Modelling of gas hydrates in sedimentary systems

Methane hydrates impact on flow through porous media

Alejandro Bello-Palacios

Thesis for the degree of Philosophiae Doctor (PhD)
University of Bergen, Norway
2022

UNIVERSITY OF BERGEN

Modelling of gas hydrates in sedimentary systems

Methane hydrates impact on flow through porous media

Alejandro Bello-Palacios

Thesis for the degree of Philosophiae Doctor (PhD)
at the University of Bergen

Date of defense: 06.04.2022

Year: 2022

Title: Modelling of gas hydrates in sedimentary systems

Name: Alejandro Bello-Palacios

Print: Skipnes Kommunikasjon / University of Bergen

Scientific environment

The research leading to this thesis was performed at the Department of Physics and Technology, University of Bergen, and at the Equinor ASA Research Centre.

This work was funded by Equinor ASA and the Research Council of Norway through the Industrial Ph.D. scheme, grant number 290534.

Acknowledgements

This research project would not have been possible without the example of outstanding scientists that I had as supervisors on the one hand and the immense support of family, friends, and colleagues on the other.

I am grateful to my supervisors, Dr. Per Fotland, and Professor Geir Ersland, for excellent guidance, patience, and encouragement during my doctoral training. I value the productive discussions and their insightful and constructive assessment of my work.

I would also like to extend my sincere thanks to my colleagues at the Research Centre in Equinor for their support and willingness to discuss my research at any time.

I am indebted to research fellows Stian Almenningen and Jung Chan Choi. Their contributions, support, and discussions were invaluable in advancing this project.

Finally, I want to extend my gratitude to my family. Luisa, Victoria, and Agustin were immense sources of love, patience, support, and hope during these years. I also want to acknowledge the support of my father and my late mother. They have always encouraged and supported any effort to improve my professional and academic development.

Preface

This dissertation presents the research carried out as a doctoral student at the Institute of Physics and Technology at the University of Bergen and as a researcher at the Equinor ASA research centre, within the industrial PhD scheme; the research was conducted between September 2018 and November 2021.

This thesis follows an article-based format in conformity with most Norwegian doctoral dissertations in natural sciences. It consists of three main parts.

The first part includes acknowledgements, a general overview of the research environment, a list of resulting publications, and their corresponding authorship statements (in which my contribution and amount of involvement as a candidate are specified), and the thesis summary.

The second part is the research synopsis: It consists of several chapters that include an introduction, methods, a synthesis of key results, conclusions, and a reflexion for further work.

The third part comprises two appendices. The first appendix includes the main scientific contributions of this doctoral thesis: three scientific articles published in peer-reviewed journals and a poster. The final appendix consists of supporting information on the methods used in this research.

Summary

In nature, gas hydrates exist in areas of permafrost and in shallow subsurface sediments at ocean depths of more than 300-500 metres. In terms of the Sustainable Development Goals (SDG) of the United Nations, better understanding of hydrates in nature can play a role in achieving energy security (SDG7), tackling climate change (SDG13) and increasing sustainability in the use of oceans (SDG14).

Hydrates represent a potential energy resource as one litre of methane hydrate contains 180 litres of methane. However, if heat stress is induced by either artificial or natural causes, its destabilisation can result in the addition of more methane to the ocean-atmosphere system. At the same time, they can trigger geohazards in their natural environments.

The knowledge of the gas hydrate dynamics when changes are imposed either naturally or artificially by drilling and gas exploitation is not sufficiently understood. To contribute to the understanding of gas hydrate dynamics in nature, we used a numerical simulator of hydrates in porous media to reproduce and study hydrate-related processes at different scales.

The TOUGH+HYDRATE (T+H) code was the main tool used in this study. It simulates the behaviour of methane hydrate in sediments and handles both multiphase and multicomponent flow and couples heat and mass flow through porous and fractured media. To streamline the use of T+H, it was necessary to build versatile pre- and post-processing tools. These tools were written in **Python** and mainly process the input and output data so that the candidate could streamline access to the data, perform analysis, and prepare visualisations. The use of these tools was essential to produce the bulk of the results and accompanying figures presented in this thesis.

The scientific output of this thesis consists of three scientific papers that present numerical modelling of hydrates in porous media in different scenarios. **Paper 1** and **paper 2** focus on modelling laboratory experiments of hydrate-bearing porous media. **Paper 1** focusses on modelling previously acquired measurements of methane relative permeability in hydrate bearing sandstone. Simulations show that the experimental values are difficult to predict by using a homogeneous distribution of hydrates throughout the sample. The experimental magnetic

resonance imaging data also showed that the hydrate distribution can be heterogeneous, meaning that the hydrates create patches. Initialising the model with a heterogeneous distribution yielded better results. These results show the impact of heterogeneity on the distribution of hydrate saturation and suggest that small amounts of hydrate can have a disproportionately large effect on the permeability. Therefore, in those cases, the use of simple models will give erroneous results because of the too high permeability.

Paper 2 studies the effect of kaolin clay on the growth of hydrates. Clay minerals are common in subsurface sediments. This study presents both experimental and modelled results. The experiments consist of the growth of methane hydrate in sand mixtures with different amounts of kaolin clay. Experimental results suggest that both clay content and initial fluid phase saturation have a large impact on the hydrate growth rate and final hydrate saturation, respectively. The experiments are simulated using particle size as a proxy for the clay content. The simulations confirm the main two effects inferred from the experiments. However, the discrepancies between the two suggest that additional mechanisms are hindering fluid flow.

Paper 3 switches to mechanisms that occur on a larger temporal and spatial scale. The dynamics of gas hydrates over longer time scales (between 100 and 600 thousand years) were simulated during different sedimentation rates and permeabilities. The results clearly show the connections between all of the detailed physical mechanisms that work during the melting and reforming of the hydrates. Hydrate melting and reformation occur in a stepwise manner, following the continuous sedimentation. The pattern of change is the result of a combination of factors, including the sedimentation rate (heating) and the intrinsic transport properties of the sediments.

The work has been fully theoretical and consisted of careful planning of simulations and the collection of experimental data from both laboratory and field. Cooperation with other research fellows and staff at the Institute for Physics and Technology at the University of Bergen has been important.

The results of this work are relevant for the understanding of natural gas hydrates in the subsurface. They are applicable to the role of hydrates as energy resources and geohazards. They may also be applicable to the ongoing research on the role of hydrates in climate. Real data from nature are hard to collect, and observations other than seismic are also difficult to obtain. There is no evidence that methane in the atmosphere originates from hydrates, but we cannot confirm its fate if the heating of permafrost and oceans continues. What we can tell is that the melting and freezing of the hydrates will probably be very slow processes. This work may provide a tool to calculate the time it will take for melting hydrates to reach the atmosphere. Then, hydrates can be entered into the climate gas budget of the planet.

Scientific contributions

List of publications

1. Bello-Palacios, A., Fotland, P., Almenningen, S., & Ersland, G. (2022). *Effects of methane hydrates on two-phase relative permeability in sandstone: Numerical simulation of laboratory experiments*. Journal of Petroleum Science and Engineering, 208, Part D (2022)

   Authorship statement: The candidate undertook the preparation, processing and analysis of the numerical simulations. The candidate was also responsible for the preparation of the manuscript and all its figures. Co-authors engaged in discussions and contributed with manuscript reviews, especially towards improving the discussion of results.

2. Bello-Palacios, A., Almenningen, S., Fotland, P., & Ersland, G. (2021). *Experimental and numerical analysis of the effects of clay content on CH_4 Hydrate formation in sand*. Energy & Fuels, 35(12), 9836–9846.

   Authorship statement: Data collection was made by fellow reasearcher Dr. Stian Almenningen. Numerical modelling, processing, analysis and comparison of results was done by the candidate. The candidate was also responsible for the preparation of the manuscript and all its figures. Co-authors engaged in discussions and contributed with manuscript reviews, especially towards improving the discussion of results.

3. Bello-Palacios, A., Fotland, P., & Ersland, G. (2022). *Modelling the effects of sedimentation on natural occurrences of CH_4 hydrates in marine sediments*. Energy & Fuels, published online in March 15, 2022.

   Authorship statement: The candidate undertook the conceptualization of the study, and undertook the preparation, processing and analysis of the numerical simulations. The candidate was also responsible for the preparation of the manuscript and all its figures. Co-authors engaged in discussions and contributed with manuscript reviews.

Other contributions

1. Bello-Palacios, A., Almenningen, S., Fotland, P., & Ersland, G. (2020). *Modelling Relative Permeability: Stretching the learnings from laboratory experiments*. Abstract and Poster presented at the **2020 Gordon Research Conference and Seminar on Natural Gas Hydrate Systems**. February, 2020. Galveston, TX United States.

Nomenclature

List of Abbreviations

CCUS Carbon capture, use and storage

EM TOUGH+HYDRATE equilibrium model

GHSZ Gas hydrate stability zone

IODP/ODP/DSDP International Ocean Discovery Program / Ocean Drilling Program / Deep Sea Drilling Project

IPCC Intergovernmental Panel on Climate Change

KM TOUGH+HYDRATE kinetic model

MRI Nuclear Magnetic Resonance Imaging

SDG Sustainable Development Goals

T+H TOUGH+HYDRATE

UNDP United Nations Development Program

UN United Nations

USGS United States Geological Survey

Symbols

ΔH specific enthalpy of hydrate reaction

λ composite thermal conductivity

μ_β viscosity of phase β

ω_κ molar concentration of component κ in hydrate

ϕ	effective porosity
ϕ_0	intrinsic porosity
ϕ_c	critical porosity when permeability is zero
ρ	density
A_S	surface area participating the the kinetic reaction
F_A	area adjustment factor
f_{eq}	fugacity at three-phase equilibrium
f_v	fugacity of gas at a given temperature
h	hours
H_κ	specific enthalpy of phase κ
J_β^κ	diffusive mass flux of component $kappa$ in phase β
k	effective permeability
K_0	intrinsic hydration reaction constant
k_0	intrinsic permeability
k_β	effective permeability of phase β
$k_{r\beta}$	relative permeability of phase β
k_{rF}	permeability reduction factor
m	T+H porosity model fitting exponent
N	Tokyo model fitting exponent
n	hydration number
P	pressure
P_c	capillary pressure
P_c^*	hydrate scaled capillary pressure
q^κ	mass source and sink of component $kappa$
q^E	heat source and sink

R	universal gas constant
r_p	average radius of sediment
S_β	saturation of phase β
T	temperature
U_κ	internal energy of phase κ
X_β^κ	mass fraction of component *kappa* in phase β
v	volumetric velocity of phase β

Contents

Chapter 1

Introduction

As part of its 2030 Agenda for Sustainable Development, the member states of the United Nations (UN) have committed to implement seventeen Sustainable Development Goals (SDGs) [UN General Assembly, 2015]. These SDGs cover a wide range of topics including food security, education, gender equality, energy supply, and sustainable consumption and production patterns. The SDGs are interdependent, and it is expected to identify both synergies and trade-offs between efforts to achieve them. The SDGs are science intensive and require the support of extensive research, innovation, capacity building, and technology transfer [Gill and Smith, 2021].

Research on gas hydrates in nature can be framed within the context of the SDGs. Advances in their understanding can contribute to efforts to achieve energy security (SDG7), tackle climate change (SDG13), and use the oceans sustainably (SDG14). Gas hydrates are a potential future energy source; they can also play a role in both the release of methane into the ocean-atmosphere system and in the safety and stability of the seafloor [Collett et al., 2015].

SDG7 aims to secure access to sustainable energy, defined as the energy produced to support development in the long term in all its social, economic and environmental dimensions [UNDP, 2000]. The current global energy system is not sustainable. First, annual energy demands have increased over the last 5 decades, from 192 EJ (4.59 Gtoe) in 1969 to 582 EJ (13.9 Gtoe) in 2019 [BP, 2021a]. Second, 84.3 % of this energy is sourced from coal, oil, and gas, and is responsible for 73.2 % of the global CO_2 emissions [BP, 2021a; WRI, 2021]. The IPCC projections show that to limit global warming to 1.5 ° C above preindustrial levels, CO_2 emissions must decrease and reach net zero around the middle of the twenty-first century [IPCC, 2018].

To respond to the IPCC projections without compromising energy security, the energy outlook made by both IEA [2021] and BP [2021b] states that future energy demands will be

more dependent on renewable energy. However, as renewable energy capacity cannot increase overnight, the demand for natural gas is expected to continue. The positive outlook for natural gas comes from its use as a less carbon-intensive replacement for coal in the power sector and as a source for producing (blue) hydrogen. Gas also has the potential to become a near-zero carbon source if these uses are combined with technology for carbon capture, use, and storage (CCUS) [BP, 2021b].

The exploitation of naturally occurring methane hydrates as an energy resource can play an important role in the actions to secure a reliable gas supply in the future. $1\,m^3$ of gas hydrate can contain up to $180\,m^3$ of methane at surface conditions [Ruppel and Kessler, 2017]. Although gas hydrates occurrences have been identified extensively all over the world, there are large uncertainties in estimating the total amount of methane from these. However, conservative estimates suggest that they can provide one to two orders of magnitude more methane than global natural gas reserves [Beaudoin et al., 2014].

Actions to achieve SDG7 commitments cannot be detriment to those to achieve SDG14 and SDG13. The targets to achieve SDG14 can be hampered by pollution related to the drilling and production of hydrocarbons. Furthermore, these activities cause thermal and mechanical stresses that may trigger the dissociation of hydrates [Collett et al., 2015]. Uncontrolled release of methane into the ocean-atmosphere system and loss of strength of the host sediment can trigger marine geohazards, increase the amount of gas emissions, have adverse effects on surrounding ecosystems and compromise the integrity of both the drilling and production infrastructures [Wang et al., 2018].

A better understanding of hydrate systems in nature can be crucial in the actions made to achieve SDG13. Despite the threat of climate change that causes the destabilisation of gas hydrates, there is still limited understanding of the mechanisms and the amount of methane actively released into the ocean-atmosphere system [Ruppel and Kessler, 2017].

The work presented in this thesis aims to expand on the understanding of methane (CH_4) hydrates in earth systems. Numerical simulation is used as the main method to reproduce hydrate-related processes in different scenarios. Such scenarios include both laboratory experiments and large-scale natural processes. The focus of each modelled scenario was primarily to investigate the effects of different parameters on both the formation and dissociation of hydrates in porous media. Simultaneously, they include an analysis on how the presence of hydrates in porous media can alter fluid flow. Finally, these scenarios are an application that puts the capabilities of the numerical simulator to the test. The results of this work are relevant for understanding the complexity of fluid flow through porous media in systems where the formation and dissociation of hydrates is occurring. They also highlight the advantages and limitations of using numerical simulation tools. These findings may be valuable in as-

sessing methane as a potential energy source and its role in the context of climate change and geohazards. The following sections include a brief introduction to hydrates, their occurrence in nature, and how numerical models can be used to represent them.

Chapter 2

Theory

2.1 Fundamentals concepts on gas hydrates

Gas hydrates are nonstoichiometric ice-like solid compounds that form under certain conditions of pressure (P) and temperature (T) within a gas/water mixture. They are clathrate compounds in which water molecules (host) connect by strong hydrogen bonds, forming a polyhedral crystalline lattice. Cavities through the lattice allow the allocation of (guest) gas molecules that stabilise the structure by van der Waals forces between the guest and host molecules. [Hassanpouryouzband et al., 2020; Sloan and Koh, 2008; Ye, 2013].

The shape and size of the guest molecules influence the structure of the clathrate hydrate [Sloan, 2003]. These structures can normally be grouped into cubic structures SI and SII, or the hexagonal structure SH. Figure 2.1 shows the different cavities that make up each structure. Common guest molecules are light hydrocarbons (i.e. methane, ethane) and inorganic gases such as carbon dioxide, nitrogen, or hydrogen sulphide. A cavity filled by a molecule does not result in a chemical bond between host and guest molecules. In addition, not all cavities in the clathrate lattice need to be filled. This gives the hydrates their non-stoichiometric nature, and their composition is normally described in terms of the average ratio between the number of water molecules and the number of guest molecules forming the unit crystal of a clathrate structure. This ratio is also called the hydration number (n). Methane hydrate has a type I structure and a hydration number of 5.75, which means that to form a unit crystal with maximum occupancy, 44 molecules of water are needed to enclose 8 methane molecules in a clathrate lattice (equation 2.1).

$$CH_4 + 5.75\,H_2O \rightleftharpoons CH_4 \cdot 5.75\,H_2O\,(s) \tag{2.1}$$

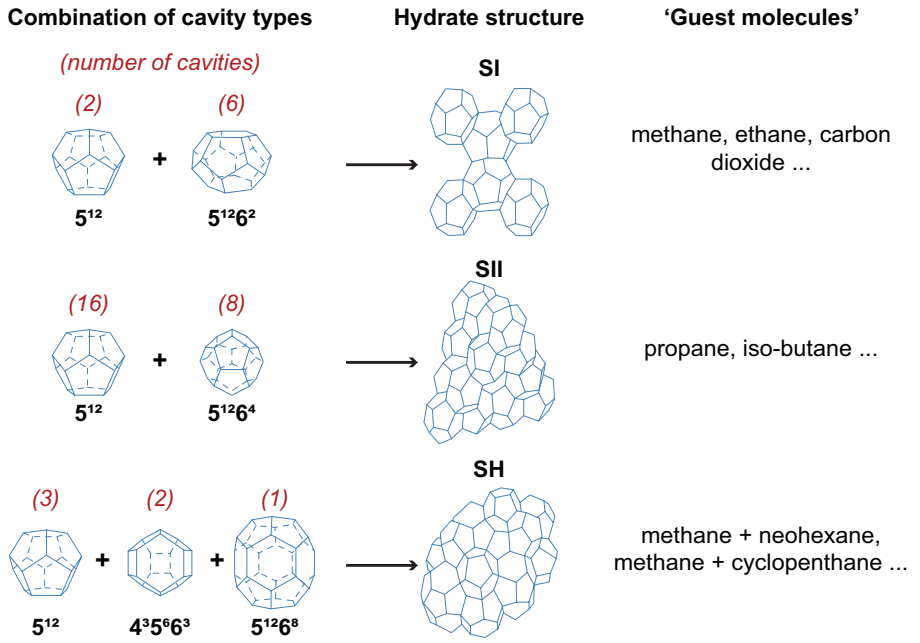

Figure 2.1: Geometric representation of cavities and structures SI, SII and SHH of gas hydrates. $5^{12}6^4$ indicates a water cage composed of 12 pentagonal and four hexagonal faces. The red text in brackets indicates the combination and number of iteration of each cage types that constitute each structure. For example, the structure I unit crystal is composed of two 5^{12} cages, six $5^{12}6^2$ cages and 46 water molecules. Modified from Sloan [2003]

In addition to its molecular structure, the thermal, mechanical, and electromagnetic properties of the hydrate are affected by the nature of the guest molecules. Hydrate-forming components also define the P-T conditions in which they can coexist in different phases in the equilibrium state [Hassanpouryouzband et al., 2020]. Hydrate formation is favoured not only by the availability of guest and host molecules, but also by having the entire system at a sufficiently low temperature or high pressure (Figure 2.2). The stability of hydrates is also affected by the inclusion of soluble components in water, such as salts or alcohols.

The process of hydrate formation is a time-dependent process, steered by the mass transfer of components and the reaction at the growing crystal surface [Sloan and Koh, 2008]. The kinetics of hydrate formation is normally described by a period of hydrate nucleation followed by a period of growth. Hydrate nucleation is a microscopic and stochastic event in which both water and guest molecules form and disperse in clusters until it achieves a critical size for continued growth [Hassanpouryouzband et al., 2020; Sloan and Koh, 2008]. At a macroscopic level, the period of time at which nucleation occurs is referred to as the induction time. At this point, the crystals will continue to grow as long as there is a constant supply of hydrate-forming components.

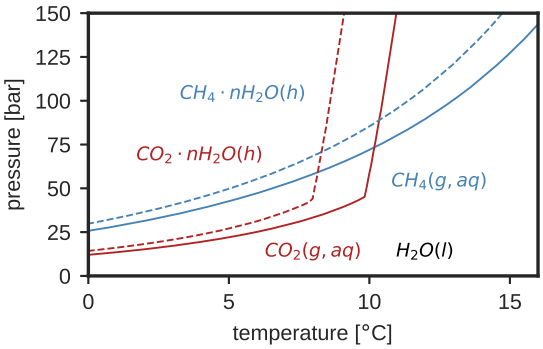

Figure 2.2: Phase boundary stability plot of CH_4 and CO_2 hydrate in fresh water (continuous line) and 3.5 wt.%NaCl brine (stipled line). Only hydrates (h) and excess fluids are found on the upper/left side of the stability curve. Only gases (g), liquids(l) and dissolved components (aq) are found on the lower/right side of the stability curve. The stability curves are calculated using the PVTsim software [Calsep, 2020].

Interest in hydrates from both industrial and academic perspectives has grown since their discovery. Ye [2013] describes this evolution in three main stages. The first stage kicks off with their discovery in 1810 by Davy and extends until the 1930s, where research focused mainly on laboratory work. These advances were crucial for the synthesis of different types of hydrates. During the second stage, between the 1930s and 1950s, hydrates were encountered as an industrial hazard that would cause blockages in gas transport pipelines. Research focused on characterisation of hydrates to allow forecast and prevention of these hazards. Since the 1960s, there has been a comprehensive growth in research on the natural occurrences of hydrates, supported by both industry and academia. Its main focus has been to understand, predict, and characterise the settings in which hydrates can naturally occur. Today, there is a better understanding of the impact of hydrates on the safety and stability of the seafloor, and research activities continue to provide data to study the relationship of hydrates with climate change, geohazards, and the feasibility of gas hydrates as a future energy resource Collett et al. [2015].

2.2 Gas hydrates in nature

Gas hydrates have been found in a wide range of natural environments (Figures 2.3 and 2.4). Relatively cold environments and deep marine regions, coupled with the abundance of hydrocarbon gas, provide conditions that allow the development of natural hydrate occurrences within the pores of sediments and rocks. The predominant guest molecule is methane. Since

1 m^3 of hydrate can contain approximately 170 m^3 of methane gas at standard temperature and pressure, gas hydrates are not only an important energy source, but are relevant to understand the role of methane emissions in climate change and assess geological hazards [Sloan and Koh, 2008].

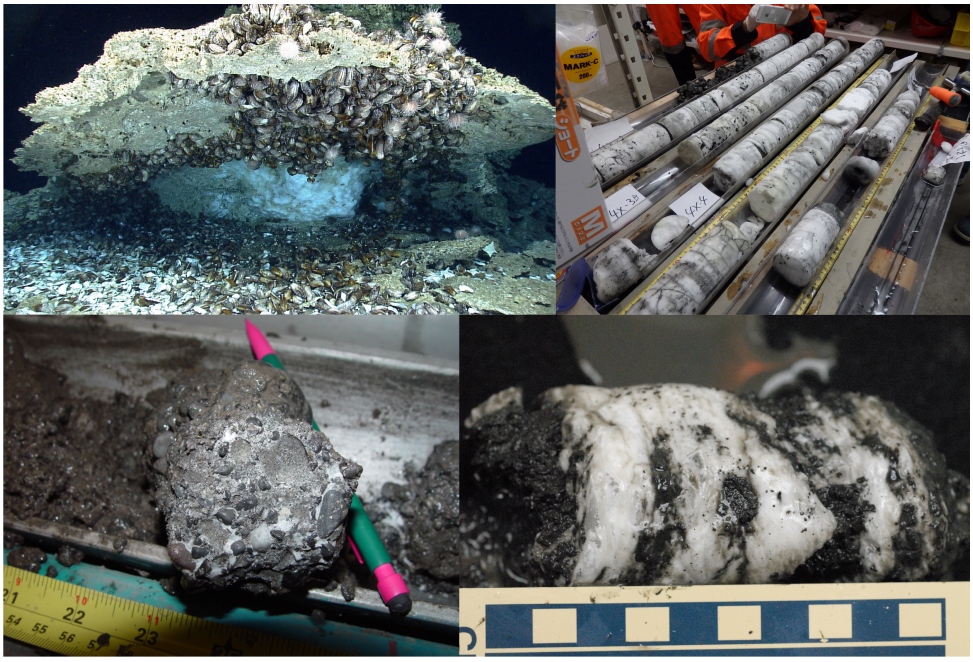

Figure 2.3: Examples of hydrate occurrences in nature. Top left: as hydrate formation under carbonate rock in Gulf of Mexico [USGS, 2017a]. Top right: Massive hydrates recovered from Nankai Trough (Japan) [Matsumoto et al., 2017]. Bottom left: Hydrate-bearing sandstone from Mallik (Canada) [USGS, 2017b]. Bottom right: Hydrate in marine sediments from Indian Ocean [USGS, 2006]

Natural hydrate occurrences have been inferred all over the globe in both onshore and offshore settings, predominantly linked to sediments in permafrost areas, subglacial settings, and upper continental slopes and deep marine settings [Ruppel and Kessler, 2017]. There is still uncertainty in knowing the estimate of the total amount of methane currently stored in natural hydrates, but observations indicate that more than 95% of them are spread in deep marine sediments [Ruppel, 2015]. In marine sediments, from top to bottom, the probability of the occurrence of hydrates extends between the sea floor and a limit of stability delimited by the gas composition, pressure, temperature, and salinity of the pore water at each location of the geosphere. This interval is commonly referred as the gas hydrate stability zone (GHSZ) (Figure 2.4 top). In terms of sediments or rock characteristics, most natural hydrates occur in deep marine fine-grained sediments. From a resource perspective, only a small fraction of these hydrates are hosted by porous sediments or rocks suitable for production [Boswell and Collett,

2011].

Data acquisition from exploration and drilling activities has been an important contribution to the current understanding of hydrates in nature. Hydrate accumulations in permafrost settings have been drilled in Canada (Mallik site), Alaska (Northern Slope) and China (Qinghai-Tibetan plateau). Marine hydrates have also been the target of scientific and commercial drilling programmes. The scientific results of IODP / ODP / DSP of leg 164 at Blake Ridge [Paull et al., 2000], leg 204 at Hydrate Ridge in offshore Oregon [Tréhu et al., 2006], and expedition 311 at the Northern Cascadia margin [Riedel et al., 2010] have provided crucial data for studying and monitoring hydrate systems in these types of settings. In addition, the governments of the United States, Japan, South Korea, India, and China have initiated national-led programmes to evaluate the economic prospectivity of hydrate occurrences in the Gulf of Mexico, Nankai Trough, Ulleung basin, the Krishna-Godavari basin, and South China Sea, respectively [Collett et al., 2015].

From the perspective of hydrates as an energy source, there is still limited data to provide an accurate assessment of its potential [Collett, 2019]. To this day, only a handful of short-term production tests have been conducted. Although these results demonstrate the potential of gas production from hydrate reservoirs, there are still challenges to assess recoverable volumes, current production technology, and there is no guarantee of the economic viability of these resources [Collett et al., 2015; Collett, 2019].

From the perspective of climate change, concerns about the role of hydrates in contributing to global methane emissions have grown alongside new knowledge. The main basis of these concerns is the susceptibility of hydrates to changes in pressure temperature. The effects of climate change, such as changes in sea level (pressure) and increases in global temperatures, can trigger the dissociation of natural hydrate occurrences. Furthermore, drilling and gas production in hydrate reservoirs can result in inadvertent gas leakage. However, there is no conclusive proof of the actual contributions of methane emissions from hydrates and simplifications in the models used may have resulted in an overestimation of these [Ruppel and Kessler, 2017]. Similarly, the incipient state of hydrate production tests does not allow one to make a sound assessment of potential gas leakages.

Both the energy and climate perspectives have also touched on the potential effects of hydrate dissociation in host sediments. The dissociation of hydrate replaces a solid component with free gas and excess pore water, changing the geomechanical stability of the sediment or rock. This process has the potential to trigger inadvertent costs and risks and can be framed as geohazards [Collett et al., 2015]. Boswell et al. [2012] groups them into two main categories: naturally occurring geohazards and operational geohazards (Figure 2.4). Naturally occurring geohazards refer mainly to geological processes that can occur in response to thermal and

mechanical stress induced by changes in sea level and global temperature rises (Figure 2.4a). Operational geohazards refer to the unintended consequences of human activities that affect hydrate occurrence (Figure 2.4b). Activities such as drilling through hydrates or extracting fluids from the subsurface bring thermal and mechanical stresses that can destabilise hydrates.

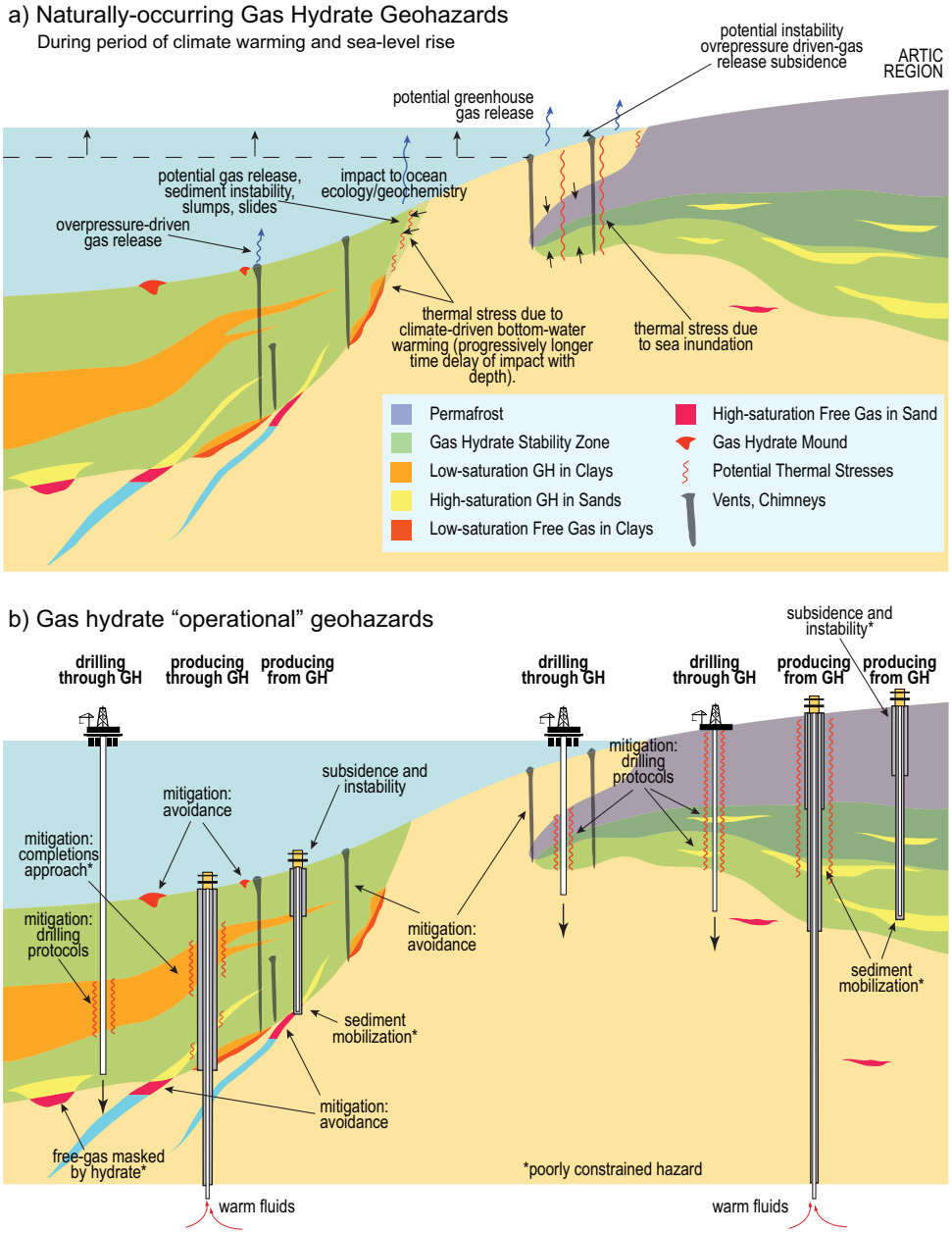

Figure 2.4: Overview of natural occurrences of gas hydrates and their related natural and man-made geohazards. Modified from Boswell et al. [2012]

Although these three perspectives justify the relevance of studying hydrates in nature, they also bring attention to the knowledge gaps and the challenges of assessing their impact on any of

these three fronts. Despite extensive laboratory-scale experiments to support the findings from exploratory drilling and incipient production tests, there are still challenges to understanding hydrate-related processes at multiple scales and over longer periods of time. Current understanding of how hydrates interact with geological, biological, and chemical processes in the earth system is still at an early stage [Yin and Linga, 2019].

2.3 Numerical modelling of gas hydrates in porous media

Numerical simulation of hydrates in porous media has become an important tool to support research on hydrate systems. It is an essential tool for evaluating the resource potential of methane hydrates, gas production rates, and the geomechanical and environmental impact of methane production from hydrate systems [Collett et al., 2015]. These learnings can also be applied to model the formation and evolution of hydrates in natural systems on geological time scales [You et al., 2019].

Several codes have been developed and tested in the last decades. In essence, they couple heat, mass, and fluid transport equations together with models for the formation and dissociation of hydrates. With the growing interest in hydrates as a potential energy resource and the development of national energy-driven initiatives, a major part of the tools are reservoir simulation codes developed to simulate methane production from hydrates. Given the lack of real data to calibrate the simulators, several codes have been subjected to code comparison efforts to validate their suitability for assessing the methane producibility of hydrates [White et al., 2020] and incorporating geomechanical processes [Wilder et al., 2008].

In addition to production, there has been a focus on modelling the formation and evolution of hydrates in nature. This type of modelling has been considered essential to understand the distribution and concentration of hydrates in nature [You et al., 2019]. Although not fit for purpose, some conventional reservoir simulators have been used to model the evolution of hydrates over geological time [HE et al., 2011; Liu et al., 2019; Zhu et al., 2020]. More recently, with the goal of incorporating geological processes such as sediment burial and compaction and organic matter methane generation, some authors have repurposed conventional basin modelling tools [Burwicz et al., 2017; Piñero et al., 2016] or developed codes that couple these mechanisms with hydrate-related processes [You and Flemings, 2021].

TOUGH+HYDRATE (T+H) was used in all of the research results presented here. The following methods chapter provides more detailed information about T+H.

Chapter 3

Methods: TOUGH+HYDRATE

The TOUGH+HYDRATE v1.5 (T+H)[Moridis, 2014] code and its open-source version HydrateResSim [Gamwo and Liu, 2010] are codes developed by Lawrence Berkeley National Laboratory. Both codes have been used in the numerical evaluation of natural occurrences of gas hydrates [Jin et al., 2018; Li et al., 2015; Moridis et al., 2004; Sun et al., 2016] and to model experiments on hydrate formation [Li et al., 2014; Yin et al., 2018]. These codes simulate the behaviour of methane hydrate-bearing sediments and handle multiphase, multicomponent flow and transport of mass and heat through porous and fractured media [Moridis and Pruess, 2014].

T+H became the main tool used to carry out the studies included in this thesis. This chapter presents a brief summary of the governing equations. It gives special focus to the way T+H handles transport properties. Finally, it includes information on a series of pre- and post-processing tools that were built as part of this thesis to optimise the utilisation of T+H.

3.1 Governing equations

In terms of hydrate mass components (κ), T+H includes a host (water, H_2O), a guest (methane, CH_4) and a water-soluble inhibitor (i.e. sodium chloride NaCl). These components can be partitioned into four possible phases (β): hydrate (H), aqueous (W), gaseous (G) and solid ice (I).

Formation and dissociation can be modelled using either an equilibrium model (EM) or a kinetic model (KM). In EM, the mass and energy balances are governed by equations 3.1 and 3.2, respectively, bringing a total of three equations. If a soluble inhibitor is considered, the number of equations increases to four.

$$\frac{\partial}{\partial t}\left[\sum_{\beta=A,G,H,I}\phi S_\beta \rho_\beta X_\beta^\kappa\right]+\nabla\cdot\left[\sum_{\beta=A,G}\rho_\beta \vec{v}_\beta X_\beta^\kappa+\sum_{\beta=A,G}\vec{J}_\beta^\kappa\right]=q^\kappa \qquad \kappa=w,m,i \tag{3.1}$$

$$\frac{\partial}{\partial t}\left[\sum_{\beta=A,G,H,I}\phi S_\beta \rho_\beta U_\beta+(1-\phi)\rho_R U_R+\phi S_H \rho_H \Delta H\right]+\nabla\cdot\left[\sum_{\beta=A,G}\rho_\beta \vec{v}_\beta H_\beta-\lambda\nabla T\right]=q^E \tag{3.2}$$

In the expressions 3.1 and 3.2, ϕ represents intrinsic porosity, S is phase saturation, ρ is density, X_β^κ is the mass fraction of each component κ in phase β, v is the volumetric velocity of each fluid phase, J_β^κ is the diffusive mass flux of the component κ in phase β, q represents either mass transfer (*kappa*) or heat E transfer associated to sinks and sources. U is the internal energy of each phase β or the rock matrix R. H is the specific enthalpy of each phase. ΔH is the specific enthalpy of the hydrate reaction. λ is the composite thermal conductivity and T is the temperature.

The convective and diffusive transfer of mass and heat is incorporated into the expressions 3.1 and 3.2. On the left-hand side, the 1st term is the mass accumulation term and the 2nd term is the flux term. The right-hand side of the equations represents both the source and the sink. The inclusion of the specific enthalpy (ΔH) on the first term of expression 3.2 notes the hydrate reaction in the accumulation term. Expressions 3.1 and 3.2 show that the phase transitions in EM depend on pressure and temperature (Figure 3.1) and are driven by both heat and mass flow [Teng and Zhang, 2020].

In KM, the mass balance is governed by equations 3.3 and 3.4. The energy balance is governed by equation 3.5. In KM, hydrates are treated as a new mass component κ. The expression 3.4 incorporates an Arrhenius-type expression based on the work of Kim et al. [1987] that calculates phase transitions as a kinetic reaction. This new equation brings a total of four equations, or five if a soluble inhibitor is considered.

$$\frac{\partial}{\partial t}\left[\sum_{\beta=A,G,I}\phi S_\beta \rho_\beta X_\beta^\kappa\right]+\nabla\cdot\left[\sum_{\beta=A,G}\rho_\beta \vec{v}_\beta X_\beta^\kappa+\sum_{\beta=A,G}\vec{J}_\beta^\kappa\right]=q^\kappa+\omega_\kappa q^H \quad \kappa=w,m,i \tag{3.3}$$

$$\frac{\partial}{\partial t}(\phi S_H \rho_H)=q^H=-K_0 e^{(-\Delta E_a/RT)}F_A\, A_S\, (f_{eq}-f_v)M_H \tag{3.4}$$

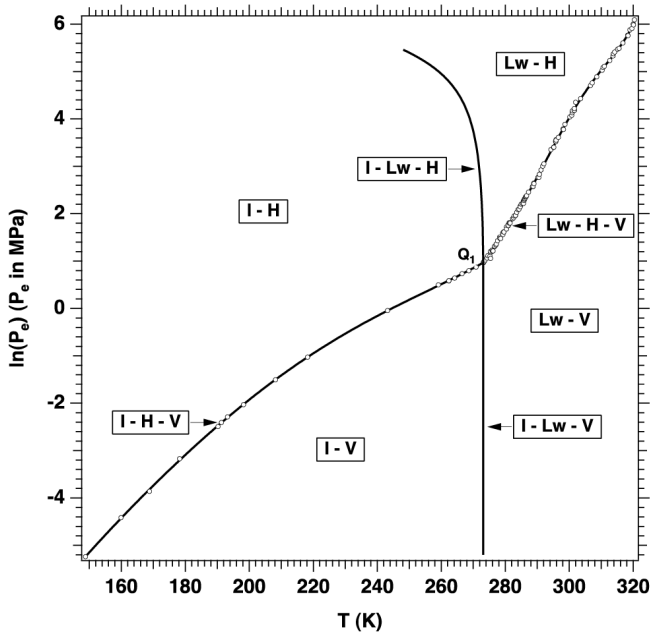

Figure 3.1: Pressure-temperature equilibrium relationship in the phase diagram of the water–methane–hydrate system. All possible combinations of the four phases are displayed: aqueous (Lw), ice (I), gas (V), and hydrate (H).[Moridis and Pruess, 2014]

$$\frac{\partial}{\partial t}\left[\sum_{\beta=A,G,H,I}\phi S_\beta \rho_\beta U_\beta + (1\phi)\,\rho_R U_R\right] + \nabla\cdot\left[\sum_{\beta=A,G}\rho_\beta \vec{v}_\beta H_\beta - \lambda\nabla T\right] = q^E + q^H \Delta H \quad (3.5)$$

In addition to the variables included in expressions 3.1 and 3.2; in expressions 3.3, 3.4 and 3.5, ω_κ is the molar concentration of the component κ in hydrate, K_0 is the intrinsic hydration reaction constant, ΔE_a is the hydration activation energy, R the universal gas constant, F_A an area adjustment factor, A_S is the surface area participating in the kinetic reaction, f_{eq} is the fugacity at three-phase equilibrium and f_v is the fugacity of gas at a given temperature.

Kowalsky and Moridis [2007] and Teng and Zhang [2020] have compared both modelling strategies. Kowalsky and Moridis [2007] concluded that they were practically indistinguishable for long-lasting and large-scale processes, but that KM would be more suitable for short-lasting and core-scale simulations. Teng and Zhang [2020] conclude that EM is a special case of KM in which the relative strength of the hydrate reaction is greater than those of other physical processes. The authors also indicate that KM may be more computationally efficient.

3.2 Transport properties

The effect of hydrates on transport properties was an important part of the studies included in this thesis. T+H handles them using different models. The model chosen for these studies is described as *evolving porous medium model* [Moridis and Pruess, 2014]. In this model, the hydrate and ice phases are solid phases that become an extension of the matrix. This results in the creation of a new porous medium that continuously changes its porosity and intrinsic permeability. The remaining pore space is filled only by the fluid phases [Moridis and Pruess, 2014]. Effective porosity (ϕ) is equivalent to the pore volume filled only by the fluid phases. It is a function of both intrinsic porosity (ϕ_0) and hydrate saturation (S_H) (Eq. 3.6). [Moridis and Pruess, 2014].

$$\phi = \phi_0 (1 - S_H) \tag{3.6}$$

T+H provides the option of using this treatment of porosity to scale both permeability (k) and capillary pressure (P_c) as functions of hydrate saturation (S_H). The scaling of permeability (Eq 3.7) is based on the model defined by Verma and Pruess [1988]. It is a power-law relationship between the ratio of porosity and the ratio of permeability. The critical porosity parameter ϕ_c accounts for scenarios of hydrate clogging pore throats and disconnecting fluid-filled pores. The ratio between effective and intrinsic permeability is referred as the permeability reduction factor k_{rF}.

$$\frac{k}{k_0} = K_{rF} = \left(\frac{\phi - \phi_c}{\phi_0 - \phi_c} \right)^m \tag{3.7}$$

$$\frac{k}{k_0} = (1 - S_h)^N \tag{3.8}$$

This approach is similar to the Tokyo model (eq. 3.8) proposed by Masuda [1997]. In both models, the exponents m and N steer the rate at which the permeability is reduced. No particular restrictions are given on the magnitude of the parameters n and N. These fitting parameters accept a wide range of values aimed to make the models fit different scenarios. Dai and Seol [2014] linked the magnitude of this parameter with pore habits and found that it can vary from N=1.25 for sediments with uniform cementing hydrate, to N=25 for sediments with uniform pore-filling hydrate.

In T+H, Moridis and Pruess [2014] assumes that changes in porosity and permeability are related to changes in capillary pressure. The formation of solid phases will alter the pore

distribution and may have an impact on the effective radius of the pore throats. The Leverett [1941] model (Eq. 3.9) is implemented to scale the capillary pressure.

$$P_c^* = P_c \sqrt{\frac{k_0}{k} \cdot \frac{\phi}{\phi_0}} \tag{3.9}$$

For further details on other physical processes represented by T+H, the reader is referred to the user manuals [Moridis, 2014; Moridis and Pruess, 2014].

3.3 Pre- and post-processing

T+H does not provide a user interface to either prepare the simulations or analyse their output. Data handling is accomplished by means of fixed-format text-based files. The input data and specifications for the type of simulation are organised in a single file under different data blocks, defined by keywords. The preparation of each simulation involves editing and modifying the input file using a text editor. The output data consists of a series of text files with different formats. Processing the output data involves parsing these files and using a data analysis application to store, analyse, and visualise the output.

This manual process can be error-prone, time-consuming and ultimately a hindrance for efficient analysis and visualisation of the modelled results. Therefore, it was essential for the objectives of this thesis to build tools for the pre- and post-processing of the simulation files. These tools offer a more strict control in the preparation of each simulation and different workflows to process the output data.

The tools were written in ***python***. These scripts hold a simple structure of nested functions that can be used in or adapted to be used in any T+H simulation file. Aside from standard Python packages, it uses mainly the ***pandas*** and ***numpy*** libraries. These tools reside on the *TH-PrePost* GitHub repository [Bello-Palacios, 2021] and can be accessed by anyone. For further details on how to get a hold of these scripts, the reader is referred to Appendix B. The scripts are open to be modified and upgraded. In their simplest form, their contents can be described in four main categories.

1. **Pre-processing scripts:** Stored in the `TH_proc.py` file. Scripts for reading and editing T+H input files. The scripts turn the T+H input file into a dataframe stored in memory that can be edited and written into a new file.

2. **Post-processing scripts:** Stored in the `TH_post.py` file. Scripts for reading and editing

T+H output files. The scripts turn the T+H output files into a dataframe that can be used for plotting and further analysis.

3. **Bokeh graphical interface:** Built in `Simple_Tutorial.ipynb` Jupyter notebook and uses the function stored in the `TH_post_Bokeh.py` file. Simple graphical interface to visualize the processed output. These scripts have been designed to produce simple visualizations of one- and two-dimensional grids.

4. **Auxiliar functions:** Scripts included in the `Aux_Functions.py` and `MeshMaker.py` files. A diverse group of functions used for different purposes like setting the input files for the MeshMaker facility, and running both T+H and the MeshMaker facility from python, amongst others.

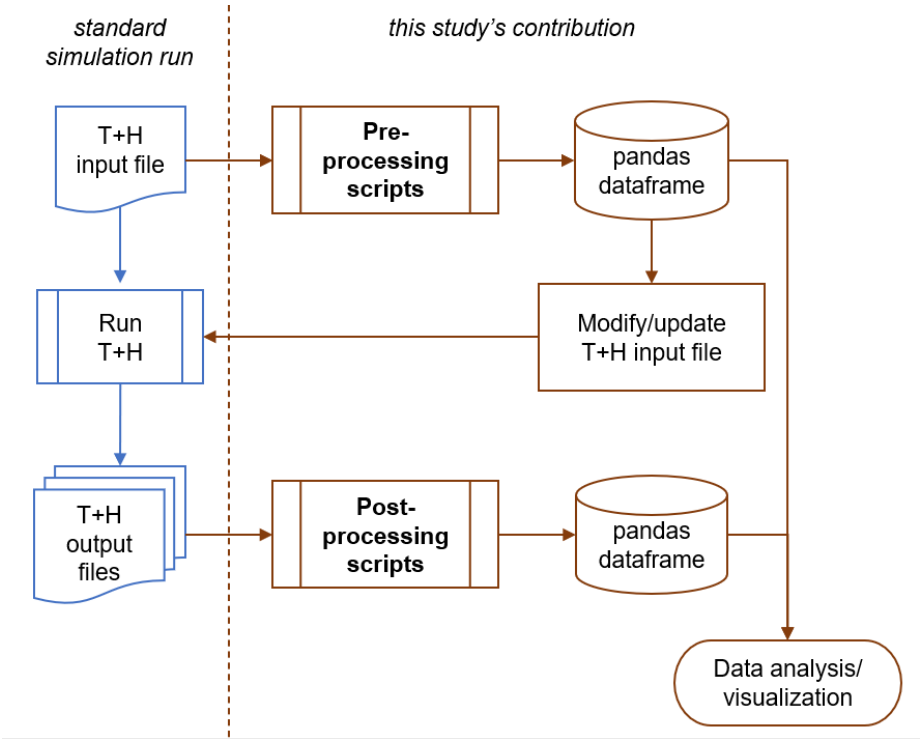

Figure 3.2: Flowchart displaying how the use of the scripts assists running T+H.

The bulk of the analysis and figures presented in the enclosed results were only made possible by using these routines. These scripts transformed the input and output data into different indexable tables (i.e. arrays, pandas dataframes). This allowed an easier access to the data, the execution of numerical analysis, and the preparation of data visualisations (i.e., plotting). A typical simulation workflow in T+H involves the preparation of the input files, running T+H,

and processing the output results. The scripts complemented this workflow by streamlining each of the steps (Figure 3.2).

Chapter 4

Results and discussion

This chapter summarises the main findings of this research. The results include applications of the use of TOUGH + HYDRATE (T + H) to model hydrates in porous media on different scenarios and scales (Figure 4.1). The simulation setup for each scenario is intertwined with the nature and scale of the processes modelled. The reader is referred to the papers enclosed for specific details about the approach used in building the simulation grid, boundary conditions, data used, and experimental setup.

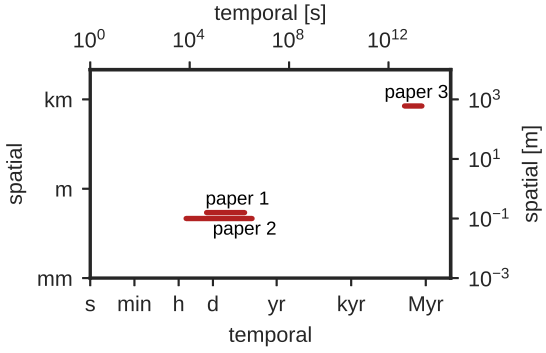

Figure 4.1: Spatial and temporal scale covered by the experiments and simulations studied on each manuscript. **Paper 1** and **paper 2** focuses on laboratory-scale experiments lasting for hours and days. **Paper 3** focuses on basin-scale experiments lasting for hundreds of thousands of years.

4.1 Modelling hydrates at laboratory scale

The scope of this section is to present the results of modelling hydrates in porous media on a laboratory scale. The temporal and spatial scales of these studies include experiments and simulations that last hours to a few days in hand-sized core specimens (Figure 4.1).

Laboratory experiments are reproduced numerically. The main contribution of these studies is the comparison between experimental and modelled results and the use of the simulator as a verification tool. The main topics of **Paper 1** and **Paper 2** are relative permeability measurements and the effects of clay on hydrate growth, respectively.

4.1.1 Hydrate effects on relative permeability

Paper 1 focusses on modelling measurements of methane relative permeability in hydrate-bearing sandstone. A series of laboratory experiments published in Almenningen et al. [2019] were simulated using the T + H kinetic model (KM) in one and two dimensions. The experiments consisted of core flooding experiments in cylindrical hydrate-bearing sandstone cores. Each experiment provided measurements of gas relative permeability (K_{rG}) and phase saturation (S_W, S_G, S_H), before and after hydrate formation (Figure 4.2).

In addition to testing the ability of T + H to represent core flooding experiments, 1-D and 2-D simulations were used as tools to support the analysis and interpretation of the experimental results. The use of 1-D models gave preliminary insight on how efficient the hydrate formation process was during the experiments. These simulations model the final distribution of fluid and solid phases in an ideal system where gas and brine are always in contact. Hydrate growth in these models is constrained only by its thermodynamics. As expected, these simulations yielded more hydrates than the experiments (Figure 4.3). These discrepancies were interpreted as internal restraints that hinder the possibility of contact between the hydrate-forming fluids. An indication of this came from the fact that there were smaller discrepancies between the cases initialised with more methane (exp. A), compared to the case initialised with the least amount of methane (exp. H). When the system is initialised with a low S_G, the effective permeability of the gas (k_G) is also reduced. This is intensified by a further reduction in S_G as more hydrate forms. Reduced K_G can cause the injected gas to not reach certain parts of the system. This can be exacerbated by the internal restraints of hydrate interrupting the contact between hydrate forming fluids. This results in limited growth of the hydrate and separated volumes of brine and gas.

KM does not account for nucleation phenomena, and hydrate formation results in an instantaneous and homogeneous phase Kowalsky and Moridis [2007]. However, the formation of

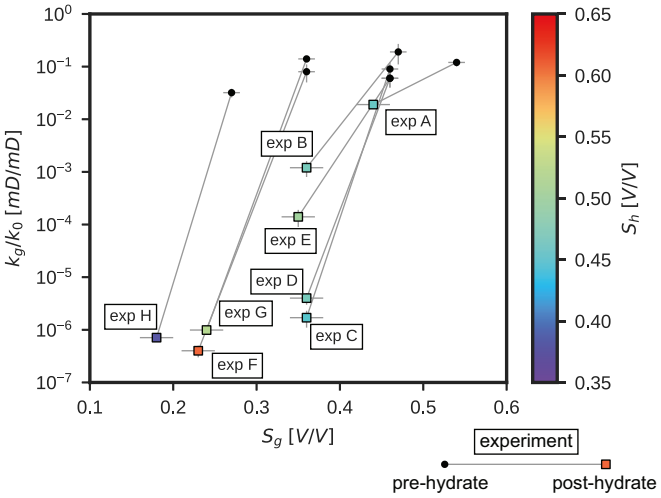

Figure 4.2: Overview of all the methane relative permeability measurements and margin of errors. Black circles show gas relative permeability before hydrate formation. Colored squares show relative permeability after hydrate formation. Color shade in squares represents hydrate saturation. Stippled lines connect measurements in each experiment.

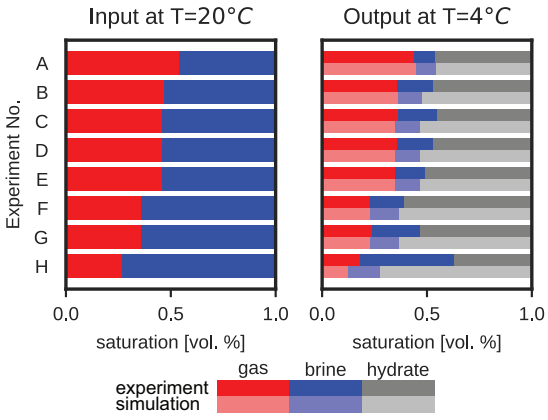

Figure 4.3: Overview of phase saturations measured before and after cooling down. In a lighter shade of color, modelled saturations from single cell simulations are added for comparison.

hydrates in porous media can result in a patchy distribution of crystals. To account for heterogeneity in the distribution of hydrates and their effect on effective permeability, the 2D grid was populated with a stochastic distribution of hydrate saturation (S_H) values. In addition to the homogeneously saturated grid, a spectrum of stochastic arrangements was tested, ranging from a narrow distribution (near-homogeneous) to a broad distribution for each experiment. All iterations had the same bulk average saturation. For the distribution of the remaining fluid phases, each grid was populated with and without the effect of hydrate on the intrinsic capillary pressure function (Eq. 3.9). Using Darcy's law, the estimation of permeability from simulated core flooding experiments was defined as follows:

$$k_G = \mu_G \cdot \frac{\Delta x Q_G}{\Delta P}$$

k_G is the effective gas permeability, μ_G is the gas viscosity, Δx is the length of the 2D grid, and ΔP is the pressure drop registered between each side of the grid in each simulation.

When P_c was not scaled to hydrate saturation, core flooding simulations did not return significant drops in pressure (ΔP). However, when the hydrate scaled P_c^* was included and the heterogeneity in S_H increased, the pressure drops were much higher, resulting in drastically lower relative permeability (Figures 4.4). Figures 4.5 the gradual decrease in effective flow, observed in simulations for Exp. B.

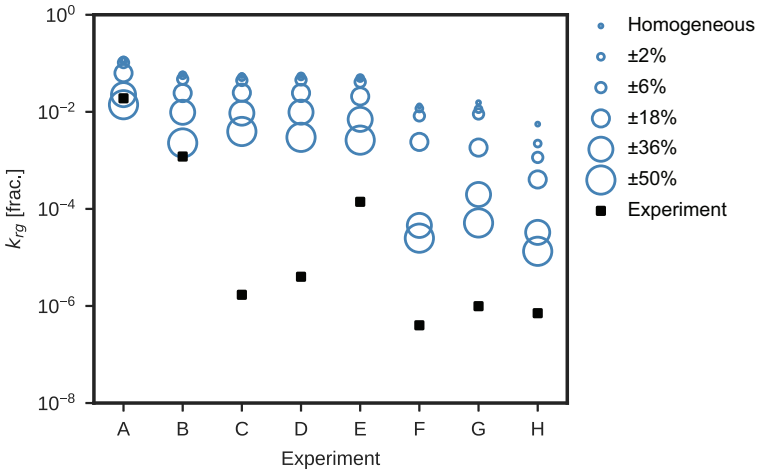

Figure 4.4: Comparison between measurements of methane relative permeability (black squares) and simulated estimations (blue circles). The radius of the circles represents the standard deviation of the phase saturations within the grid. Smallest circles correspond to homogeneous distribution and the largest circle to a distribution with a broad variation ($\sigma = \pm 50\%$).

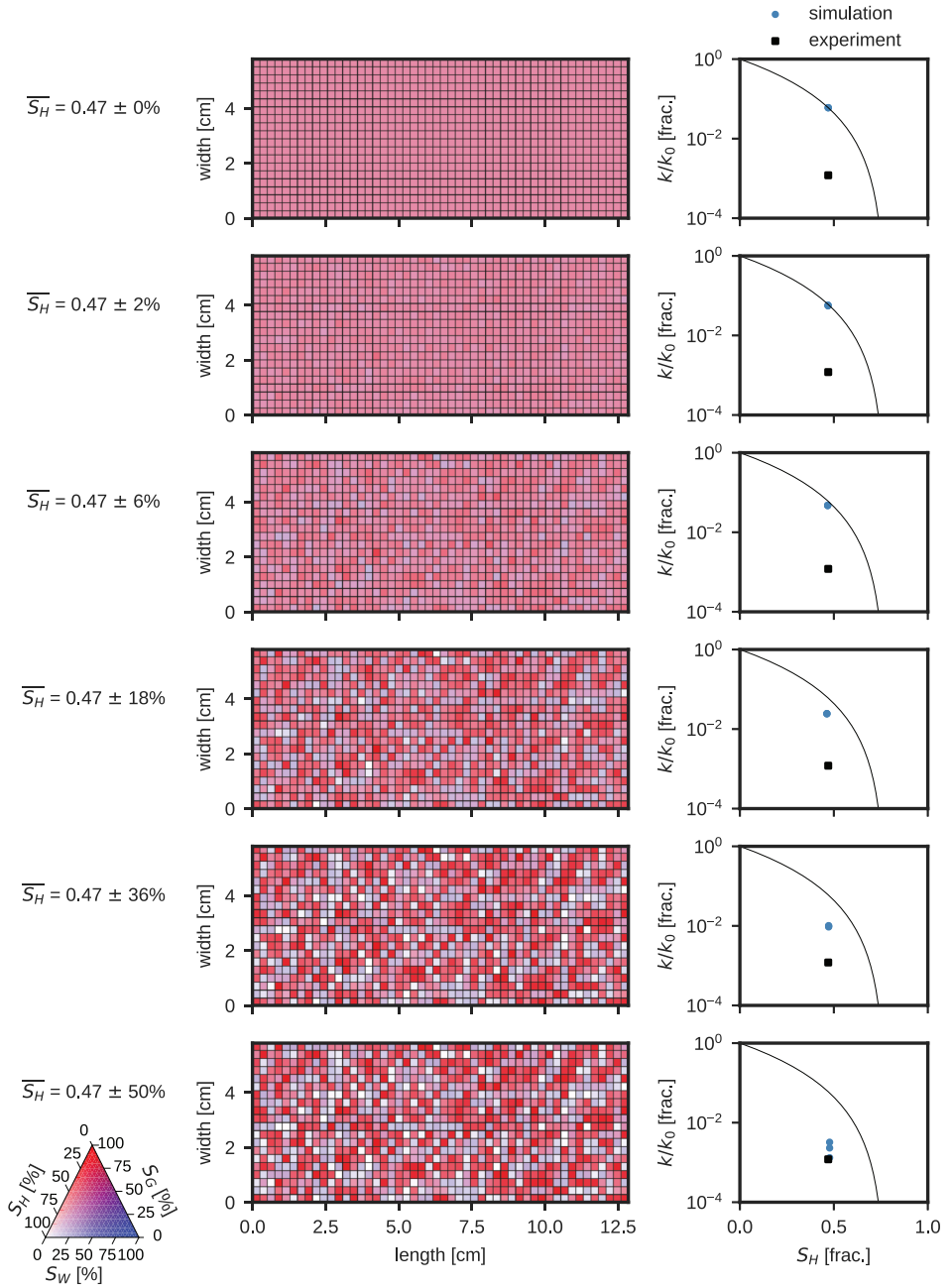

Figure 4.5: **Paper 1** - Experiment B. Effect of heterogenous distribution on gas relative permeability k_{rG}. The first two columns on the left show the distribution of phases. The third column shows the resulting k_{rG} plotted against the average S_H (blue circle). As reference, the measure k_{rG} is included (black square), and the theoretical model of permeability reduction used by T+H (black curve).

The simulator was a useful tool for testing scenarios that could explain the reasons for the large reduction in k_{rG} observed in the experiments (Figure 4.2). Although the development of a patchy distribution of hydrates is expected in these types of experiments, the use of a numerical simulator was beneficial in confirming this. By scaling the capillary pressure (eq. 3.9) in a heterogeneous system, the fluid phases are redistributed. In the regions with the highest saturation of hydrate S_H, the remaining pore space is filled with brine. Gas is present only as S_H decreases and the effective radii of the pores allow it. This fluid redistribution results in a system in which flow restrictions are caused by the reduction in intrinsic permeability caused by S_H and the development of capillary barriers. This is an important contribution to consider when designing core-flooding experiments in hydrate-bearing systems.

In terms of the capabilities of T+H, the main limitations of the simulator are the way it models the growth of the hydrate and the way that the reduction in permeability is modelled solely as a function of S_H. However, the flexibility of the porosity model and the use of stochastic distributions offer alternatives to explore improvements to either of these two limitations.

4.1.2 Effect of clay content on hydrate growth

Paper 2 focusses on the effect of clay content on methane gas hydrate phase transitions in unconsolidated sand at subsurface reservoir conditions (P = 83 bar and T = 5–8 °C). The results include both experiments and simulations of hydrate growth in two core setups. Each core setup consisted of an adjacent arrangement of different mixtures of unconsolidated sand and kaolin clay. To avoid sand production, sections of consolidated Bentheim sandstone were placed at both ends of each set-up (Figure 4.6).

Each core setup was saturated with a mixture of methane and brine. In Exp. 1, the fluids were arranged so that there was a continuous gas phase along the core setup (Figure 4.7 left at time = 0 h). Exp. 2 was set with a different distribution of fluids. On the left side of the core setup, S_W would be close to 100% and S_G would gradually increase towards the other end (Figure 4.7 right at time = 0 h). Hydrate formation was triggered by cooling each set-up and injecting methane to maintain pore pressure at 83 bar. The saturation of each phase was mapped using magnetic resonance imaging (MRI) at different stages of growth (Figure 4.7).

Experiments showed that hydrate growth was influenced by both the kaolin content and initial brine saturation S_{Wi}. In both experiments, growth started significantly earlier in the sections with the highest clay content (Figure 4.8 upper left). The near-homogeneous distribution of hydrate-forming fluids in Exp. 1 yielded a sequential increase of S_H that levelled after nearly the fiftieth hour, in similar magnitudes. In Exp. 2, the uneven distribution of S_W prior to hydrate formation affected the sequential growth pattern (Figure 4.7 right). Within the first

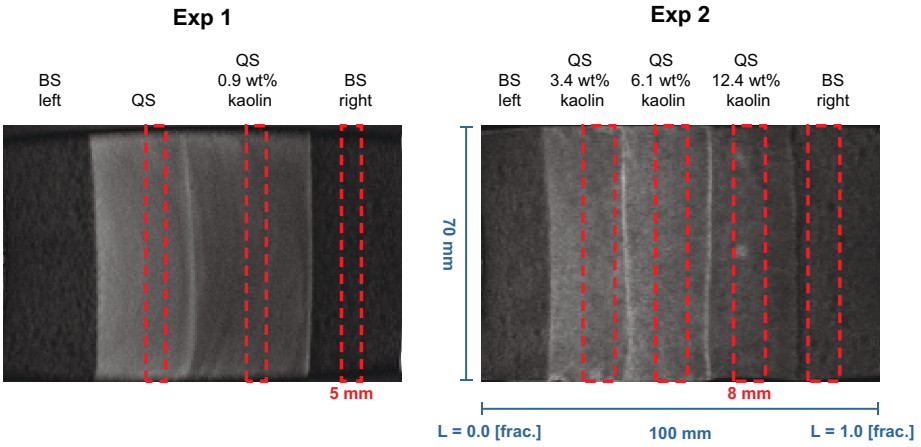

Figure 4.6: Sagittal view of quartz sand (QS) and Bentheim sandstone (BS) saturated with brine inside the core holder. The red dashed rectangles mark the position of the axial MRI slices that were used to analyze hydrate formation (5 mm thick for Exp. 1 and 8 mm thick for Exp. 2).

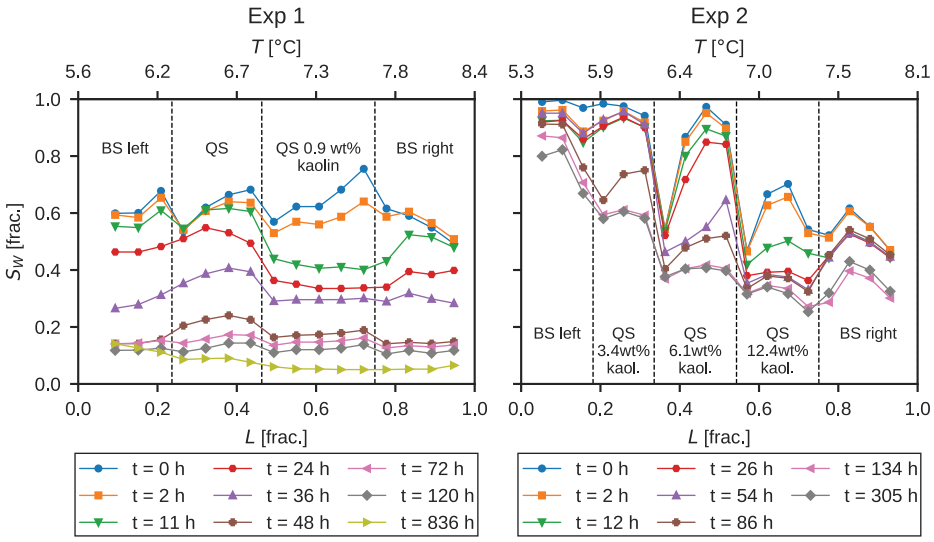

Figure 4.7: Change in water saturation during hydrate growth at constant pressure, P=83 bar for Exp. 1 (left) and Exp. 2 (right)

hours of the experiment, a sequential increase in S_H was also observed. However, despite having a higher kaolin content, within a few hours, the hydrate stopped in some sections and delayed in others (Figure 4.8 top right). Unlike in Exp. 1, growth did not occur within the first 50 hours, but was extended over near 150 hours. These observations suggest that there could have been interference in the evolution of the hydrates on each core piece. To a lesser extent, these types of interference between core pieces can also be interpreted from the Exp 1 results, where growth in the core piece with the highest clay content stagnates as soon as growth starts in the neighbouring pieces.

A similar strategy to **paper 1** was carried out for modelling. The core setup was represented by 1- and 2-dimensional grid representations. In T + H, the surface area A_S in eq. 3.4 is a function of the average grain radius of the sediment r_p, its porosity ϕ and hydrate saturation S_H at a given time:

$$A_S = \frac{1-\phi}{r_p} S_H^{2/3}$$

The grain radius r_p was used to incorporate the kaolin content of each mixture on the premise that a higher kaolin content results in a smaller average particle size r_p and a larger surface area A_S.

The numerical model for Exp 1 reproduced the sequential growth of hydrates driven by particle size (Figure 4.8 bottom left) observed in the experiments. In addition, the numerical model for Exp. 2 showed the effect of combining this mechanism with a system with a heterogeneous distribution of brine (Figure 4.8 bottom right). However, the models did not reproduce the interference observed between core pieces. The limitations encountered can be related in part to the limited data available for characterising the transport properties and grain size distribution, and in part to limitations in T+H for representing physical mechanisms observed in the experiments.

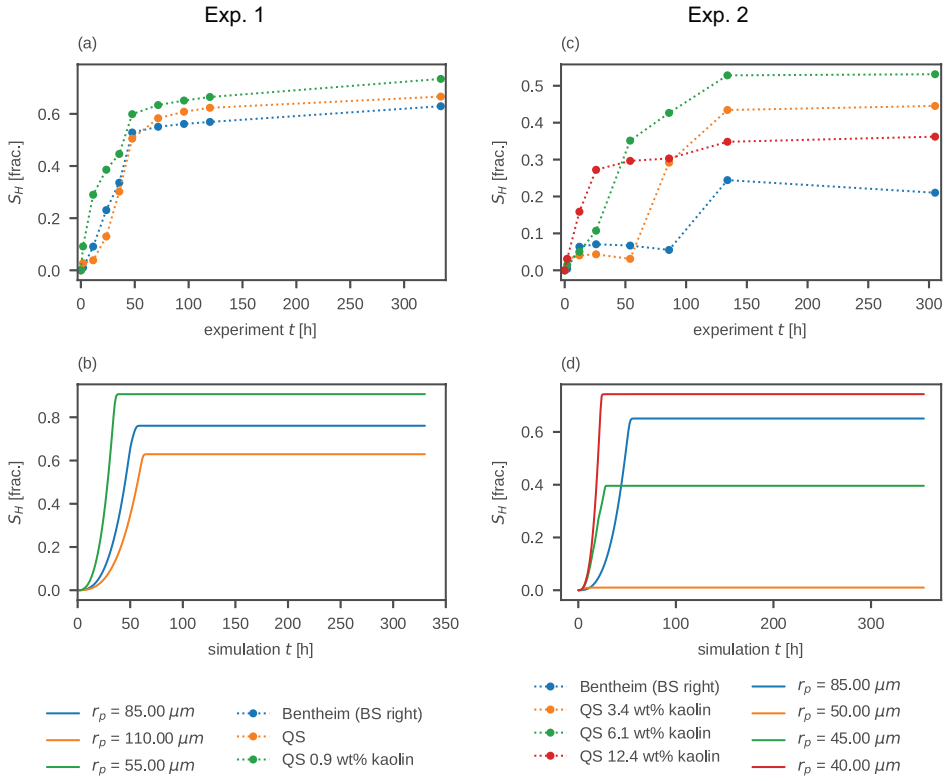

Figure 4.8: Time development of hydrate saturation at each core piece for Exp. 1 (left) and Exp. 2 (right). Top charts (*a* and *c*) show the experimental measurements. Bottom charts (*b* and *d*) show the simulated simulated hydrate saturation for the corresponding sections of each experiment.

As observed in **paper 1**, a heterogeneous distribution of hydrates can reduce the effective permeability of a porous system by clogging the system with solid hydrates or developing capillary barriers. The modelling in this study focused on hydrate formation, and the simulation of these processes did not consider stochastic nucleation and was constrained by the way T+H models hydrate formation. This resulted in a system that was mainly limited by the relative permeability of the gas k_{rG}. In simulations of Exp. 1, the homogeneous distribution of fluid phases allows the growth of hydrates to occur without major restrictions (Figure 4.9 top). However, in the simulations for Exp 2, the sections with high S_{Wi}, despite having a r_p that favours the formation of hydrates earlier than other sections, faced a limitation in mass transfer caused mainly by the high S_W (Figure 4.9 bottom).

In terms of mass balance, both 2D models were able to reach a final bulk hydrate saturation comparable to that acquired in the experiments (Figure 4.10. The discrepancies were mainly

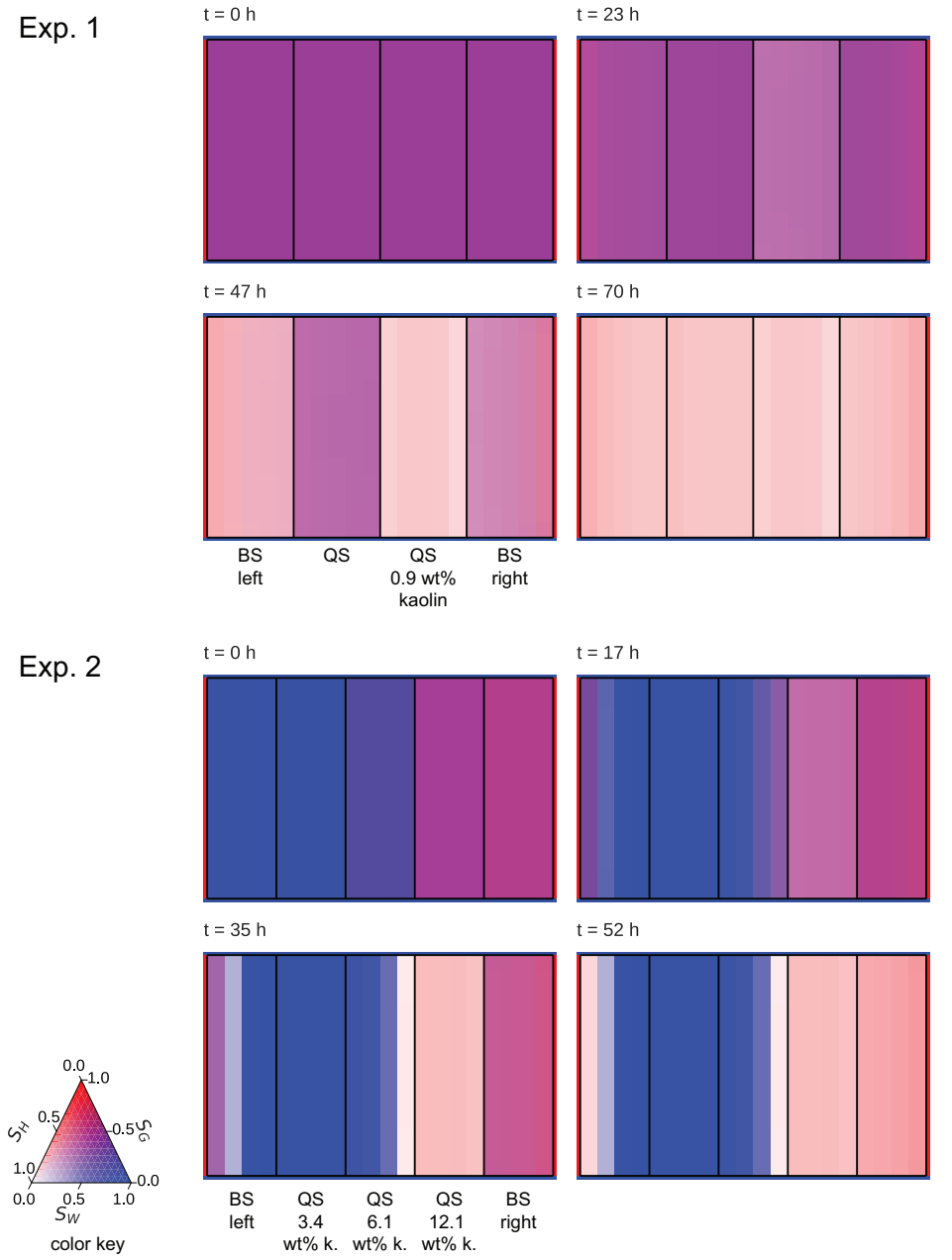

Figure 4.9: Visualization of 2D-simulation results at different points in time for Exp. 1 (top) and Exp. 2 (bottom) . The color shade is proportional to the saturation of each phase. Hydrate (white), brine (blue) and gas (red). The last visualization is shown when hydrate growth has reached a steady-state.

at the core-piece level. Although the modelled systems were able to form as much hydrate as the experiments, they were unable to steer the internal fluid flow; therefore, the hydrate growth in each section would have replicated the experimental result. Potentially, better characterisation of the transport properties of the materials may improve the quality of the modelled results. Both porosity, permeability, and capillary entry pressure are expected to change as more kaolin is added to the sand mixture. Hydrate saturation has a similar effect on the model, and coupling these effects can steer the internal fluid flow of the system and bring the model closer to the experiments. However, the inherent limitations of T+H still constrain the final results of the model. In addition to the inability to produce a stochastic growth of hydrate, T+H is built to model hydrates in consolidated porous systems. Although addressing these limitations will offer a better constrained construction of the models, there is no guarantee that the modelling approach can circumvent the complexities of modelling hydrates in porous media. Despite their limitations, simplified models are still useful for mapping out constrained and unconstrained processes that impact experimental results.

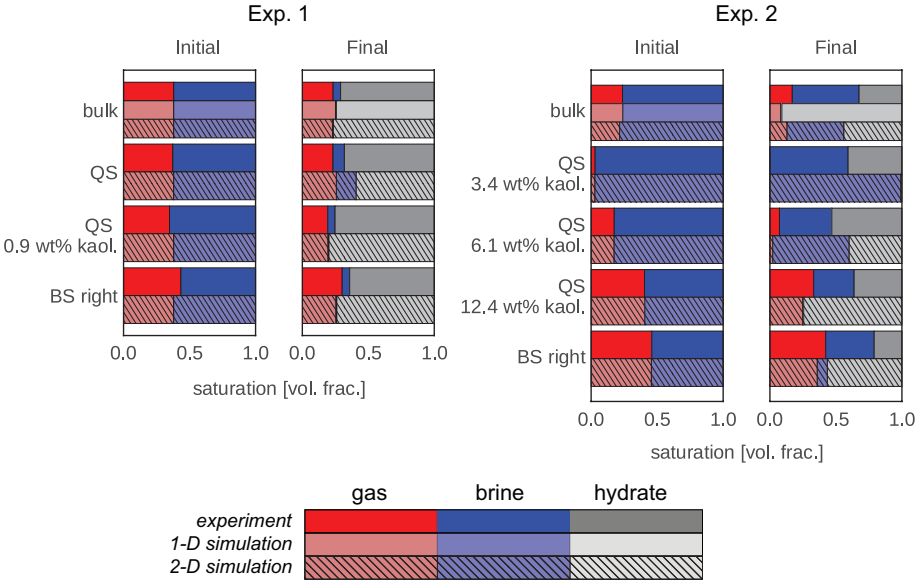

Figure 4.10: Comparison of average phase saturations yielded by experiments and simulations for the entire core setup (bulk) and each core piece. Initial values prior to hydrate formation in left and final post-hydrate formation values on right. Experimental measurements in bold colors, 1-D simulation results in lighter colors and 2-D simulation results in dashed colors.

4.2 Modelling hydrates in nature

The scope of this section is to present the results of modelling hydrates on a basin scale. The temporal and spatial scales of **paper 3** include simulations that last thousands of years in sediment sections of several hundred metres thick (Figure 4.1).

4.2.1 Evolution of hydrates during sedimentation

Paper 3 focusses on how the physical form of a hydrate occurrence evolves over long periods of time, in response to changes in its boundary conditions. Unlike **paper 1** and **2**, the scale and scope of this study justify the use of the equilibrium model (EM) of T+H ((eqs. 3.2, and 3.1). The hydrate occurrence was modelled and subjected to changes in its boundary conditions. These changes were set to emulate the deposition of sediments on the seafloor. All variations in temperature, pressure, phase saturation, and concentration of soluble components among other parameters were tracked over time.

The use of pre- and post-processing tools was essential to design the methodology for emulating a sedimentation process in T+H. Being a reservoir simulator, in a simple simulation, the grid remains static. Using the scripts, it was possible to run multiple simulations in sequence, where each simulation's output would serve as the input parameter of the next iteration. The duration of each simulation represented the time necessary to deposit a grid cell thickness at a given sedimentation rate.

The deposition of new sediment layers in the model displaced the geothermal gradient and induced the melting of the hydrate occurrence. As the sedimentation continued, the hydrate occurrence shoaled in cycles of slow melting interspersed with cycles of rapid reformation. Each cycle was transformed into a transient system driven by the heating rate (sedimentation rate) but constrained by variations in salinity and effects of hydrate saturation on the sediment transport properties.

Conventionally, the theoretical thickness of the GSHZ is defined by assuming a constant salinity and a linear gradient of temperature and hydrostatic pressure, the latter being used interchangeably as a proxy for depth [Collett, 2002]. In the transient systems observed in this study, salinity, pressure, and temperature experienced local variations that redefined the base GHSZ over time. During melting, hydrate dissociation resulted in an excess in the pore pressure caused by gas and hydrate filling the pores. This overpressure and the dilution of the salinity of the brine made the system more favourable to extend the preservation of the hydrates. Resulting in a progressively thicker GHSZ. The cycle was completed when the gas pressure surpassed the capillary entry pressure of the hydrate-bearing sediments and quickly migrated

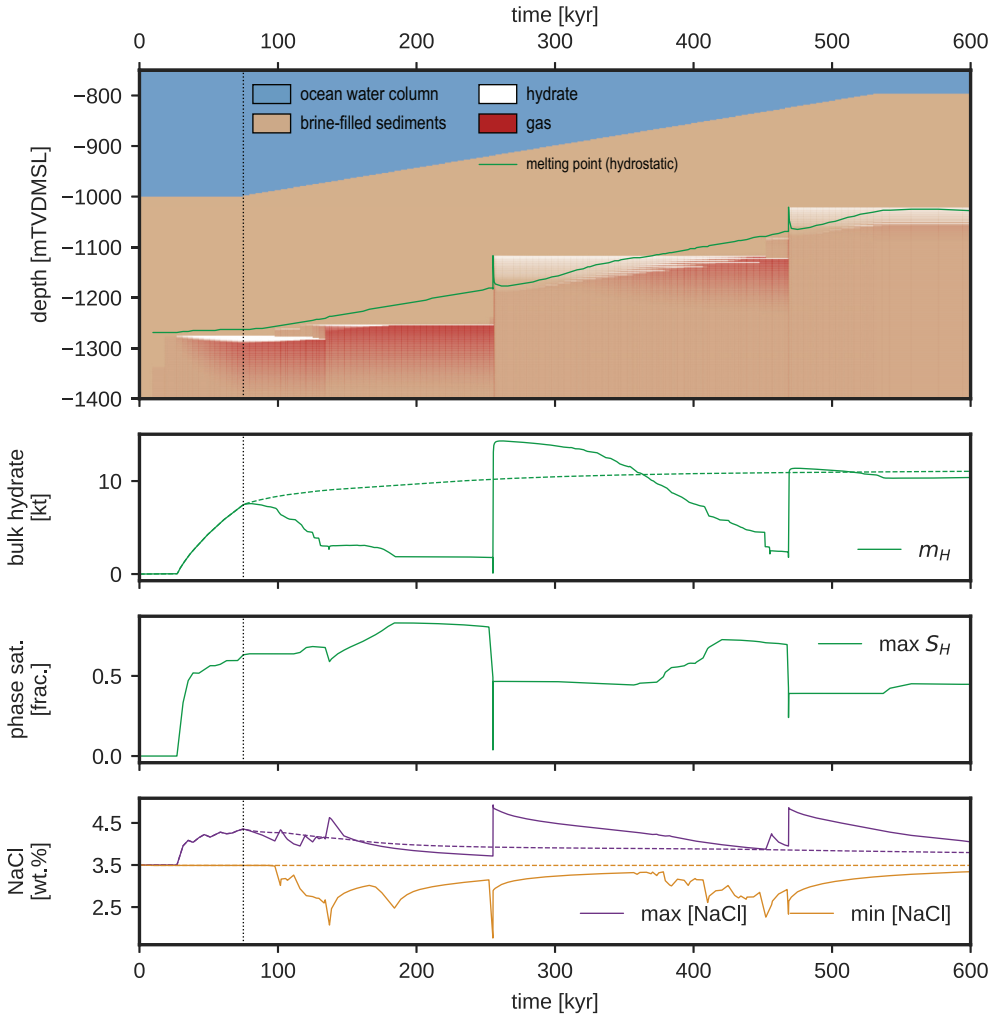

Figure 4.11: Evolution of hydrate occurrence during sedimentation (220 m/kyr). From top to bottom, the first chart shows the 1-D evolution through time of hydrate (white) and gas (red) saturation. The green line shows the depth at which the temperature and pressure matches the melting point at the given conditions. The second chart shows the bulk mass of hydrate through time during sedimentation (continuous) and with no sedimentation (stippled, Case 2). The third chart shows the maximum hydrate saturation reached at each point in time. The fourth and last chart shows the maximum (purple) and minimum (orange) salinity during sedimentation (continuous) and with no sedimentation (stippled).

upward. During the hydrate reformation cycles, the excess heat brought by the gas and the increase in salinity shrinked the GHSZ and brought it closer to the theoretical values.

An important contribution of this study is the development of a methodology for modelling hydrates in evolving systems where sedimentation plays a major role. Numerical simulation is a useful tool for keeping track of all of the variables involved in the hydrate transition phases and the transport of heat and mass. In complex systems such as those observed in this study, it becomes a powerful tool for understanding the mechanisms behind the thermodynamic evolution of a hydrate occurrence over geological time. However, there are still limitations inherent to T+H that constrain the capacity of this methodology. Although it was possible to emulate the sedimentation process by stacking layers and updating the boundary conditions, the mechanical compaction of sediments that results in sediment deposition and burial was not represented. Sediment compaction results in a system in which the transport properties change spatially and temporally. This could produce more complexity in the melting and reformation patterns observed in this study. Addressing the mechanical properties of unconsolidated systems also includes processes related to the formation of hydrates in these types of materials. In fine-grained sediments, hydrates can form nodules and lenses that mechanically displace grains [Jang and Santamarina, 2016]. These processes can also have an impact on the effective transport properties of the system.

Another contribution is related to the interpretation of hydrate occurrences in marine sediments. Identification of bottom-simulating reflectors (BSRs) is usually associated with the base of the GHSZ. This study shows that in systems with active sedimentation, the position of the BSR can change over time and does not correspond to the theoretical base of GHSZ.

Chapter 5

Conclusions and further work

5.1 Conclusions

Together, these results show the value of using numerical simulators as a tool to model hydrate-related processes at different temporal and spatial scales.

- Despite the limitations of the tool to reproduce all processes related to the formation and dissociation of hydrates, it is still possible to set up verification studies focussing on specific processes. These studies also provide an opportunity to inspect the capabilities of the simulator.
- Numerical simulations provide insight on the complexity of hydrate-bearing porous systems. By tracking all variables and components, it is possible to confirm that the formation and dissociation of hydrates in porous media result in a dynamic system in which multiple processes occur simultaneously. At different scales, some processes become more important than others.
- Simulations can provide explanations for processes that are not fully understood due to a lack of data or information. On the laboratory scale, the experimental apparatus does not monitor all physical and chemical processes. On a large scale, present-day observations of natural hydrate occurrences provide limited information on the processes that lead to its formation. In these scenarios, the simulator can provide alternative explanations for missing details that hinder the full interpretation of the processes.
- The evolving porosity model of T+H is a flexible model that addresses the effects of a changing porous system. Although it is solely a function of hydrate saturation that does not consider the habit and texture of a hydrate-bearing porous system, it sets the founda-

tion for understanding how hydrates can become flow barriers and steer the transfer of fluids through porous systems.

5.2 Further work

- To connect multiple scales, it is necessary to include scales beyond the range presented in this study and that fill the gap between the laboratory and basin scales. The results of modelling the methane production from hydrates can contribute to this approach. Once a richer spectrum of both temporal and spatial scales is covered, a dimensionless analysis can improve the understanding of which mechanisms dominate the transfer of heat and mass at each scale.

- The results of this study are a building block for understanding the effects of hydrate formation on the transport properties of porous systems. However, there is still a gap in incorporating the interaction between hydrate formation-dissociation and the mechanical properties of unconsolidated systems. The porosity model used to reduce porosity and permeability as a function of saturation is flexible to cover different scenarios. However, the changes in transport properties are fully reversible; as the hydrate melts, the transport properties revert to their intrinsic values. This can be an acceptable approximation for consolidated systems like those addressed in **paper 1**. However, in unconsolidated systems such as those studied in **paper 2** and **paper 3**, the formation of hydrates can displace grains, segregate and form hydrate lenses or nodules [Jang and Santamarina, 2016]. With the melting of the hydrates, the changes caused by the development of these lenses and nodules can leave an imprint on the sediments, changing the porous system and its transport properties. Although the introduction of the complexity of nodules and lens formation goes beyond the scope of T + H, introducing hysteresis into the porosity model can be a valid approximation.

- The learnings from **paper 1** and **paper 2** can be combined. With a better characterisation of the sediment transport properties, the simulated hydrate growth can be conditioned by a stochastic distribution of hydrates. With this approach, new modelled scenarios that consider both clay content and heterogeneity in hydrate saturation can address the limitations in **paper 2** to fully reproduce the experiments.

- In modelling large-scale systems, it may be relevant to include the mechanical behaviour of sediments. Not only to model the already mentioned mechanisms linked to the formation of hydrates in fine-grained sediments, but also to include the compaction of sediments. As sediments are buried over time, porosity and permeability change actively and this can bring a new layer of complexity to the processes observed in **paper 3**.

Bibliography

S. Almenningen, J. Gauteplass, L. P. Hauge, T. Barth, M. A. Fernø, and G. Ersland. Measurements of ch4 and co2 relative permeability in hydrate-bearing sandstone. *Journal of Petroleum Science and Engineering*, 177:880–888, 2019. ISSN 09204105. doi: 10.1016/j.petrol.2019.02.091.

Y. C. Beaudoin, W. Waite, R. Boswell, and S. R. Dallimore. *Frozen Heat: A UNEP Global Outlook on Methane Gas Hydrates Volume 1*, volume 1. United Nations Environment Programme, Arendal, NORWAY, 2014. ISBN 978-92-807-3429-4. URL `https://wedocs.unep.org/20.500.11822/9355`.

A. Bello-Palacios. TH-PrePost: Pre- and post-processing Python scripts for TOUGH+HYDRATE, 11 2021. URL `https://github.com/Alejobep/TH_PrePost`.

R. Boswell and T. S. Collett. Current perspectives on gas hydrate resources. *Energy Environ. Sci.*, 4(4):1206–1215, 2011. ISSN 1754-5692. doi: 10.1039/c0ee00203h. URL `https://dx.doi.org/10.1039/C0EE00203H`.

R. Boswell, T. Collett, S. Dallimore, and M. Frye. Geohazards associated with naturally-occurring gas hydrate. *Fire-In-The-Ice Methane Hydrate Newsletter*, 12(1):11e15, 2012.

BP. *Statistical Review of World Energy*. BP plc, London, UK, 2021a. URL `https://www.bp.com/content/dam/bp/business-sites/en/global/corporate/pdfs/energy-economics/statistical-review/bp-stats-review-2021-full-report.pdf`.

BP. *Energy Outlook 2020*. BP plc, London, UK, 2021b. URL `https://www.bp.com/content/dam/bp/business-sites/en/global/corporate/pdfs/energy-economics/statistical-review/bp-stats-review-2021-full-report.pdf`.

E. Burwicz, T. Reichel, K. Wallmann, W. Rottke, M. Haeckel, and C. Hensen. 3-d basin-scale reconstruction of natural gas hydrate system of the green canyon, gulf of mexico. *Geochemistry, Geophysics, Geosystems*, 18(5):1959–1985, 2017. ISSN 1525-2027.

doi: https://doi.org/10.1002/2017GC006876. URL https://agupubs.onlinelibrary.wiley.com/doi/abs/10.1002/2017GC006876.

Calsep. Pvtsim, 2020. URL https://www.calsep.com/pvtsim-nova.

T. Collett, J.-J. Bahk, R. Baker, R. Boswell, D. Divins, M. Frye, D. Goldberg, J. Husebø, C. Koh, M. Malone, M. Morell, G. Myers, C. Shipp, and M. Torres. Methane hydrates in nature—current knowledge and challenges. *Journal of Chemical & Engineering Data*, 60 (2):319–329, 2015. ISSN 0021-9568. doi: 10.1021/je500604h. URL https://doi.org/10.1021/je500604h.

T. S. Collett. Energy resource potential of natural gas hydrates. *AAPG Bulletin*, 86(11):1971–1992, 2002. ISSN 0149-1423. doi: 10.1306/61eeddd2-173e-11d7-8645000102c1865d. URL https://doi.org/10.1306/61EEDDD2-173E-11D7-8645000102C1865D.

T. S. Collett. Gas hydrate production testing – knowledge gained. In *Offshore Technology Conference*, volume Day 3 Wed, May 08, 2019, D031S035R002, 2019. doi: 10.4043/29516-ms. URL https://doi.org/10.4043/29516-MS.

S. Dai and Y. Seol. Water permeability in hydrate-bearing sediments: A pore-scale study. *Geophysical Research Letters*, 41(12):4176–4184, 2014. ISSN 0094-8276. doi: https://doi.org/10.1002/2014GL060535. URL https://agupubs.onlinelibrary.wiley.com/doi/abs/10.1002/2014GL060535.

I. K. Gamwo and Y. Liu. Mathematical modeling and numerical simulation of methane production in a hydrate reservoir. *Industrial & Engineering Chemistry Research*, 49(11):5231–5245, 2010. ISSN 0888-5885. doi: 10.1021/ie901452v. URL https://doi.org/10.1021/ie901452v.

J. C. Gill and M. Smith. *Geosciences and the Sustainable Development Goals*. Sustainable Development Goals Series. Cham: Springer International Publishing AG, Cham, 2021. ISBN 9783030388140,303038814X.

A. Hassanpouryouzband, E. Joonaki, M. Vasheghani Farahani, S. Takeya, C. Ruppel, J. Yang, N. J. English, J. M. Schicks, K. Edlmann, H. Mehrabian, Z. M. Aman, and B. Tohidi. Gas hydrates in sustainable chemistry. *Chemical Society Reviews*, 49(15):5225–5309, 2020. ISSN 0306-0012. doi: 10.1039/C8CS00989A. URL http://dx.doi.org/10.1039/C8CS00989A.

L.-J. HE, X.-L. LEI, and Y. ZHANG. Numerical modeling of gas hydrate accumulation in the marine sediments of shenhu area, northern south china sea. *Chinese Journal of Geophysics*, 54(3):299–306, 2011. ISSN 0898-9591. doi: https://doi.org/10.1002/cjg2.1612. URL https://agupubs.onlinelibrary.wiley.com/doi/abs/10.1002/cjg2.1612.

IEA. *World Energy Outlook 2021*. International Energy Agency, Paris, France, 2021. URL https://www.iea.org/reports/world-energy-outlook-2021.

IPCC. *Summary for Policymakers*, page 32. World Meteorological Organization,, Geneva, Switzerland, 2018.

J. Jang and J. C. Santamarina. Hydrate bearing clayey sediments: Formation and gas production concepts. *Marine and Petroleum Geology*, 77:235–246, 2016. ISSN 02648172. doi: 10.1016/j.marpetgeo.2016.06.013.

G. Jin, H. Lei, T. Xu, X. Xin, Y. Yuan, Y. Xia, and J. Juo. Simulated geomechanical responses to marine methane hydrate recovery using horizontal wells in the shenhu area, south china sea. *Marine and Petroleum Geology*, 92:424–436, 2018. ISSN 0264-8172. doi: https://doi.org/10.1016/j.marpetgeo.2017.11.007. URL https://www.sciencedirect.com/science/article/pii/S0264817217304415.

H. C. Kim, P. R. Bishnoi, R. A. Heidemann, and S. S. H. Rizvi. Kinetics of methane hydrate decomposition. *Chemical Engineering Science*, 42(7):1645–1653, 1987. ISSN 00092509. doi: 10.1016/0009-2509(87)80169-0.

M. B. Kowalsky and G. J. Moridis. Comparison of kinetic and equilibrium reaction models in simulating gas hydrate behavior in porous media. *Energy Conversion and Management*, 48 (6):1850–1863, 2007. ISSN 01968904. doi: 10.1016/j.enconman.2007.01.017.

M. C. Leverett. Capillary behavior in porous solids. *Transactions of the AIME*, 142(01): 152–169, 1941. ISSN 0081-1696. doi: 10.2118/941152-g.

B. Li, X.-S. Li, and G. Li. Kinetic studies of methane hydrate formation in porous media based on experiments in a pilot-scale hydrate simulator and a new model. *Chemical Engineering Science*, 105:220–230, 2014. ISSN 0009-2509. doi: https://doi.org/10.1016/j.ces.2013.11.016. URL https://www.sciencedirect.com/science/article/pii/S0009250913007513.

B. Li, X.-S. Li, G. Li, and Z.-Y. Chen. Evaluation of gas production from qilian mountain permafrost hydrate deposits in two-spot horizontal well system. *Cold Regions Science and Technology*, 109:87–98, 2015. ISSN 0165-232X. doi: https://doi.org/10.1016/j.coldregions.2014.08.002. URL https://www.sciencedirect.com/science/article/pii/S0165232X14001359.

J. Liu, M. Haeckel, J. Rutqvist, S. Wang, and W. Yan. The mechanism of methane gas migration through the gas hydrate stability zone: Insights from numerical simulations. *Journal of Geophysical Research: Solid Earth*, 124(5):4399–4427, 2019. ISSN 2169-9313. doi: https://doi.org/10.1029/2019JB017417. URL https://agupubs.onlinelibrary.wiley.com/doi/abs/10.1029/2019JB017417.

Y. Masuda. Numerical calculation of gas production performance from reservoirs containing natural gas hydrates. In *Annual Technical Conference, Soc. of Petrol. Eng., San Antonio, Tex., Oct. 1997*, 1997.

R. Matsumoto, Y. Kakuwa, G. Snyder, M. Tanahashi, A. Hiruta, T. Oi, S. Ohkawa, H. Tomaru, H. Numanami, C. Shen, and S. Morita. Occurrence and origin of thick deposits of massive gas hydrate, eastern margin of the sea of japan. In *The Ninth International Conference on Gas Hydrates, ICGH9*, 2017.

G. Moridis. User's manual for the hydrate v1. 5 option of tough+ v1. 5: A code for the simulation of system behavior in hydrate-bearing geologic media. report lbnl-6869e. Report, Lawrence Berkeley National Laboratory. Berkeley, California US., 2014. URL https://tough.lbl.gov/assets/files/02/documentation/TH_Manual_v1.5s.pdf.

G. Moridis and K. Pruess. User's manual of the tough+ v1. 5 core code: A general purpose simulator of non-isothermal flow and transport through porous and fractured media. Report, Lawrence Berkeley National Laboratory. Berkeley, California US., 2014. URL https://tough.lbl.gov/assets/files/02/documentation/TC_Manual_v1.5s.pdf.

G. J. Moridis, T. S. Collett, S. R. Dallimore, T. Satoh, S. Hancock, and B. Weatherill. Numerical studies of gas production from several ch4 hydrate zones at the mallik site, mackenzie delta, canada. *Journal of Petroleum Science and Engineering*, 43(3):219–238, 2004. ISSN 0920-4105. doi: https://doi.org/10.1016/j.petrol.2004.02.015. URL https://www.sciencedirect.com/science/article/pii/S0920410504000464.

C. K. Paull, R. Matsumoto, P. J. Wallace, and W. P. Dillon. *Proceedings of the Ocean Drilling Program, 164 Scientific Results*. Proceedings of the Ocean Drilling Program. Ocean Drilling Program, 2000. doi: 10.2973/odp.proc.sr.164.2000. URL https://doi.org/10.2973%2Fodp.proc.sr.164.2000.

E. Piñero, C. Hensen, M. Haeckel, W. Rottke, T. Fuchs, and K. Wallmann. 3-d numerical modelling of methane hydrate accumulations using petromod. *Marine and Petroleum Geology*, 71:288–295, 2016. ISSN 0264-8172. doi: https://doi.org/10.1016/j.marpetgeo.2015.12.019. URL https://www.sciencedirect.com/science/article/pii/S0264817215301677.

M. Riedel, T. S. Collett, and M. Malone. *Expedition 311 Synthesis: scientific findings*, book section Scientific findings. Proceedings of the IODP. Integrated Ocean Drilling Program Management International, Inc., 2010. doi: 10.2204/iodp.proc.311.213.2010.

C. Ruppel. Permafrost-associated gas hydrate: Is it really approximately 1 % of the global system? *Journal of Chemical & Engineering Data*, 60(2):429–436, 2015. ISSN 0021-9568. doi: 10.1021/je500770m. URL https://doi.org/10.1021/je500770m.

C. D. Ruppel and J. D. Kessler. The interaction of climate change and methane hydrates. *Reviews of Geophysics*, 55(1):126–168, 2017. ISSN 8755-1209. doi: https://doi.org/10.1002/2016RG000534. URL https://agupubs.onlinelibrary.wiley.com/doi/abs/10.1002/2016RG000534.

E. D. Sloan. Fundamental principles and applications of natural gas hydrates. *Nature*, 426 (6964):353–359, 2003. ISSN 0028-0836. doi: 10.1038/nature02135. URL <GotoISI>://WOS:000186660800057.

E. D. Sloan and C. A. Koh. *Clathrate hydrates of natural gases*, volume 119 of *Chemical industries*. CRC Press, Boca Raton, Fla, 3rd ed. edition, 2008. ISBN 9780849390784,0849390788.

J. Sun, F. Ning, L. Zhang, T. Liu, L. Peng, Z. Liu, C. Li, and G. Jiang. Numerical simulation on gas production from hydrate reservoir at the 1st offshore test site in the eastern nankai trough. *Journal of Natural Gas Science and Engineering*, 30:64–76, 2016. ISSN 1875-5100. doi: https://doi.org/10.1016/j.jngse.2016.01.036. URL https://www.sciencedirect.com/science/article/pii/S187551001630035X.

Y. Teng and D. Zhang. Comprehensive study and comparison of equilibrium and kinetic models in simulation of hydrate reaction in porous media. *Journal of Computational Physics*, 404:109094, 2020. ISSN 0021-9991. doi: https://doi.org/10.1016/j.jcp.2019.109094. URL https://www.sciencedirect.com/science/article/pii/S0021999119307995.

A. M. Tréhu, G. Bohrmann, M. E. Torres, and F. S. Colwell. *Proceedings of the Ocean Drilling Program, 204 Scientific Results*. Proceedings of the Ocean Drilling Program. Texas A & M University Ocean Drilling Program, 2006. doi: 10.2973/odp.proc.sr.204.2006.

UN General Assembly. Transforming our world: The 2030 agenda for sustainable development. a/res/70/1, 2015. URL https://sdgs.un.org/publications/transforming-our-world-2030-agenda-sustainable-development-17981.

UNDP. *World Energy Assessment: Energy and the challenge of Sustainability*. United Nations Development Programme, 2000. URL https://www.undp.org/publications/world-energy-assessment-energy-and-challenge-sustainability.

USGS. Gas hydrates in marine sediments from the indian ocean, 2006. URL https://www.usgs.gov/media/images/gas-hydrates-marine-sediments-indian-ocean-0.

USGS. Gulf of mexico gas hydrate formation, 2017a. URL https://www.usgs.gov/media/images/gulf-mexico-gas-hydrate-formation.

USGS. Mallik gas hydrate sample, 2017b. URL https://www.usgs.gov/media/images/mallik-gas-hydrate-sample-0.

A. Verma and K. Pruess. Thermohydrological conditions and silica redistribution near high-level nuclear wastes emplaced in saturated geological formations. *Journal of Geophysical Research: Solid Earth*, 93(B2):1159–1173, 1988. ISSN 0148-0227. doi: https://doi.org/10.1029/JB093iB02p01159. URL https://agupubs.onlinelibrary.wiley.com/doi/abs/10.1029/JB093iB02p01159.

F. Wang, B. Zhao, and G. Li. Prevention of potential hazards associated with marine gas hydrate exploitation: A review. *Energies*, 11(9):2384, 2018. ISSN 1996-1073. URL https://www.mdpi.com/1996-1073/11/9/2384.

M. D. White, T. J. Kneafsey, Y. Seol, W. F. Waite, S. Uchida, J. S. Lin, E. M. Myshakin, X. Gai, S. Gupta, M. T. Reagan, A. F. Queiruga, S. Kimoto, R. C. Baker, R. Boswell, J. Ciferno, T. Collett, J. Choi, S. Dai, M. De La Fuente, P. Fu, T. Fujii, C. G. Intihar, J. Jang, X. Ju, J. Kang, J. H. Kim, J. T. Kim, S. J. Kim, C. Koh, Y. Konno, K. Kumagai, J. Y. Lee, W. S. Lee, L. Lei, F. Liu, H. Luo, G. J. Moridis, J. Morris, M. Nole, S. Otsuki, M. Sanchez, S. Shang, C. Shin, H. S. Shin, K. Soga, X. Sun, S. Suzuki, N. Tenma, T. Xu, K. Yamamoto, J. Yoneda, C. M. Yonkofski, H. C. Yoon, K. You, Y. Yuan, L. Zerpa, and M. Zyrianova. An international code comparison study on coupled thermal, hydrologic and geomechanical processes of natural gas hydrate-bearing sediments. *Marine and Petroleum Geology*, 120:104566, 2020. ISSN 0264-8172. doi: https://doi.org/10.1016/j.marpetgeo.2020.104566. URL https://www.sciencedirect.com/science/article/pii/S0264817220303494.

J. W. Wilder, G. J. Moridis, S. J. Wilson, M. Kurihara, M. D. White, Y. Masuda, B. J. Anderson, T. S. Collett, R. B. Hunter, and H. Narita. An international effort to compare gas hydrate reservoir simulators. In *Proceedings of 6th International Conference on Gas Hydrates (ICGH 2008), Vancouver, CANADA*, 2008.

WRI. Climate watch historical country greenhouse gas emissions data (1990-2018), 2021. URL https://www.climatewatchdata.org/ghg-emissions.

Y. Ye. *Introduction*, pages 1–18. Springer Berlin Heidelberg, Berlin, Heidelberg, 2013. ISBN 978-3-642-31101-7. doi: 10.1007/978-3-642-31101-7_1. URL https://doi.org/10.1007/978-3-642-31101-7_1.

Z. Yin and P. Linga. Methane hydrates: A future clean energy resource. *Chinese Journal of Chemical Engineering*, 27(9):2026–2036, 2019. ISSN 1004-9541. doi: https://doi.org/10.1016/j.cjche.2019.01.005. URL https://www.sciencedirect.com/science/article/pii/S1004954118317166.

Z. Yin, G. Moridis, H. K. Tan, and P. Linga. Numerical analysis of experimental studies of methane hydrate formation in a sandy porous medium. *Applied Energy*, 220:681–704, 2018. ISSN 0306-2619. doi: https://doi.org/10.1016/j.apenergy.2018.03.075. URL http://www.sciencedirect.com/science/article/pii/S0306261918304148.

K. You and P. B. Flemings. Methane hydrate formation and evolution during sedimentation. *Journal of Geophysical Research: Solid Earth*, 126(4), 2021. ISSN 2169-9313 2169-9356. doi: 10.1029/2020jb021235.

K. You, P. B. Flemings, A. Malinverno, T. S. Collett, and K. Darnell. Mechanisms of methane hydrate formation in geological systems. *Reviews of Geophysics*, 57(4):1146–1196, 2019. ISSN 8755-1209 1944-9208. doi: 10.1029/2018rg000638.

H. Zhu, T. Xu, Z. Zhu, Y. Yuan, and H. Tian. Numerical modeling of methane hydrate accumulation with mixed sources in marine sediments: Case study of shenhu area, south china sea. *Marine Geology*, 423:106142, 2020. ISSN 0025-3227. doi: https://doi.org/10.1016/j.margeo.2020.106142. URL `https://www.sciencedirect.com/science/article/pii/S002532272030030X`.

Appendix A

Scientific contributions

Paper I

A.1 Effects of methane hydrates on two-phase relative permeability in sandstone: Numerical simulation of laboratory experiments

Alejandro Bello-Palacios, Per Fotland, Stian Almenningen, and Geir Ersland

Journal of Petroleum Science and Engineering 208, **Part D** (2022)

Journal of Petroleum Science and Engineering 208 (2022) 109606

Contents lists available at ScienceDirect

Journal of Petroleum Science and Engineering

journal homepage: www.elsevier.com/locate/petrol

Effects of methane hydrates on two-phase relative permeability in sandstone: Numerical simulation of laboratory experiments

Alejandro Bello-Palacios [a,b,*], Per Fotland [a], Stian Almenningen [b], Geir Ersland [b]

[a] Equinor ASA, Bergen, Norway
[b] Department of Physics and Technology, University of Bergen, Norway

ARTICLE INFO

Keywords:
2-phase flow
Clathrates
TOUGH +HYDRATE
Verification

ABSTRACT

To identify the challenges and limitations in measuring and modelling gas relative permeability in hydrate bearing sandstone, we simulate a series of experiments. Experimental and numerical results are used to examine the amount of hydrates formed as well as how the flow of gas is affected by the hydrate formation. The reservoir simulator TOUGH +HYDRATE was used. The system is represented numerically in both 1-dimensional and 2-dimensional grids. The 1-dimensional simulations are used to check the system consistency by keeping track of the amount of hydrates that are formed, given the initial and boundary conditions. The 2-dimensional simulations are used to measure the effects of heterogeneity in the distribution of hydrates, and its impact on both relative permeability and capillary pressure. The results reveal complexities when comparing experimental and simulated permeability in hydrate-bearing systems. The results from the 1-dimensional calculations show that most experiments have not been able to form the amount of hydrates that is theoretically possible by the initial mix of brine and gas. This indicates that early growth of hydrates can limit mass transfer to inner parts of the core shielding the system for further nucleation. This is supported by the 2-dimensional simulations. These show how a heterogeneous pattern of hydrates can limit fluid flow by (a) reducing the intrinsic permeability, (b) scaling down gas relative permeability, and (c) and scaling up capillary entry pressure of portions of the core. Although these effects do not fully explain the experimental results, the results provide insight to hydrate induced flow restrictions and how these can affect experimental result.

1. Introduction

Gas hydrates are crystalline ice-like solids formed by the mixing of water and a gas under pressure. Water molecules form hydrogen-bonded structures with cavities that are stabilized by the filling of non-polar or slightly polar guest gas molecules (Sloan et al., 2007). Methane is the most common gas molecule that forms hydrates naturally. Besides the availability of both water and methane, low temperatures and high pressures are needed. Porous media in and below permafrost and near seafloor sediments in deep marine regions (water column higher than 400 m) meet these conditions and host most methane hydrate accumulations known in the world (Boswell, 2009). These accumulations have gained increased interest over the last four decades and multiple research initiatives are focusing on understanding their impact on safety in drilling operations, seafloor stability, climate change, geohazards, and its feasibility as a potential energy resource (Collett et al., 2014).

Natural or human induced changes in pressure and temperature will affect the stability of hydrates and may cause formation of hydrates or melting and reformation. This involves a dynamic transition between a system with 2 phase flow (gas and water) and 1 solid phase (hydrates).

Depending on whether the hydrates form or melt in a saline environment a number of changes take place; 1. heat is either consumed or released causing a temperature change 2. pressure may decrease or increase due to both gas and water consumption or release, 3. the salinity decreases or increases as water is consumed or released. All these mechanisms may have significant impact on the hydrate distribution and flow of fluids. To complicate matters even more there is an apparent stochastic nature to hydrate formation. Once hydrate nuclei are formed, they will consume nearby gas and water and grow until the driving forces are locally zero, due to lack of methane, water or an increased salinity. This may cause the overall formation to become patchy (Fig. 1). If in addition the porous medium is un-consolidated, the internal hydrate pressure of the small nuclei may be higher than the surrounding effective pressure and thereby grains can be moved and the patch may grow to become a single solid hydrate lens or vein (Jang and Santamarina, 2016).

In multi-phase flow, the saturation of each phase determines how it flows and inhibits the flow of the coexisting phases. This effect is

* Corresponding author.
E-mail address: gpb@equinor.com (A. Bello-Palacios).

https://doi.org/10.1016/j.petrol.2021.109606
Received 12 October 2020; Received in revised form 13 April 2021; Accepted 4 October 2021
Available online 12 October 2021

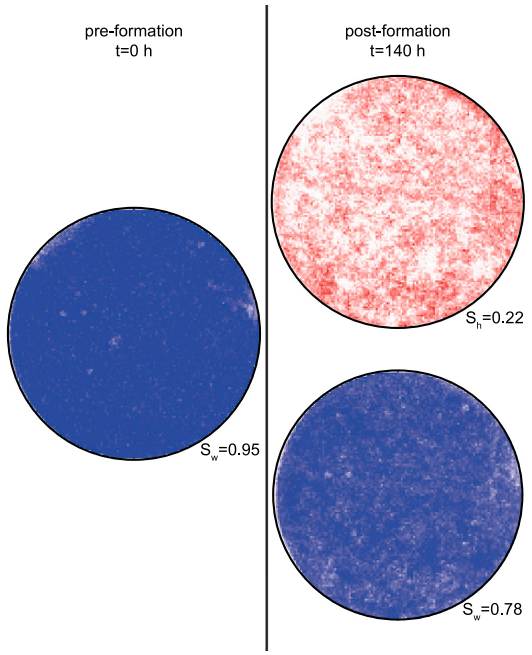

Fig. 1. MRI images of a cross-sectional slice of a Bentheim sandstone core. Images display phase saturations before (left) and after (right) hydrate formation. Post-formation phase saturation is resolved for both hydrates (red) and brine (blue). Hydrate saturation (top right) shows a heterogeneous stochastic ("patchy") pattern.

described by the phase relative permeability. Reliable relative permeability estimates are central to the accuracy of numerical predictions of flow in porous media (Kleinberg et al., 2003).

In terms of laboratory experiments, the most common technique for permeability measurements is the steady state flow test (Li et al., 2018). The complexities of multi-phase flow in hydrate bearing systems makes the measurement of relative permeability particularly difficult. Every phase affects each other while the intrinsic permeability of the medium actively changes. In addition, though pressure and temperature must be maintained during tests, it is very hard to avoid hydrate re-formation and dissociation (Moridis et al., 2010). The number of studies published is low (Jaiswal, 2004; Ahn et al., 2005; Johnson et al., 2011; Almenningen et al., 2019) and include a variety of methods and materials. Ren et al. (2020) concludes that the variability between these studies reveals a lack of repeatability and a challenge of making their results comparable.

Almenningen et al. (2019) published a series of measurements of gas relative permeability in carbon dioxide (CO_2) and methane (CH_4) hydrate bearing sandstone. The experiment setup considered varying saturations of both gas and brine, expecting to measure the effect of the presence of both hydrates and the fluid phases. Results show a clear but highly scattered decreasing trend of gas permeability with increasing hydrate saturation. It is suggested that this effect can be related to methane becoming disconnected by hydrate films that form local barriers of flow and that the distribution of such flow barriers vary between experiments.

In terms of combining experimental studies on hydrate bearing porous media with numerical models, there has been relatively few studies. Jang and Santamarina (2014) used numerical modelling to reproduce permeability and capillary pressure relationships monitored through hydrates in micromodels. Chen et al. (2018), used numerical models to calculate gas relative permeability as a function of hydrate distribution obtained from X-ray microtomography images from hydrate bearing sandpacks.

To estimate bulk phase saturations in laboratory measurements involving hydrate formation or dissociation of porous media, exchange of fluids along with pressure and temperature are monitored. However, in the absence of tools that provide images that can distinguish solid hydrates from fluid phases, it is impossible to see how these phases are distributed internally.

Numerical modelling can assist the analysis of experimental measurements where the internal distribution of phases could have been critical in the quality of the physical measurement. Modelling can be critical to complement the work done in the laboratory and enable extrapolation of laboratory measurements to field-scale applications. Similarly, experimental results can assist constraining the models that define how the internal porous media is affected by the presence of hydrates. A good agreement between experimental data and numerical predictions is essential to bridge knowledge gaps and improve understanding of the complexity of gas hydrates systems (Birkedal et al., 2014).

To address this issue, we present the results of simulating 2-phase flow effective permeability experiments from Almenningen et al. (2019)) using TOUGH+HYDRATE (T+H).

- Firstly, we compare how suitable T+H is to reproduce the process of hydrate formation after cooling down pressurized gas and brine.
- Secondly, we evaluate how T+H can help to understand processes that were not possible to observe during the experimental work. Particularly on the internal distribution of both solid and fluid phases on the effective gas flow. This includes how a stochastic hydrate growth affects both capillary pressure and intrinsic permeability.
- Finally, with the results obtained in this work we aim to map out potential caveats and limitations that can be encountered when designing experiments that involve hydrates in porous media.

2. Methods

The dataset used for this work consists of end-point gas relative permeability measurements in sandstone, before and after hydrate formation (Almenningen et al., 2019) (Table 1). A set of cylindrical sandstone cores initially saturated with methane gas and brine (3.5 wt% NaCl) were connected to flowlines on each end of the core to provide the necessary influx to pressurize the core and measure relative permeability. A cooling jacket was used to cool down the core and induce the formation of hydrates at constant pressure.

Each experiment produced a relative permeability measurement before and after hydrate formation (Fig. 2). Hydrate saturation achieved after cooling was between 37% and 61%. The relative permeability due to hydrate formation was decreased by 1 to 5 orders of magnitude.

To model these results, TOUGH+HYDRATE v1.5 (T+H) was used. T+H is a numerical code for the simulation of the behaviour of methane hydrate-bearing geologic systems for multi-phase, multi-component flow and transport of mass and heat through porous and fractured media (Moridis and Pruess, 2014).

Hydrate formation and dissociation are modelled in T+H by using either an equilibrium or a kinetic model. In the equilibrium model, phase transitions are governed only by pressure and temperature. Water and methane are mass components, and hydrate is one of the potential phases that can be present in different combinations (Fig. 3). In the kinetic model, hydrates are treated as a new mass component. Phase transitions are calculated by kinetic parameters in an Arrhenius-type expression based on the work of Kim et al. (1987). Eq. (1) describes the behaviour of the hydrate mass component and phase.

$$\frac{\partial M}{\partial t} = K_0 e^{(-\Delta E_a/RT)} F_A \; A_S \; (f_{eq} - f_v) \tag{1}$$

Table 1
List of all CH_4 permeability experiments (Almenningen et al., 2019). Core pressure and temperature were kept constant at 8.3 MPa and 4 °C, respectively, during hydrate formation and permeability measurements. Margin of errors reflect instrumental uncertainties. (For interpretation of the references to colour in this figure legend, the reader is referred to the web version of this article.)

Exp. ID	No hydrate		Hydrate		
	S_g [frac.] ±0.01	k_{rg} [frac.]	S_{hyd} [frac.] ±0.02	S_g [frac.] ±0.02	k_{rg} [frac.]
A	0.54	0.12 ± 0.02	0.46	0.44	1.9E−2 ± 0.3E−2
B	0.47	0.19 ± 0.08	0.47	0.36	1.2E−3 ± 0.4E−3
C	0.46	0.09 ± 0.03	0.45	0.36	1.7E−6 ± 0.6E−6
D	0.46	0.06 ± 0.02	0.47	0.36	4E-6 ± 1E−6
E	0.46	0.06 ± 0.02	0.51	0.35	1.4E−4 ± 0.5E−4
F	0.36	0.08 ± 0.03	0.61	0.23	4E-7 ± 1E−7
G	0.36	0.14 ± 0.02	0.53	0.24	9.9E−7 ± 0.8E−7
H	0.27	0.032 ± 0.006	0.37	0.18	7.1E−7 ± 0.8E−7

S_g and S_{hyd} are the gas and methane saturations, respectively; k_{rg} is the relative permeability of gas.

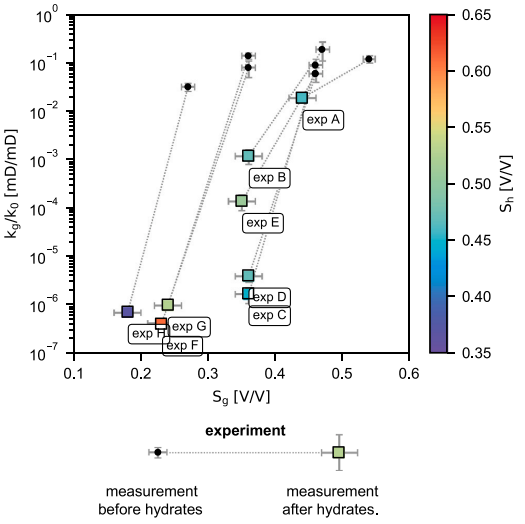

Fig. 2. Overview of all the methane relative permeability measurements and margin of errors. Black circles show gas relative permeability before hydrate formation. Coloured squares show relative permeability after hydrate formation. Colour shade in squares represents hydrate saturation. Stippled lines connect measurements in each experiment. (For interpretation of the references to colour in this figure legend, the reader is referred to the web version of this article.)

Where $^{\partial M}/_{\partial t}$ is the methane mass rate, K_0 the intrinsic hydration reaction constant, ΔE_a the hydration activation energy, R is the universal gas constant, T is the temperature, F_A is the area adjustment factor, A_S is the hydrate reactive surface area, f_{eq} is the fugacity at equilibrium temperature and f_v is the fugacity in the gas phase at temperature T.

Kowalsky and Moridis (2007), Teng and Zhang (2020) have compared both modelling strategies. Kowalsky and Moridis (2007) concluded that they were practically indistinguishable for large-scale and long-term processes, but that Kinetic model would more suitable for short-term and core-scale simulations. Teng and Zhang (2020) conclude that the equilibrium model is a special case of kinetic model where the relative strength of the hydrate reaction is greater than that of other physical processes. The authors also indicate that when such strength is relatively smaller than other physical processes, the kinetic model can be more computationally efficient. Birkedal et al. (2014) observed that the kinetic model was less sensitive to temperature variations at the boundary condition and was more numerically efficient.

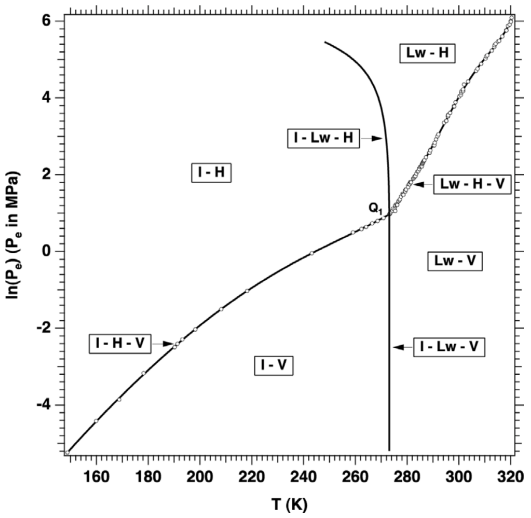

Fig. 3. Pressure–temperature equilibrium relationship in the phase diagram of the water–methane–hydrate system. All possible combinations of the four phases are displayed: aqueous (Lw), ice (I), gas (V), and hydrate (H) (Moridis and Pruess, 2014).

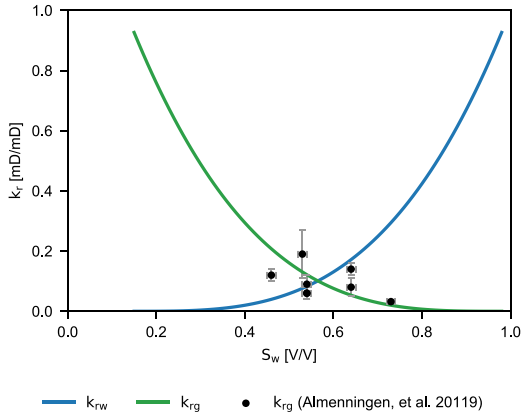

Fig. 4. 2-phase relative permeability curves used in this study based on the modified Stone model. k_w, k_r are water and gas relative permeability, respectively. Overlaid, 2-phase gas relative permeability measurements, prior to hydrate formation (Almenningen et al., 2019).

Water and gas flow in hydrate bearing rocks is governed by fluid saturations and the reduction in porosity due to hydrate formation. T+H handles this by using separate models that define two-phase relative permeability and growth of solid (hydrate). For relative permeability, the modified Stone model was used in T+H. It is a power-law relationship between the relative permeability of the fluid phase (k_{rw}, k_{rg}) and the saturation of the phase (S_w, S_g) (Fig. 4), defined by Eqs. (2) and (3).

$$k_{rw} = \frac{k_w}{k_0} = \left(\frac{S_w - S_{rw}}{1 - S_{rw}}\right)^{n_w} \quad (2)$$

$$k_{rg} = \frac{k_g}{k_0} = \left(\frac{S_g - S_{rg}}{1 - S_{rw}}\right)^{n_g} \quad (3)$$

Table 2
TOUGH+H input parameters used for sandstone cores.

Parameter	Magnitude
Porosity [V/V]	$\phi_0 = 0.22$
Absolute permeability [D]	$k_0 = 1.3$–1.9
Initial salinity [wt.%]	$X_{inh} = 3.5$[a]–5.44[b]
Model for updating porosity and permeability	$m = 3$[a]
	$\phi_c = 0.05$[a]
Relative permeability. Modified Stone model	$S_{ira} = 0.15$, $S_{irg} = 0.05$[a]
	$n_a = 3.5$, $n_g = 3.2$[a]

[a]Values taken from Birkedal et al. (2014).
[b]Arbitrarily defined value to estimate highest reduction of permeability.

S_{rw} and S_{rg} are residual saturation of water and gas phases, respectively. Both these parameters and fitting exponents n_w, n_g define the shape and end-points of the curves (Fig. 2) and are to be defined by the user. The small amount of experiments yielded a scattered amount of relative permeability measurements (Fig. 2). There is no unique solution for the Stone model. Therefore, residual saturations and fitting exponents for both gas and water were taken from Birkedal et al. (2014) (Table 1).

The solid hydrate phase in T+H is modelled as an extension of the matrix. Effective or (hydrate-filled) porosity (ϕ) is a function of both the initial (hydrate-free) porosity (ϕ_0) and hydrate saturation (S_h). ϕ is defined as the porosity filled only by fluid phases, expressed in Eq. (4)

$$\phi = \phi_0 \, (1 - S_h) \tag{4}$$

As porosity is modified, intrinsic permeability k is also updated. T+H uses a permeability reduction factor k_{rF} that is obtained from a power law relationship (Eq. (5)) between the ratios of hydrate-filled porosity ϕ and the hydrate-free porosity ϕ_0. The reduction factor k_{rF} sets the ratio by which intrinsic (hydrate-free) permeability k_0 is decreased, and yields an effective (hydrate-filled) permeability k. The effective permeability k is the permeability of a single-phase fluid flowing in a porous medium with specific saturation of hydrate.

$$\left(\frac{k}{k_0}\right) = k_{rF} = \left(\frac{\phi - \phi_c}{\phi_0 - \phi_c}\right)^m \tag{5}$$

The critical porosity ϕ_c accounts for scenarios of hydrates clogging pore throats and disconnecting fluid-filled pores. It is defined by the product between the saturation of hydrates at which effective permeability is reduced to zero ($maxS_h$), and the hydrate-free porosity (ϕ_0). $\phi_c = \phi_0 \cdot (1 - maxS_h)$.

This approach is similar to the Tokyo model proposed by MASUDA (1997). In both models (Eqs. (5) and (6)), exponents m and N steer the rate by which permeability is reduced. No particular restrictions are given regarding the magnitude of parameters m and N. These fitting parameters accept a wide range of values aimed to make the models fit different scenarios (Fig. 5). Dai and Seol (2014) linked the magnitude of this parameter with pore habits and found that it can vary from $N = 1.25$ for sediments with uniform cementing hydrate, to $N = 25$ for sediments with uniform pore-filling hydrate.

$$\left(\frac{k}{k_0}\right) = (1 - S_h)^N \tag{6}$$

With the small number of measurements used in this study and the fact that all of them are done in the presence of three phases, it was impractical to attempt finding values for parameters m and ϕ_c. Therefore, base values were taken from Birkedal et al. (2014).

Regarding 2-phase flow, T+H keeps the relative permeability model unchanged. However, it uses hydrate saturation (S_h) and the permeability reduction factor (k_{rF}) to obtain the magnitude of effective fluid phase permeability. This involves normalizing the fluid flow saturations

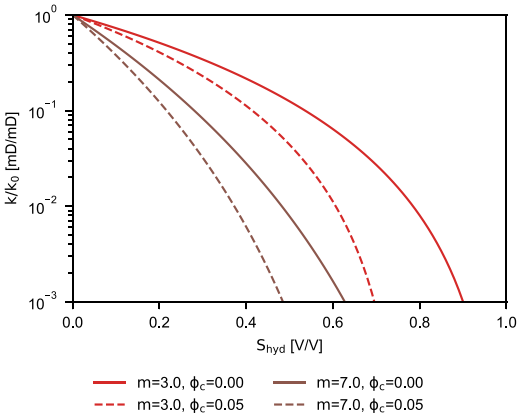

Fig. 5. Hydrate reduction of absolute permeability. Exponent m and critical porosity ϕ_c are fitting parameters. m determines the shape of the curve or the rate at which permeability is reduced. ϕ_c scales the curve on x-axis and sets the point at which permeability is reduced to zero.

(Eqs. (7) and (8)). Solid phases are no longer included as they are an extension of the matrix.

$$S_g^* = \frac{S_g}{(S_g + S_w)} = \frac{S_g}{(1 - S_h)} \tag{7}$$

$$S_w^* = \frac{S_w}{(S_g + S_w)} = \frac{S_w}{(1 - S_h)} \tag{8}$$

These new saturations yield a new relative permeability from Eqs. (3) and (2). To evaluate the effective phase permeability in hydrate bearing systems the relative permeability is 'scaled down' by the permeability reduction factor (Eqs. (9) and (10)).

$$k_w = k_0 \cdot k_{rF}(S_h) \cdot k_{rw}(S_w^*) \tag{9}$$

$$k_g = k_0 \cdot k_{rF}(S_h) \cdot k_{rg}(S_g^*) \tag{10}$$

Capillary pressure was defined by the van Genuchten model (van Genuchten, 1980), with capillary pressure (P_{cap}) as a function of water saturation (S_w), with no hysteresis considered (Fig. 5, Eq. (11)). The remaining terms are fitting parameters set by the user. The only condition is that the magnitude of residual water saturation (S_{irw}) should be smaller than the corresponding parameter in Eqs. (2) and (3). The magnitude of each of these parameters was defined to fit experimental values for capillary entry pressure run on Bentheim sandstone (Raeesi et al., 2014).

$$P_{cap} = -P_0 \left[(S^*)^{1/\lambda} - 1 \right]^{1-\lambda} \qquad \text{where } S^* = \frac{S_w - S_{irw}}{S_{mxw} - S_{irw}} \tag{11}$$

As hydrates grow, capillary pressure is scaled with the Leverett model, defined in Eq. (12). Both the hydrate-bearing and hydrate-free porosity and permeability from Eqs. (4) and (5) are used as input. As hydrates are an extension of the matrix, the resulting scaled capillary pressure will reflect a reduction on the effective radii of the pore throats (Fig. 6).

$$P_{cap}^* = P_{cap} \sqrt{\frac{k_0}{k} \cdot \frac{\phi}{\phi_0}} \tag{12}$$

2.1. Model setup

Several numerical simulations in T+H were set to simulate each experiment (Fig. 7). Gridding focused on representing the sandstone

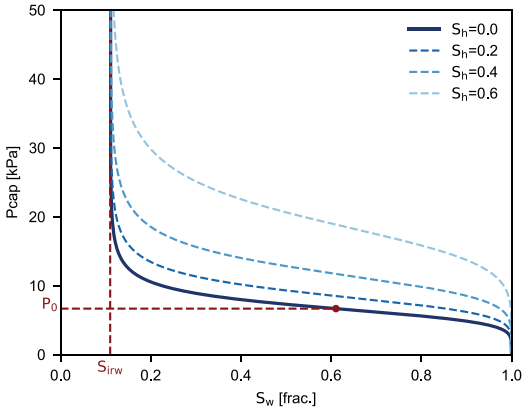

Fig. 6. In dark blue, capillary pressure curve based on van Genuchten model. Parameters P_0 and S_{irw} are highlighted in dark red. In lighter shades of blue, the scaled capillary pressure curves using Leverett model for different hydrate saturation values. (For interpretation of the references to colour in this figure legend, the reader is referred to the web version of this article.)

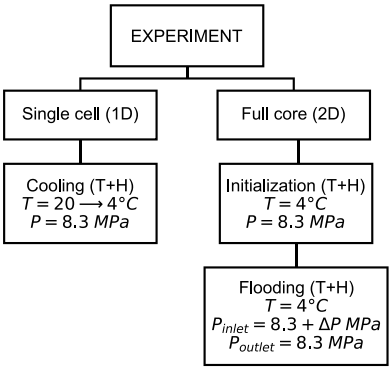

Fig. 7. Overview of simulations set in T+H for each experiment.

core and its interaction with its surroundings with regards to both mass and heat fluxes (Fig. 8).

2.1.1. Single cell simulation

The first set of simulation cases was done on a 1-dimensional representation of the system. This was a material balance exercise to estimate the total saturation of phases and concentration of salinity that an initial mix of brine and methane can yield after cooling down the system. The grid consists of a single element connected to two adjacent boundaries. The cell is initialized with the pre-hydrate fluid saturation values 1 at 20 °C and 8.3 MPa. The adjacent cells are thermodynamic boundaries, set to deliver the heat and mass fluxes necessary to keep the pressure constant and cooling the system down to 4 °C. These simulations were run using the equilibrium model. For comparative purposes, these simulations were reproduced using the kinetic model.

2.1.2. Full core model setup

The horizontal 2-dimensional cartesian grid representation displayed in Fig. 1 was used to simulate core flooding experiments after hydrate formation. Length and width of the full grid are close to the length (14.8 cm) and diameter (5.2 cm) of the core. In comparison to a 3-dimensional model, by reducing the problem by one dimension, the computational cost is minimized without compromising the quality of the results (Birkedal et al., 2014).

Surrounding the grid, boundary conditions were set to emulate the physical elements surrounding core in the experimental setup. To emulate the cooling system, the outer edge of the grid was set to steer and maintain the temperature constant. Permeability and porosity were set to zero, so no mass exchange occurs with the rest of the system.

In between the edge of the grid and the grid representation of the core, grid elements were set to represent the physical elements separating the core from the cooling source such as the steel pieces, the rubber sleeve and the confining fluid. Similarly, permeability and porosity are set to zero to avoid any mass exchange. The main purpose of these grid elements is to steer heat fluxes to emulate the cooling process of the core.

The edges along the y-axis are to represent the flow lines that inject and produce gas. This boundary is also initially set a thermodynamic boundary that actively steer the mass fluxes to sustain pressure.

The main grid is set to represent a Bentheimer sandstone core like the one used in the experiments. Different input parameters are set to describe the physical properties of the medium (Table 2). Similarly, parameters to define relative permeability relationship (Eqs. (3) and (2)) and effect of hydrates in porous media are included (Eq. (5)).

2.1.3. Full core model simulations

The full core grid was used to set up simulations of the core flooding experiments after hydrate formation. For pre-cooling conditions, porous media contain only two fluid phases, methane and brine, and simulation was not needed. Effective permeability was calculated by using the initial saturations of each experiment (Table 1) and Eq. (3).

Initialization at post-cooling conditions. For each experiment, a set of simulations were initialized using the final saturations of gas, brine and hydrate achieved experimentally (Table 1). These simulations were run using the kinetic model.

For initialization of these simulations, distribution of phases was set both homogeneously and heterogeneously. A homogeneous distribution was defined in a way that every single cell of the grid would initialize with the same values of saturation for all three phases. Heterogeneous distributions were set by using a random distribution of values for hydrate saturation. The values of each distribution are truncated between 0 and 1 and their average match the value measured. Multiple variations of standard deviation were set to cover a range of saturation from a narrow (±2 vol.%) to a broad (±50 vol.%) distribution. Fig. 10 shows the resulting distribution of phases for case B, when hydrate saturation has a variance of 36%.

The remaining fluid phases were defined so the bulk saturations of the entire grid would match the experimental values. Capillary effect was considered by setting up simulations with and without capillary pressure scaling. In the simulations without scaling capillary pressure, the fluid phase saturations are set keeping the proportions of the bulk measurements. When capillary pressure scaling is enabled, the distribution of the aqueous phase must be set so the system is in equilibrium in terms of pressure. Eqs. (11) and (12) yield a different capillary pressure (P_{cap}) curve for every value of hydrate saturation. Therefore, for each experiment and grid cell a value of capillary pressure has been determined by solving Eq. (11) for brine saturation (S_w) and that keeps the bulk volumes of all phases equal to the experimental measurements. This yields an accommodation of phases were the remaining pore space in grid cells with a high amount of hydrates is filled mainly by brine and gas fill the cells as hydrate saturation decreases (Figs. 9 and 10).

Flooding. Core flooding simulations were set for both pre- and post-cooling conditions. Pressure at the inlet boundary was set higher than the outlet boundary to induce gas flooding. This pressure difference was set small enough to guarantee that only gas flows in and out of the system and minimal mobilization of brine and phase changes would occur. Effective gas permeability ($k_{g,eff}$) was calculated by Darcy's law

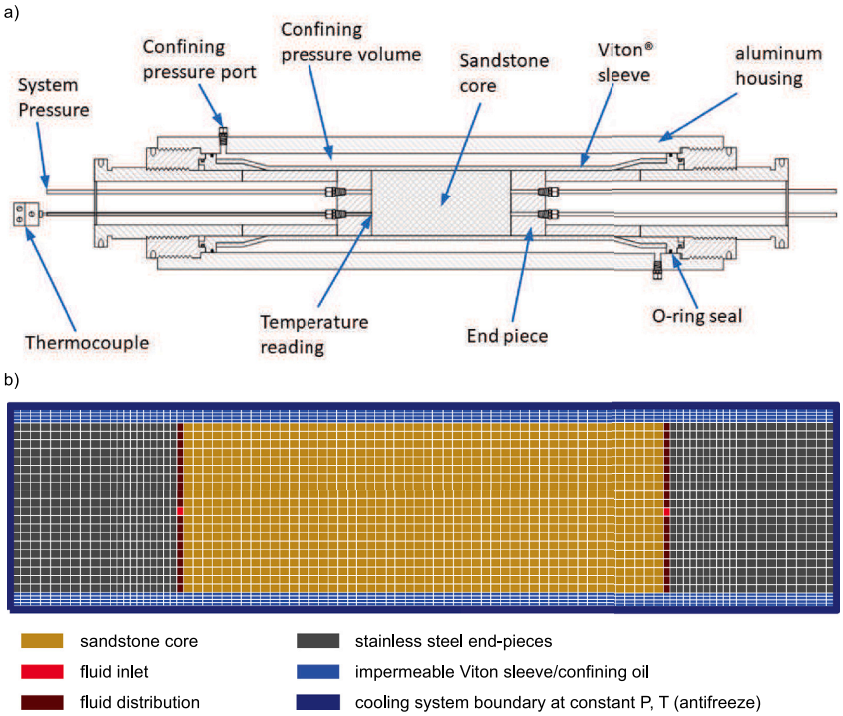

Fig. 8. (a) Cross-sectional view of the composite core holder. Modified from Husebø (2008). (b) Illustration of the numerical system based on the figure above. A no-flow (Neuman) boundary surrounds the system.

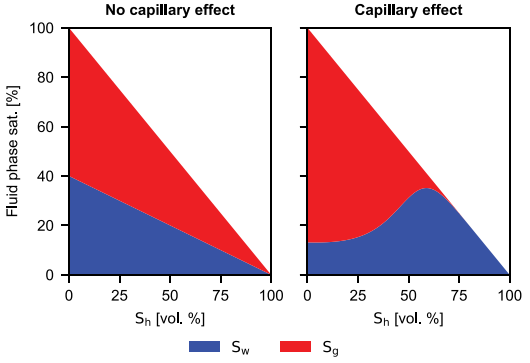

Fig. 9. Schematic representation of how fluid phase saturations are initialized in this study. When no hydrates effect on capillary pressure is considered, fluid phases are defined with the same proportion (left). When hydrates have an effect on capillary pressure (capillary pressure scaling), fluid phases are constrained by the capillary pressure function defined (right). Gas can only invade the larger pores and as hydrate saturation increases, the remaining pore space will be predominantly filled by brine.

defined in Eq. (13). μ_g is viscosity, Δx is the length of the grid in the horizontal axis, Q_g is the volumetric flow across the vertical cross section of the grid, and ΔP is the pressure difference between inlet and outlet of the grid.

$$k_{g,eff} = \mu_g \cdot \cdot \frac{\Delta x \cdot Q_g}{\Delta P} \tag{13}$$

3. Results and discussion

3.1. Hydrate formation:1-dimensional model

Simulations using the 1-dimensional model are displayed in Table 3. Hydrate formation yields an increase of salinity from 3.5 to 14 wt% NaCl, which matches the inhibition level of methane hydrate with NaCl at 8.3 MPa and 4 °C, confirming that the system has reached equilibrium. Fig. 11 shows the comparison between these simulations and the laboratory experiments.

In general, all simulations yielded equal or more hydrates than the experiments. All phase saturations showed variations in comparison to the experimental results. Largest variations are observed in final brine and hydrate saturation. Experiment A was initialized with the highest gas saturation (54 vol. %). Its simulation matched experimental results within the range of uncertainty.

Experiments B, C, D and E were initialized with a gas saturation between 46 and 47 vol. %. However, they all yielded different amounts of hydrates (45–51 vol. %) reflecting a limitation on the repeatability of results. Numerically, these simulations yielded more hydrates than any of the experiments (53 vol.%).

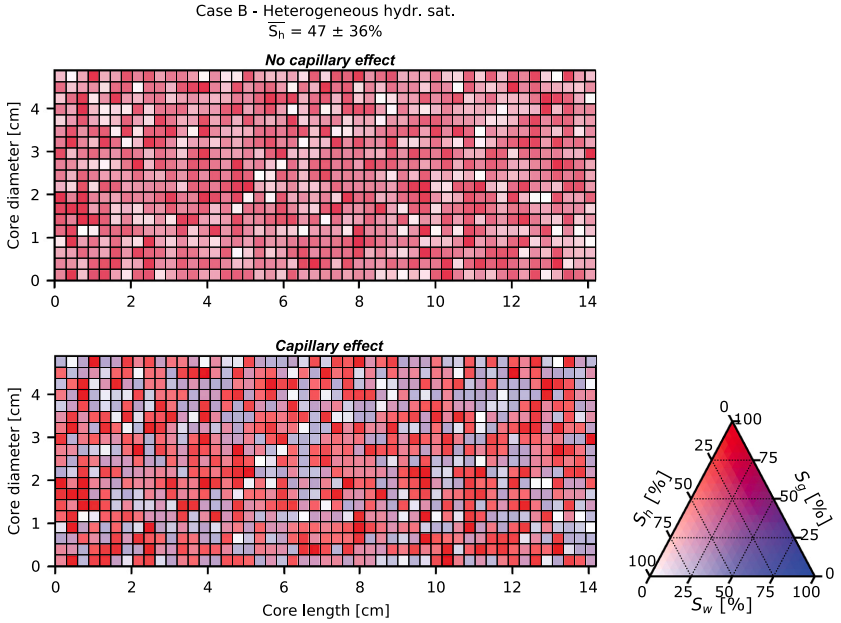

Fig. 10. Heterogeneous distribution of phases set for case B. The bulk phase saturations are equal to those obtained experimentally ($S_h = 47\%$, $S_g = 36\%$, $S_w = 17\%$). At a grid cell level, the magnitude for hydrate saturation is set randomly using a normal distribution defined by the measured hydrate saturation as its mean (47%), and a variance of ±36%. When no hydrate present does not affect capillary pressure (top figure), the non-hydrate filled pore space is set proportionally to the measurements of gas an brine saturation ($S_g = 36\%$, $S_w = 17\%$). To account for the effect of hydrates on capillary pressure (bottom figure), fluid phases are redistributed to achieve equilibrium.

Table 3
Comparison between saturation and salinity before and after cooling from single cell (1-dimensional) simulation for each experiment. S_w, S_g and S_h are volume fraction saturations for brine, gas and hydrate respectively. X_{inh} is salinity concentration.

Exp. ID	Input (T=20 °C)			Output (T=4 °C)			
	S_w	S_g	X_{inh}	S_w	S_g	S_h	X_{inh}
A	4.60E−01	5.40E−01	3.50E−02	9.88E−02	4.47E−01	4.54E−01	1.40E−01
B	5.30E−01	4.70E−01	3.50E−02	1.14E−01	3.63E−01	5.23E−01	1.40E−01
C	5.40E−01	4.60E−01	3.50E−02	1.16E−01	3.51E−01	5.33E−01	1.40E−01
D	5.40E−01	4.60E−01	3.50E−02	1.16E−01	3.51E−01	5.33E−01	1.40E−01
E	5.40E−01	4.60E−01	3.50E−02	1.16E−01	3.51E−01	5.33E−01	1.40E−01
F	6.40E−01	3.60E−01	3.50E−02	1.37E−01	2.31E−01	6.32E−01	1.40E−01
G	6.40E−01	3.60E−01	3.50E−02	1.37E−01	2.31E−01	6.32E−01	1.40E−01
H	7.30E−01	2.70E−01	3.50E−02	1.57E−01	1.23E−01	7.20E−01	1.40E−01

This pattern was repeated in experiments F and G. Both experiments were initialized with less gas than previous experiments (36 vol.%). The amount of hydrates formed was not reproduced experimentally either (53–61 vol.%), and such amount was less than the one formed numerically (63 vol.%).

Finally, experiment H was initialized with the lowest gas saturation (27 vol.%). The discrepancies between simulations and experiments were higher in this case. Simulation of this experiment yielded almost twice the hydrates formed experimentally and a third of the brine. Simulated final gas saturation was also a fraction of the experimental measurement.

In experiments B to H, as more hydrates are formed, the final brine saturation decreased correspondingly. Gas saturation remained similar in all experiments but experiment H, where final gas saturation is close to two thirds of the value obtained in the lab.

Whereas the experiments are constrained by both equilibrium and kinetics, the single cell simulations are in equilibrium and are only constrained by pressure, temperature and initial fluid in place. They return a material balance with no regard of the porous medium properties, where both cooling and hydrate formation occur homogeneously. These results can be regarded as the potential maximum amount of hydrates a given distribution of gas and brine can yield. The discrepancy between these and the experimental measurements suggests that experiments are not being able to form as much hydrates as they could potentially form.

Experimentally, gas must move throughout the core, limited by the intrinsic permeability of the porous medium and its initial saturation. As hydrates start forming, these are not formed homogeneously. At the pore scale, nucleation of hydrate will occur if both gas and brine are present. However, as hydrates form these will consume both phases and will need supply of either to form more hydrates. The rate at which more gas arrives will be limited by the reduced gas saturation. If all gas is consumed in a region of the core, such region is left with only hydrate and brine. In order to have more gas invading this sector, this stream of gas has to overcome the capillary entry pressure. In addition, the random nature of hydrate nucleation most likely creates stochastic flow barriers that progressively limit the flow. So, a low amount of hydrates returned by experiments, could be caused by gas not being

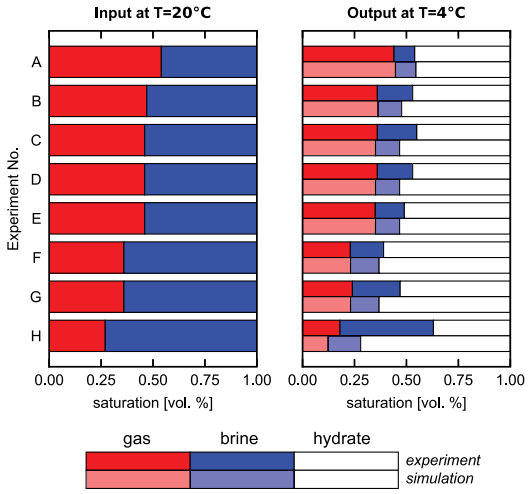

Fig. 11. Overview of phase saturations measured before and after cooling down. In a lighter shade of colour, modelled saturations from single cell simulations are added for comparison. (For interpretation of the references to colour in this figure legend, the reader is referred to the web version of this article.)

able to reach inner parts of the core due to hydrates limiting flow. They can also be caused by portions of the core saturated with either gas or brine with few contact points.

This is reflected in the fact that simulations yielded more hydrates in all cases but experiment A. Experiment A has the highest initial saturation of gas (S_{g0}) which means the initial effective permeability of gas (k_{g0}) is higher than any other experiment, allowing more gas to flow in the core as hydrates form. In contrast, experiment H has the lowest S_{g0} and its simulation returned the largest discrepancy in hydrate saturation (S_h). This means, although there is an excess of brine, it can only form hydrates with the gas that is in contact with brine. By the time hydrates start growing, gas supply is limited to reach remaining brine.

3.2. Hydrate effects on gas permeability

For the full core model simulations, methane relative permeability estimations were produced for cases with both a homogeneous and a heterogeneous distribution of fluid and solid phases. Simulations using a homogeneous distribution of phases, always returned a relative permeability higher than experiments (Table 4). Setting exponent m in Eq. (5) as 3, experiment A produced a value about 6 times higher than the measured value. This difference becomes higher in the remaining experiments, modelled values may be four orders of magnitude higher than the experimental values.

When m of Eq. (5) is increased to 5.4, methane permeability decreases but the modelled results are still higher than experimental ones (Table 4). Modelled methane relative permeability for experiment A has a magnitude close to the measured value. However, remaining experiments show a variation of modelled values up to 3 orders of magnitude higher than the measured ones.

As control points, relative permeability was also estimated by using the input phase saturations and the models defining equations (Eqs. (5) and (10)). The small change discrepancy between both values (Table 4 columns *from EQ* and *simulated*) respond to small changes in hydrate saturation during flooding, but still not high enough to change the bulk saturation of the grid.

These simulations show that the permeability reduction model (Eq. (5)) is not able to provide a unique solution that matches the experimental results. This suggests that reductions in gas relative permeability k_{rg} may not be caused exclusively by the permeability reduction factor K_{rF}.

By being a function of hydrate saturation (S_h), this model (Eq. (5)) does not account for changes in pore geometry caused by hydrate formation. Though the model is flexible to set the decrease of permeability to fit different pore habits (Dai and Seol, 2014), it does not consider the occurrence of multiple pore habits in a single lithology or the shifting between different habits with the change of hydrate saturation (Teng and Zhang, 2020). Dai and Seol (2014) have pointed out that in these types of models, the determination of fitting parameters like N or m lack a sound physical foundation and cannot be estimated based on lithology or other remotely detectable reservoir parameters.

These observations and the unlikelihood of having a homogeneous distribution of both fluid and hydrate justify testing a stochastic distribution of hydrates, closer to the "patchy" pattern that has been observed in hydrate-bearing sediments (Fig. 1).

A heterogeneous distribution of solid phases causes a reduction of the effective gas permeability. When the hydrate effect on capillary pressure is not considered (Fig. 12 left), permeability gets progressively smaller as the distribution of hydrates is more heterogeneous. With the broadest distribution permeability decreased by near one order of magnitude in all experiments. However, in this scenario, fluid phase saturations are proportional to the bulk saturations of the core (Fig. 9 left).

When the hydrate effect on capillary pressure is considered (12 right), the change from homogeneous to heterogeneous is more pronounced than in the previous simulations. This decline ranged from 1 order of magnitude lower in experiment A to almost 3 orders of magnitude in experiment H. The main reason for such decrease is that the capillary entry pressure in each cell has been scaled up by the hydrate saturation (Eq. (12)). Higher capillary pressure results in gas being accommodated preferentially to the cells with lower hydrate saturation. On the other end, cells with higher hydrate saturation will have the remaining pore space filled mainly by brine (Fig. 12 left). Injected gas is then able to move through those cells with low hydrate saturation. In contrast, its flow will be limited in the remaining cells by both hydrate and the low saturation of gas.

The set of simulations that considers the effect of hydrates on both capillary pressure and permeability yields results closer to those obtained experimentally (see Fig. 12). However, there is still a gap between modelled and measured values of methane relative permeability. Modelled results for experiment A yielded a close match for the two broadest distributions ($\sigma = \pm 36$ vol.%, ± 50 vol.%). To a lesser degree, a similar situation was observed in experiment B. However, remaining simulations returned values between one and two orders of magnitude higher than laboratory measurements (see Fig. 13).

The results suggest that the impact of a random pattern of hydrate growth on effective fluid flow cause reductions of relative permeability close to those observed in the laboratory. The same mechanism may also explain the limitations that can constrain the flow of gas and limit the amount of hydrates formed during cooling.

However, there are still gaps to achieve a better match between simulations and experiments. Such gaps are not necessarily explained only by the uncertainty of the input to the models, but can be caused by processes, that are not represented by the model.

Variations on experiments results that were initialized with similar phase saturations (B, C, D, E and F, G) suggest that the resulting distribution of hydrates may not be only heterogeneous but may follow a preferential pattern constrained by the rate at which the system was cooled down internally. A scenario where initial nucleation is located towards the outer rim of the core is possible. In this situation the edges of the core will meet the conditions to form hydrate first, and therefore limit the flow of gas towards the inner part of the core. This yields a

Table 4
Comparison between methane measured and modelled methane relative permeability Modelled values include preliminary calculations using Eq. (10) and simulated obtained from Darcy's law using simulated volumetric flow and differential pressure. These values include output for two different exponents m for Eq. (5).

Exp. ID	S_h	S_g	k_{rg} [frac.]				
	[frac.]	[frac.]	Measured	Modelled			
	±0.02	±0.02		m =3.0, ϕ_c =0.05		m =5.44, ϕ_c =0.05	
				From EQ.	Simulated	From EQ.	Simulated
A	0.46	0.44	1.9E−2 ± 0.3E−2	1.11E−01	1.17E−01	2.20E−02	2.28E−02
B	0.47	0.36	1.2E−3 ± 0.4E−3	5.72E−02	6.00E−02	1.08E−02	1.13E−02
C	0.45	0.36	1.7E−6 ± 0.6E−6	5.72E−02	5.60E−02	1.19E−02	1.17E−02
D	0.47	0.36	4.0E−6 ± 1.0E−6	5.72E−02	5.61E−02	1.08E−02	1.06E−02
E	0.51	0.35	1.4E−4 ± 0.5E−4	5.20E−02	5.12E−02	7.95E−03	7.75E−03
F	0.61	0.23	4.0E−7 ± 1.0E−7	1.27E−02	1.33E−02	1.04E−03	1.08E−03
G	0.53	0.24	9.9E−7 ± 0.8E−7	1.49E−02	1.54E−02	2.03E−03	2.11E−03
H	0.37	0.18	7.1E−7 ± 0.8E−7	5.51E−03	5.60E−03	1.65E−03	1.70E−03

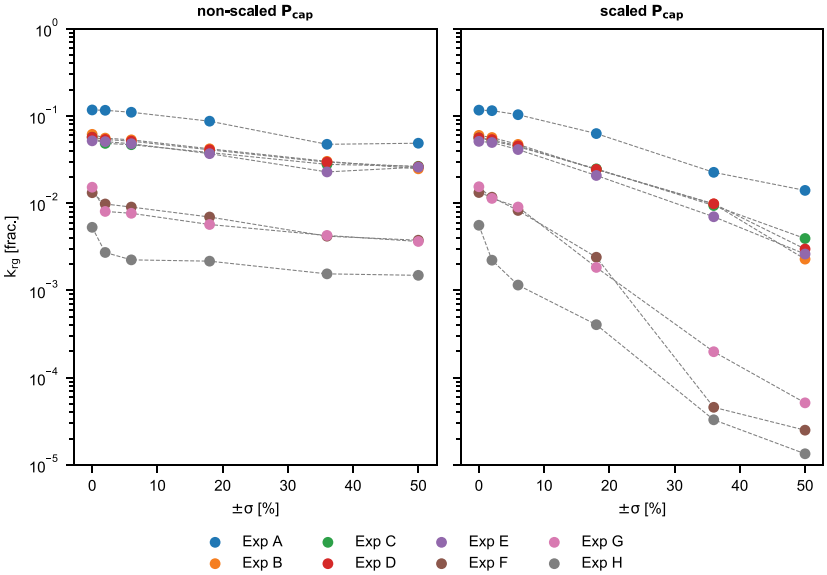

Fig. 12. Simulated methane relative permeability versus std deviation of hydrate distribution for simulations considering only hydrate effects on permeability (left) and for simulations considering hydrate effects on both permeability and capillary pressure. For each experiment, the average phase saturation remains constant, but its standard deviation changes from 0 to 50%.

limited amount of gas to form hydrates towards the middle of the core, and an effective reduction of permeability along the long axis of the core.

The saturation heterogeneities formed during hydrate growth are probably caused by local consumption of gas and water, as well as local reduction of porosity. These processes will cause driving forces to change rapidly. However, the effects may disappear or be enhanced over the natural timescales. For instance, unless replenished by gas, hydrates will eventually dissolve and disappear. One may also imagine processes as Ostwald ripening driving changes in the heterogeneities, perhaps enhancing the appearance of veins and patches.

These observations reflect the challenges of measuring relative gas permeability in hydrate bearing sediments. Though it is possible to perform a core flooding procedure with success, the resulting flow of gas will be constrained by the internal distribution of hydrates inside the core. In addition, the development of capillary barriers will decrease the flow of gas. Finally, if hydrates are being formed preferentially in the outer parts of the core, a low saturation of hydrates concentrated in this part can be enough to further the reduction of effective fluid flow.

4. Conclusions

- Experimental characterization and subsequent model implementation of the heterogeneities is necessary in order to model hydrate permeabilities. The impact that the heterogeneous nature of hydrate formation on sediment has on flow is seen in this study.
- Consistency testing by initial 1D modelling is valuable for comparing experimental and calculated bulk saturations. Discrepancies may indicate hydrate driven flow barriers.
- Adding heterogeneities to the hydrate saturation as seen in MRI experiments, are necessary in order to simulate the experimental trend of the permeabilities.
- Application of a capillary entry pressure is necessary to model regions where all the gas been consumed.

CRediT authorship contribution statement

Alejandro Bello-Palacios: Conceptualization, Methodology, Software, Formal analysis, Writing – original draft. **Per Fotland:** Supervision, Writing – review & editing. **Stian Almenningen:** Resources,

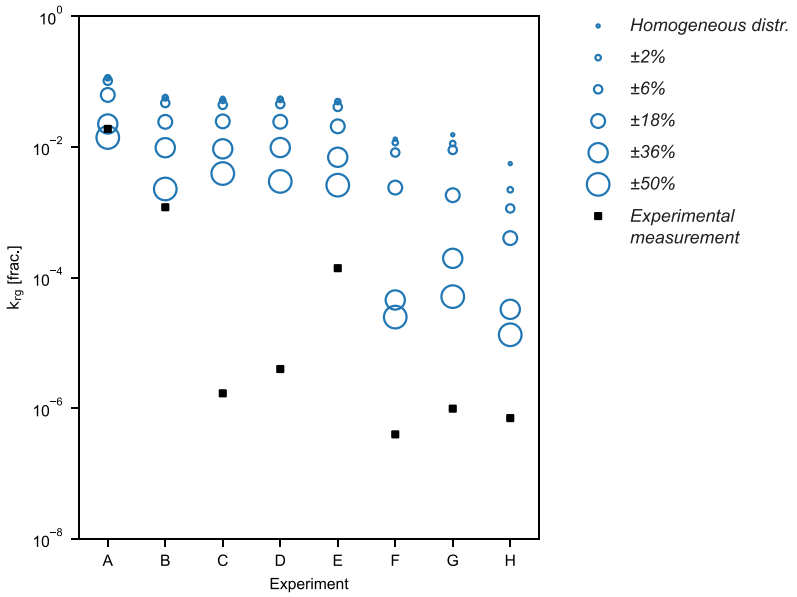

Fig. 13. Comparison between measurements of methane relative permeability (black squares) and simulated estimations (blue circles). The radius of the circles represents the standard deviation of the phase saturations within the grid. Smallest circles correspond to homogeneous distribution and the largest circle to a distribution with a broad variation ($\sigma = \pm 50\%$).

Writing – review & editing. **Geir Ersland:** Supervision, Writing – review & editing.

Declaration of competing interest

The authors declare that they have no known competing financial interests or personal relationships that could have appeared to influence the work reported in this paper.

Acknowledgements

This work was supported by funding from the Norwegian Research Council. Equinor ASA is thanked for permission to publish this work.

References

Ahn, T., Lee, J., Huh, D.G., Kang, J.M., 2005. Experimental study on two-phase flow in artificial hydrate-bearing sediments. Geosyst. Eng. 8, 101–104. http://dx.doi.org/10.1080/12269328.2005.10541244.

Almenningen, S., Gauteplass, J., Hauge, L.P., Barth, T., Fernø, M.A., Ersland, G., 2019. Measurements of ch_4 and co_2 relative permeability in hydrate-bearing sandstone. J. Pet. Sci. Eng. 177, 880–888. http://dx.doi.org/10.1016/j.petrol.2019.02.091.

Birkedal, K.A., Freeman, C.M., Moridis, G.J., Graue, A., 2014. Numerical predictions of experimentally observed methane hydrate dissociation and reformation in sandstone. Energy Fuels 28, 5573–5586. http://dx.doi.org/10.1021/ef500255y.

Boswell, R., 2009. Engineering. is gas hydrate energy within reach? Science 325, 957–958. http://dx.doi.org/10.1126/science.1175074, URL: https://www.ncbi.nlm.nih.gov/pubmed/19696340.

Chen, X., Verma, R., Espinoza, D.N., Prodanović, M., 2018. Pore-scale determination of gas relative permeability in hydrate-bearing sediments using x-ray computed micro-tomography and lattice boltzmann method. Water Resour. Res. 54, 600–608. http://dx.doi.org/10.1002/2017wr021851.

Collett, T., Bahk, J.J., Baker, R., Boswell, R., Divins, D., Frye, M., Goldberg, D., Husebø, J., Koh, C., Malone, M., Morell, M., Myers, G., Shipp, C., Torres, M., 2014. Methane hydrates in nature—current knowledge and challenges. J. Chem. Eng. Data 60, 319–329. http://dx.doi.org/10.1021/je500604h.

Dai, S., Seol, Y., 2014. Water permeability in hydrate-bearing sediments: A pore-scale study. Geophys. Res. Lett. 41, 4176–4184. http://dx.doi.org/10.1002/2014GL060535, URL: https://agupubs.onlinelibrary.wiley.com/doi/abs/10.1002/2014GL060535. arXiv:https://agupubs.onlinelibrary.wiley.com/doi/pdf/10.1002/2014GL060535.

Husebø, J., 2008. Monitoring Depressurization and CO_2-CH_4 Exchange Production Scenarios for Natural Gas Hydrates (Ph.D. thesis). University of Bergen.

Jaiswal, N.J., 2004. Measurement of Gas-Water Relative Permeabilities in Hydrate Systems (Ph.D. thesis). University of Alaska Fairbanks.

Jang, J., Santamarina, J.C., 2014. Evolution of gas saturation and relative permeability during gas production from hydrate-bearing sediments: Gas invasion vs. gas nucleation. J. Geophys. Res.: Solid Earth 119, 116–126. http://dx.doi.org/10.1002/2013jb010480.

Jang, J., Santamarina, J.C., 2016. Hydrate bearing clayey sediments: Formation and gas production concepts. Mar. Pet. Geol. 77, 235–246. http://dx.doi.org/10.1016/j.marpetgeo.2016.06.013.

Johnson, A., Patil, S., Dandekar, A., 2011. Experimental investigation of gas-water relative permeability for gas-hydrate-bearing sediments from the mount elbert gas hydrate stratigraphic test well, alaska north slope. Mar. Pet. Geol. 28, 419–426. http://dx.doi.org/10.1016/j.marpetgeo.2009.10.013.

Kim, H.C., Bishnoi, P.R., Heidemann, R.A., Rizvi, S.S.H., 1987. Kinetics of methane hydrate decomposition. Chem. Eng. Sci. 42, 1645–1653. http://dx.doi.org/10.1016/0009-2509(87)80169-0.

Kleinberg, R.L., Flaum, C., Griffin, D.D., Brewer, P.G., Malby, G.E., Peltzer, E.T., Yesinowski, J.P., 2003. Deep sea nmr: Methane hydrate growth habit in porous media and its relationship to hydraulic permeability, deposit accumulation, and submarine slope stability. J. Geophys. Res.: Solid Earth 108, http://dx.doi.org/10.1029/2003jb002389.

Kowalsky, M.B., Moridis, G.J., 2007. Comparison of kinetic and equilibrium reaction models in simulating gas hydrate behavior in porous media. Energy Convers. Manage. 48, 1850–1863. http://dx.doi.org/10.1016/j.enconman.2007.01.017.

Li, G., Li, C., Li, X., Wei, N., 2018. Permeability experiments on the methane hydrate in quartz sands and its model verification. Nat. Gas Ind. B 5, 298–305. http://dx.doi.org/10.1016/j.ngib.2017.12.009.

MASUDA, Y., 1997. Numerical calculation of gas production performance from reservoirs containing natural gas hydrates. In: Annual Technical Conference. Soc. of Petrol. Eng., San Antonio, Tex., URL: https://ci.nii.ac.jp/naid/10025408647/en/.

Moridis, G.J., Collett, T.S., Pooladi-Darvish, M., Hancock, S., Santamarina, C., Boswell, R., Kneafsey, T., Rutqvist, J., Kowalsky, M., Reagan, M.T., Sloan, E.D., Sum, A.K., Koh, C., 2010. Challenges, uncertainties and issues facing gas production from gas hydrate deposits. SPE Reserv. Eval. Eng. Medium: ED. URL: https://www.osti.gov/servlets/purl/1005168.

Moridis, G., Pruess, K., 2014. User's Manual of the Tough+ V1. 5 Core Code: A General Purpose Simulator of Non-Isothermal Flow and Transport Through Porous and Fractured Media. Report, Lawrence Berkeley National Laboratory, URL: http://tough.lbl.gov/assets/files/02/documentation/TH_Manual_v1.5s.pdf.

Raeesi, B., Morrow, N.R., Mason, G., 2014. Capillary pressure hysteresis behavior of three sandstones measured with a multistep outflow-inflow apparatus. Vadose Zone J. 13, http://dx.doi.org/10.2136/vzj2013.06.0097.

Ren, X., Guo, Z., Ning, F., Ma, S., 2020. Permeability of hydrate-bearing sediments. Earth-Sci. Rev. 202, http://dx.doi.org/10.1016/j.earscirev.2020.103100.

Sloan, E., Dendy, J., Koh, C., 2007. Clathrate Hydrates of Natural Gases. CRC Press LLC, Bosa Roca, United States.

Teng, Y., Zhang, D., 2020. Comprehensive study and comparison of equilibrium and kinetic models in simulation of hydrate reaction in porous media. J. Comput. Phys. 404, 109094. http://dx.doi.org/10.1016/j.jcp.2019.109094, URL: https://www.sciencedirect.com/science/article/pii/S0021999119307995.

van Genuchten, M.T., 1980. A closed-form equation for predicting the hydraulic conductivity of unsaturated soils. Soil Sci. Am. J. 44, 892–898. http://dx.doi.org/10.2136/sssaj1980.03615995004400050002x.

Paper II

A.2 Experimental and Numerical Analysis of the Effects of Clay Content on CH_4 Hydrate Formation in Sand

Alejandro Bello-Palacios, Stian Almenningen, Per Fotland, and Geir Ersland

Energy & Fuels 35, **12**, 9836–9846 (2021)

energy&fuels

pubs.acs.org/EF

Article

Experimental and Numerical Analysis of the Effects of Clay Content on CH_4 Hydrate Formation in Sand

Alejandro Bello-Palacios,* Stian Almenningen, Per Fotland, and Geir Ersland

Cite This: *Energy Fuels* 2021, 35, 9836–9846

Read Online

ACCESS | Metrics & More | Article Recommendations

ABSTRACT: Natural gas hydrates exist in large quantities in nature and represent a potential source of energy, mostly in the form of methane gas. Knowledge about hydrate formation in clayey sand is of importance for understanding the production of methane gas from hydrate reservoirs, as well as for understanding the impact of global warming on the stability of subsurface gas hydrates. In this paper, we explore the effect of clay content on methane gas hydrate phase transitions in unconsolidated sand at realistic reservoir conditions (P = 83 bar and T = 5−8 °C) both experimentally and numerically. Kaolin clay was mixed in pure quartz sand in a series of experiments where the clay content ranged from 0 wt % to approximately 12 wt %. Simulations of these experiments were set up in TOUGH+HYDRATE. In the kinetic reaction model, particle size was used as a proxy for kaolin content. The growth of methane hydrates from water (0.1 wt % NaCl) and methane were visualized and quantified by magnetic resonance imaging with millimeter resolution. Dynamic imaging of the sand revealed faster hydrate growth in regions with increased clay content. NMR T_2 mapping was used to infer the hydrate phase transition characteristics at the pore scale. Numerical simulations showed also faster growth in materials with a smaller mean particle size. The simulation results showed a significant deviation throughout the hydrate growth period. The constraints of both the experimental and modeling setups are discussed to address the challenges of comparing them.

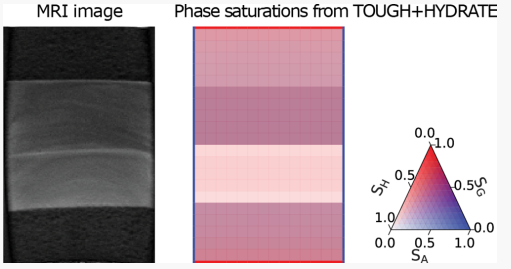

INTRODUCTION

Background. The amount of methane gas associated with natural gas hydrates in nature has led to a proliferation of research on gas hydrates in porous media. Several countries have state-sponsored research programs aimed at quantifying the domestic resource potential and enabling safe methane gas production from hydrate reservoirs. The trial productions that have been undertaken over the past two decades highlight the difficulty of maintaining sustained gas production by field-scale hydrate dissociation.[1−3] The preferred production method is to dissociate the hydrate structure into water and methane by pressure depletion and let the pressure differential between the dissociation front and the wellbore drive the production of fluids.[4] The hydrate accumulations most likely for gas production are located in the pore space of sandy sediments.[5] The presence of solid hydrates in the pore space enhances the effective cohesion of the sediments and has a stabilizing effect on the integrity of the formation.[6] The combined effect of pressure depletion and conversion of solid hydrates to fluids can trigger mobilization of sediments and collapse of the formation.[7,8] A review of all field pilots conducted to date shows that all tests have to some extent experienced problems with uncontrolled sand production.[9] The sandy sediments that are usually targeted as promising hydrate accumulations also contain varying amounts of clay particles that may be mobilized during hydrate dissociation. The transportation of small particles, i.e., fines, may alter the permeability of the formation by either enhancing it in the pores where the fines are displaced or decreasing it in the pores where the fines are deposited.[10] In either way, the impact of clay particles should be addressed in laboratory experiments to mimic the flow behavior of water and gas in unconsolidated sediments.

Clay Content in Hydrate Bearing Sediments. The impact of clay particles on hydrate phase stability is important when assessing the potential of finding large accumulations of hydrates in different lithologies. High hydrate accumulations are typically found in coarse-grained sand where the connectivity of the pore bodies is good, leading to an even distribution of methane throughout the pore space. Increased clay content is associated with narrower pores that limit the

Received: February 18, 2021
Revised: May 7, 2021
Published: May 31, 2021

https://doi.org/10.1021/acs.energyfuels.1c00549
Energy Fuels 2021, 35, 9836−9846

accumulation of hydrates but can locally cause volumes of high saturation, i.e., almost pure hydrate. These pure hydrate volumes are however not connected as in coarse-grained sand, but rather display a veined and patchy distribution. Waite et al.[11] explored the correlation between hydrate saturation and clay content in sandy sediments from the Krishna-Godavari Basin, the Cascadia Margin,[12] and the Nankai Trough.[13] The clay content was defined as the volume fraction of grains smaller than 4 μm. The hydrate saturation was close to zero in sediments with clay fractions larger than 0.3, while elevated hydrate saturations larger than 0.4 and 0.6 were found in sediments with clay fractions less than 0.1 and 0.05, respectively. The clay content thus seems to effectively control the saturation of hydrates found in nature. However, the effect on hydrate phase equilibria depends on the specific clay mineral. Kaolin clay with water content less than 20 vol % yielded methane hydrate equilibrium temperatures that were up to 1.5 °C lower than bulk hydrate.[14] A similar hydrate inhibition was observed for glass beads with a particle size slightly higher than that of kaolin clay. The inhibition effect of kaolin clay was thus explained as a pore size phenomenon. The equilibrium temperature was also depressed in bentonite clay, except when the water content was larger than approximately 90 vol %. Then, the equilibrium temperature was slightly elevated and hydrate formation was promoted. In another study, the presence of bentonite clay in a suspension of silica sand and seawater decreased the induction time of hydrate formation and enhanced the rate of gas consumption compared to silica sand alone.[15]

Numerical Simulation of Gas Hydrates in Porous Media. Hydrate reservoir simulators are essential to forecast the long-term production performance of hydrate-bearing reservoirs.[16] Multiple tools have been tested and compared[16,17] to validate and build confidence in the modeling of hydrate-related processes in porous media.

In general, these tools involve coupling of physical, chemical, and thermal processes.[16] Formation and dissociation of hydrates are commonly modeled as either an equilibrium phenomenon or a kinetic reaction.[18] In the first approach, two main components (water and gas) can be found present in different phases, depending on the conditions of pressure and temperature. In the second approach, hydrate is treated as a new mass component and phase transitions are calculated from the kinetic parameters of the model. Multiple models developed to represent kinetic hydrate formation have been proposed. Yin et al.[19] has mapped out a total of 27 well-known hydrate growth kinetic models. Just a few models have been developed and implemented in reservoir simulation codes to model hydrate growth in porous media.[20−23] All these models are defined by an Arrhenius-type reaction rate constant. Another factor that steers the gas consumption is the surface area, which can be defined by time-dependent[22] or hydrate-saturation-dependent[20,21,23] factors. In addition, a driving force is defined by the difference in the fugacity of methane between the gas phase and the three-phase equilibrium[20,21,23] or the difference in chemical potential between water in the hydrate and liquid phases.[22]

The TOUGH+HYDRATE v1.5 (T+H)[24] code and its open-source version HydrateResSim[25] are codes developed by Lawrence Berkeley National Laboratory. Both codes have been used in the numerical evaluation of natural occurrences of gas hydrates[26−29] and to model experiments on hydrate formation.[30,31] The code has been developed to simulate the behavior of methane hydrate bearing sediments and handles both multiphase, multicomponent flow and transport of mass and heat through porous and fractured media.[21]

In T+H hydrate formation and dissociation are modeled by using either a kinetic or equilibrium model. Kowalsky and Moridis[32] have concluded that the kinetic model is more suitable for modeling short-term and core-scale processes.

The kinetic model in T+H is defined by eq 1.[33]

$$\frac{\partial M}{\partial t} = K_0 e^{(-\Delta E_a/RT)} F_A A_S (f_{eq} - f_v) \quad (1)$$

where $\frac{\partial M}{\partial t}$ is the methane mass rate of change, K_0 is the intrinsic hydration reaction constant, ΔE_a is the hydration activation energy, R is the universal gas constant, T is the temperature, F_A is the area adjustment factor, A_S is the hydrate reactive surface area, f_{eq} is the fugacity at equilibrium temperature, and f_v is the fugacity in the gas phase at temperature T.

Equation 1 yields the uptake of gas for hydrate formation in time (Figure 1). Changes in the gas consumption rate follow

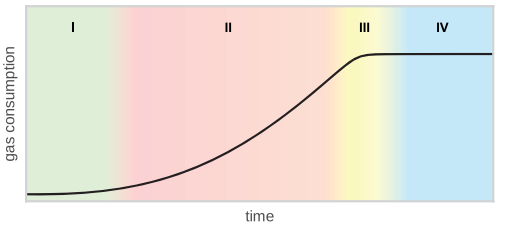

Figure 1. T+H modeled gas uptake curve during gas hydrate formation from the kinetic model. Colors highlight the different stages in hydrate formation described by Yin et al.[19] Induction time (stage I), rapid hydrate growth (stage II), decreased growth (stage III), and steady state (stage IV).

the typical gas uptake curve described by Yin et al.[19] in four stages. The early slow growth mimics an induction time (stage I), followed by a steep growth where most of the gas intake occurs (stage II) until it slows down (stage III) and reaches a steady state (stage IV).

There are no specific parameters in the model that respond to the presence of clay. However, the size of particles, the porosity of the sediment, and the hydrate saturation are the input parameters that define the reactive surface area (A_S), which has an impact on the hydrate growth and dissociation rates. The magnitude of A_S is a function of the average grain radius of the sediment r_p, its porosity ϕ, and the hydrate saturation S_H at a given time (eq 2[33]).

$$A_S = 0.879 \frac{1-\phi}{r_p} S_H^{2/3} \quad (2)$$

In this study, we examine the effect on methane hydrate phase transitions by adding kaolin clay to quartz sand. Specifically, we map the saturation of methane hydrates during formation at reservoir conditions by magnetic resonance imaging (MRI). The weight percent of kaolin clay compared to quartz sand was low (lower than 13 wt %) to emphasize the effect of the surface texture of kaolin clay on hydrate phase transitions.

T+H was used to reproduce numerically the experimental observations. To validate the kinetic reaction model, particle

https://doi.org/10.1021/acs.energyfuels.1c00549
Energy Fuels 2021, 35, 9836−9846

size is used as a proxy of clay content. We study how variations in particle size affect the modeled hydrate growth. Model outputs are compared with experimental measurements to identify the strengths and limitations of the code.

The results of this work are relevant for both experimental analysis and numerical analysis of hydrate accumulations in coarse-grained sand reservoirs containing clay.

METHODS

Experimental Setup. Quartz sand (D50 = 220 μm) mixed with kaolin clay (D50 = 3.5 μm) was used as host sediment for the methane hydrate phase transitions in this study. Dry kaolin clay was added to the sand and mixed thoroughly by rotating a beaker. The rubber sleeve was placed vertically with a fluid-distributing end piece inserted at the bottom. Different mixtures of sand and clay were then placed in sections inside the rubber sleeve on top of each other. Consolidated Bentheim sandstone core pieces were placed as filters at both ends between the body of sand and the end pieces to avoid sand production. The average pore diameter of Bentheim sandstone is 125 μm.[34] The core holder, high-pressure pumps, cooling system, and superconductive magnet used for MR imaging are detailed in Almenningen et al.[35]

Experimental Procedure. Two different experimental runs were conducted with two different designs. In the first experiment (experiment 1, Figure 2), the length of the rubber sleeve was filled with Bentheim sandstone (L = 2.42 cm), pure quartz sand (L = 2.30 cm), quartz sand containing 0.9 wt % kaolin clay (L = 2.80 cm), and Bentheim sandstone (L = 2.13 cm). In the second experiment (experiment 2, Figure 1), the length of the rubber sleeve was filled with Bentheim sandstone (L = 2.15 cm), quartz sand containing 3.4 wt % kaolin clay (L = 2.00 cm), quartz sand containing 6.1 wt % kaolin clay (L = 2.15 cm), quartz sand containing 12.4 wt % kaolin clay (L = 2.20 cm), and Bentheim sandstone (L = 2.12 cm). A core holder was mounted around the rubber sleeve, and an effective confining pressure of 15 bar was applied before the core holder was placed horizontally.

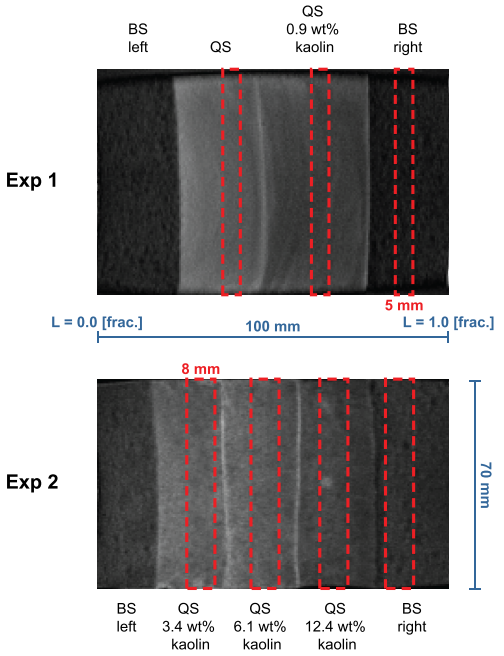

Figure 2. Sagittal view of quartz sand (QS) and Bentheim sandstone (BS) saturated with brine inside the core holder. The red dashed rectangles mark the positions of the axial MRI slices that were used to analyze hydrate formation (5 mm thick for experiment 1 and 8 mm thick for experiment 2).

The pore space was purged under vacuum and subsequently saturated with brine containing 0.1 wt % NaCl. Injection of methane gas from one side of the core material displaced some of the brine, and the pore space was consequently filled with a mixture of methane gas and brine. In experiment 1, to achieve a continuous phase of gas along the core setup, methane gas was injected until there was a gas breakthrough at the other end. In experiment 2, the gas inflow was stopped prior to gas reaching the other end, so the right section of the core setup would be 100% saturated with brine.

Hydrate formation was then triggered by cooling the system to 7 °C and increasing the pore pressure to 83 bar by methane gas injection from both sides of the core material. The 2-D saturation maps of brine and methane hydrates were continuously acquired during hydrate growth. Bulk hydrate saturation (S_h) was calculated from the amount of methane consumed by the system, using PVT data. Simultaneously, an explicit mapping of hydrate saturation (S_h) was obtained by tracking the changes in water saturation observed in the MRI images, assuming that all reduction in water saturation was caused by hydrate formation. This assumption is reasonable for hydrate growth at constant pressure.[35]

Modeling Setup. The physical system was represented in both a one-dimensional grid and a two-dimensional grid. The different contents of kaolin were interpreted as a variation of particle size.

The magnitude of the area adjustment factor (F_A) value was reduced iteratively until the time scales of both the experiments and simulations were of the same order of magnitude. F_A can be adjusted to match observations in history matching simulations.[21] Yin et al.[31] has determined that F_A may not remain constant during hydrate formation. In our study, the magnitude was kept constant through the whole simulation.

One-Dimensional Model. A one-dimensional grid was built to have bulk estimates of the growth of hydrates through time and final phase saturations. This model assumes both brine and gas are evenly distributed and in contact with each other. The system was initialized by having brine and gas at 7 °C. The pressure is calculated by T+H to near 53 bar, just next to the boundary of stability for the given salinity (0.3 wt % NaCl). As soon as hydrates start forming, the pressure and temperature are sustained by a thermodynamic boundary. This boundary is set to keep the pressure and temperature at 83 bar and 7 °C, by injecting gas and steering the flow of heat.

This model was used first to calculate the final hydrate saturation of experiments 1 and 2, based on their initial fluid phase saturations. Then, the model was used to study the effect of initial fluid saturation and particle size on hydrate growth driven by the kinetic reaction model of T+H. These simulations were set by initializing the model with a broad range of brine saturation (S_{wi}) and particle sizes (r_p), ranging from 50 to 110 μm.

Two-Dimensional Model. Two-dimensional grids were built representing both experiments (Figure 3). The grid represents a sagittal horizontal slice of the core, discretized by 280 cubic elements (20 × 14) of 50 mm on edge length. The grid is surrounded by infinite boundaries that steer both mass and heat flow. Along the longest axis, the boundary is impermeable and is set to deliver the necessary heat flow to keep the system at the target temperature. The boundaries along the shortest axis represent the core end pieces and behave like those in the 1-D model.

The grid was split into regions emulating the different core pieces for each core setup (Figure 3). No measurements of porosity, permeability, and other thermophysical properties were available for the sand mixtures used. Therefore, all intrinsic thermophysical properties other than the particle size were assumed equal for all regions (Table 1).

https://doi.org/10.1021/acs.energyfuels.1c00549
Energy Fuels 2021, 35, 9836−9846

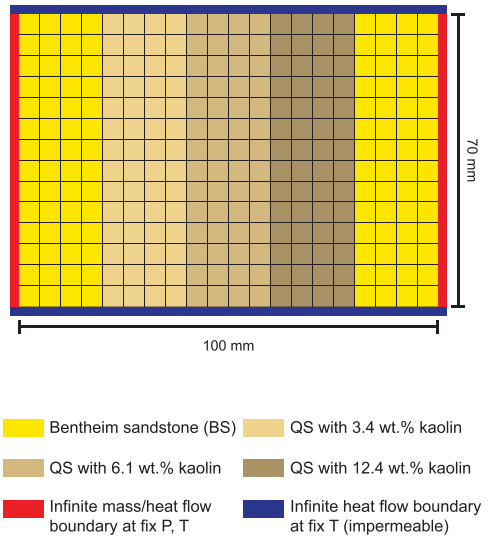

Figure 3. Two-dimensional simulation grid for experiment 2. The infinite boundary in red is set to deliver the necessary mass and heat flow to keep the system at the target pressure and temperature. The infinite boundary in dark blue is impermeable and is set to deliver the necessary heat flow to keep the system at the target temperature.

The particle size (r_p) was adjusted with the grain size of the clean quartz sand used in the experiments as reference (110 μm). The remaining sand mixtures were adjusted under the premise that sand with a larger amount of kaolin would have a smaller representative mean grain radius. The particle size of Bentheim sandstone was also adjusted to match results.

Unlike the 1-D models, simultaneous hydrate growth at different rates occurs in different locations of the model. To focus only on the effects of particle size and to keep the model numerically stable, the intrinsic permeability was set to remain unaffected by the presence of a solid hydrate phase. Other thermophysical properties were left unchanged for all grid cells, with their magnitudes based on Bentheim sandstone values used by Birkedal et al.[38] Simulations were run with the capillary pressure function both enabled and disabled. With the latter setup, the fluid flow would be driven only by pressure differences in the system (Darcy flow). The multiphase flow would be therefore governed solely by relative permeability curves (Table 1).

RESULTS

Experimental Results. Prior to hydrate formation, the initial average water saturation was 0.62 (fraction) with a near even distribution throughout the core (Figure 4). As hydrate started forming, the liquid water saturation decreased faster in the quartz sand containing 0.9 wt % kaolin compared to the rest of the sediments. This means that the initial hydrate growth was significantly faster in quartz sand containing 0.9 wt % kaolin than in Bentheim sandstone and pure quartz sand (Figure 10a). However, a residual liquid water saturation remained at approximately 0.06 fraction after hydrate formation ceased at an average hydrate saturation of 0.71 (fraction). After hydrate formation, the apparent gas permeability was zero, indicating complete blocking of the pore space.

The initial water distribution was heterogeneous in experiment 2 (Figure 5) with an increasing water saturation from 0.50 (fraction) at $L > 0.75$ (fraction) to 1.0 (fraction) at $L < 0.30$ (fraction). The average water saturation was 0.76

Table 1. Thermophysical Properties of Materials and Parameters Used in Simulation Model

parameter	value[a]
gas composition	100% CH_4
intrinsic hydration reaction constant (K_0)	4.70848×10^5 mol/(m^2·Pa·s)[37]
hydration activation energy (ΔE_a)	8.1×10^4 J/mol[37]
universal gas constant (R)	8.314 J/(mol·K)
intrinsic permeability ($k_x = k_y = k_z$)	1.5 D (1.48×10^{-12} m^2)
porosity (ϕ)	0.30 fraction
density (ρ)	2650 kg/m^3
thermal conductivity, dry (λ_d)	0.30 W/m/K
thermal conductivity, fully saturated (λ_w)	1.65 W/m/K
specific heat (c_p)	1400 J/kg/K
boundary thermal conductivity (λ_b)	0.20 W/m/K
boundary specific heat ($c_{p,b}$)	1000 J/kg/K
composite thermal conductivity model (λ)	$\lambda = \lambda_d + (S_W^{1/2} + S_H^{1/2})(\lambda_w - \lambda_d)$
modified relative permeability model[38]	$k_{rA} = \left(\frac{S_W - S_{irW}}{1 - S_{irW}}\right)^{n_W}$
	$k_{rG} = \left(\frac{S_G - S_{irG}}{1 - S_{irW}}\right)^{n_G}$
	$k_{rH} = 0$
	$n_W = n_G = 3.0$
	$S_{irW} = 0.12$, $S_{irG} = 0.02$
capillary pressure model[39]	$P_{cap} = -P_0[(S^*)^{-1/\lambda} - 1]^{1-\lambda}$
	$S^* = \frac{S_W - S_{irW}}{S_{mxA} - S_{irW}}$
	$\lambda = 0.6$, $S_{irW} = 0.11$
	$P_0 = 2 \times 10^3$, $S_{mxA} = 1.0$

[a]Subscripts "W", "G", and "H" represent aqueous, gas, and hydrate phases, respectively; S_X is the phase saturation; S_{irX} is the irreducible phase saturation.

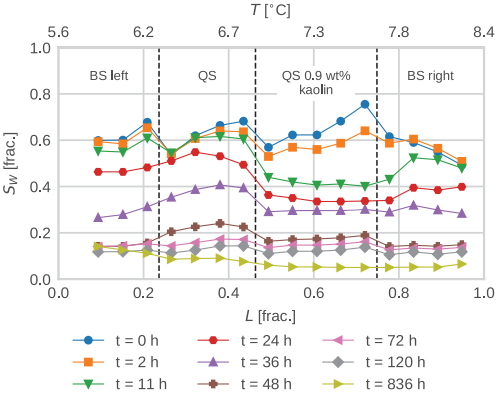

Figure 4. Change in water saturation during hydrate growth at constant pressure, $P = 83$ bar, in experiment 1.

https://doi.org/10.1021/acs.energyfuels.1c00549
Energy Fuels 2021, 35, 9836−9846

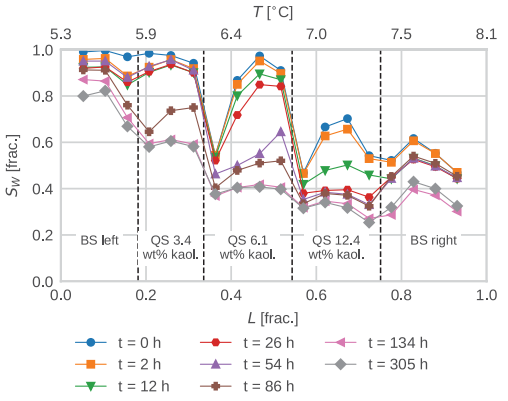

Figure 5. Change in water saturation during hydrate growth at constant pressure, P = 83 bar, in experiment 2.

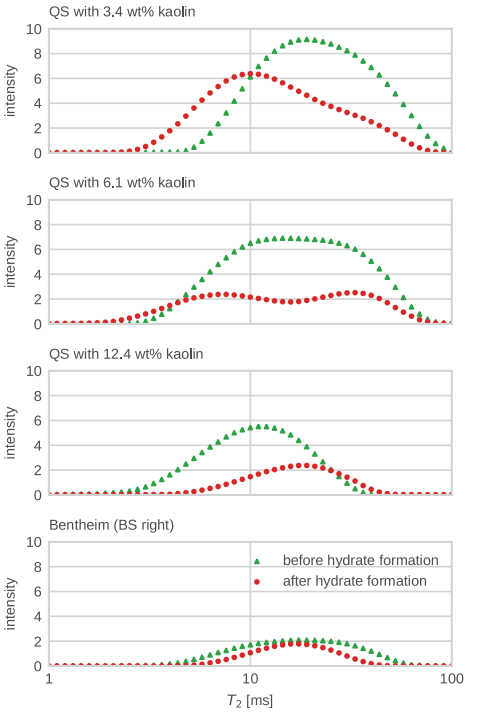

Figure 6. T_2 distributions before and after hydrate growth in experiment 2.

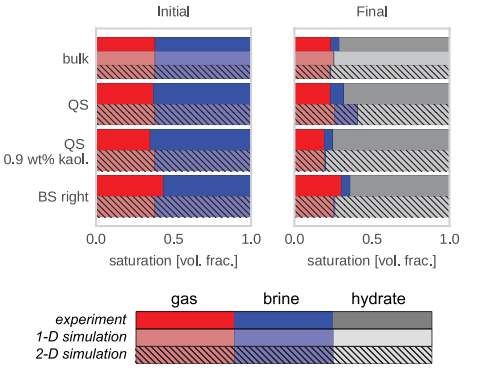

Figure 7. Experiment 1. Comparison of average phase saturations yielded by experiments and simulations for the entire core setup (bulk) and each core piece. Initial values prior to hydrate formation on left and final post hydrate formation values on right. Experimental measurements in bold colors, 1-D simulation results in lighter colors, and 2-D simulation results in dashed colors.

(fraction) prior to hydrate formation. As hydrate started forming, the liquid water saturation decreased faster in the quartz sand containing 12.4 wt % kaolin compared to other parts of the sediment. This means that the initial hydrate growth was faster in quartz sand containing the most kaolin during the first 26 h of hydrate formation (Figure 11a). Next, from t = 26 h to t = 54 h, a massive hydrate growth occurred in the quartz sand containing 6.1 wt % kaolin. The growth of hydrate was limited in the rest of the sediments during this period. Massive hydrate growth followed in the quartz sand containing 3.4 wt % kaolin from t = 54 h to t = 86 h. The growth of hydrate was thus sequential, moving from quartz sand with high kaolin content to quartz sand with low kaolin content. The final water and hydrate saturation after hydrate formation were 0.51 and 0.33 (fraction), respectively.

The transverse relaxation time constant T_2, which increases with pore size, showed a different response as the content of clay increased (Figure 6). In quartz sand with 3.4 wt % kaolin, the intermediate to large T_2 (pore size) components disappeared during hydrate growth. However, in quartz sand containing 12.4 wt % kaolin, it was the intermediate to low T_2 components that disappeared during hydrate growth.

Modeling Results. *One-Dimensional Model.* The first set of results from the 1-D simulations is shown in Figures 7 and 8. In the one-dimensional simulation for experiment 1, the final hydrate saturation after hydrate formation was 0.74 (fraction). The remaining volume is filled by mainly gas (0.25) and a small fraction of brine (less than 0.01). For experiment 2, the final hydrate saturation after hydrate formation was 0.91 (fraction). The remaining volume is filled by mainly gas (0.08) and a small fraction of brine (less than 0.01). Given the assumptions of the model, the system consumes all the water to form hydrates. The remaining water saturation is a result of inhibition due to increased salinity (8.7 wt % NaCl).

The second set of results from the 1-D simulations is shown in Figure 9. Each simulation produced a hydrate growth (gas uptake) curve in time, defined by the kinetic model and variations on the input parameters. Decrease of particle size resulted in a shorter induction time (stage I) and a higher rate during the main hydrate growth (stage II). Initial brine saturation (S_{wi}) has a direct impact on the magnitude of hydrate saturation at which hydrate growth slows down and reaches a steady state (stages III and IV).

Two-Dimensional Model. Results for 2-D simulations of experiments 1 and 2 are included in Figures 10b and 11b,

https://doi.org/10.1021/acs.energyfuels.1c00549
Energy Fuels 2021, 35, 9836−9846

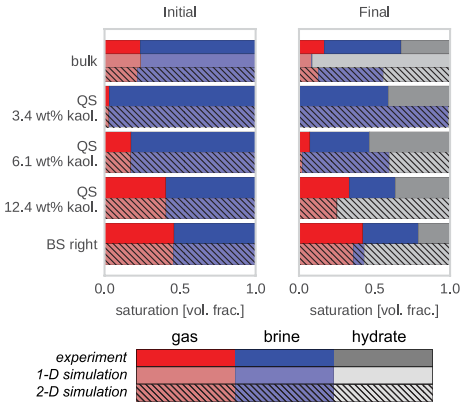

Figure 8. Experiment 2. Comparison of average phase saturations yielded by experiments and simulations for the entire core setup (bulk) and each core piece. Initial values prior to hydrate formation on left and final post hydrate formation values on right. Experimental measurements in bold colors, 1-D simulation results in lighter colors, and 2-D simulation results in dashed colors.

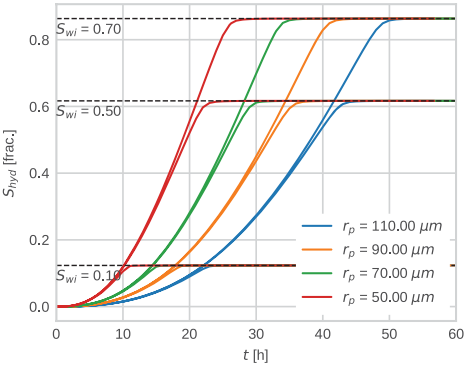

Figure 9. Effect of mean particle radius (r_p) and initial brine saturation (S_{wi}) on hydrate growth. Each simulation result shows hydrate saturation change through time for different cases, initialized with a specific particle size (50−110 μm) and initial brine saturation (0.1−0.7 fraction).

respectively for comparison with experimental measurements. In addition, extended visualizations in time for both experiments are included in Figures 12 and 13.

For experiment 1, small variations in the distribution of phases were neglected and simulations were initialized by having a homogeneous two-phase distribution of gas (0.38 fraction) and brine (0.62 fraction). Enabling the capillary function did not result in major changes in the simulations; therefore, the results presented in this section concern only the simulations run without the capillary function enabled. The area adjustment factor (F_A) was reduced to 1.59 × 10^{-3} to stretch the reaction time and match the experimental data. Mean particle sizes of the media representing Bentheim

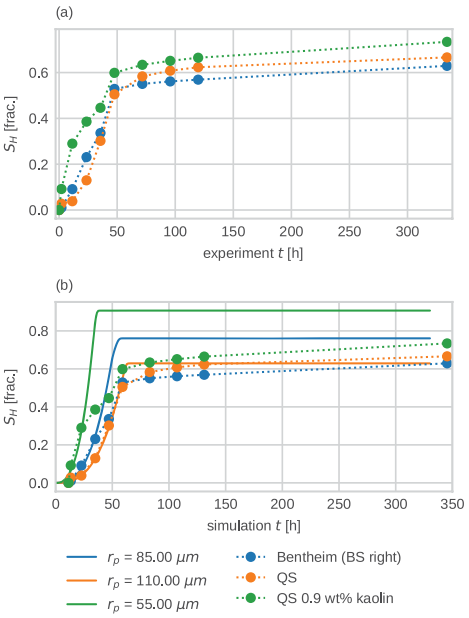

Figure 10. Experiment 1. (a) Time development of hydrate saturation in quartz sand (QS), quartz sand containing 0.9 wt % kaolin, and Bentheim sandstone (BS right). (b) In continuous lines, simulated hydrate saturation for the corresponding sections. Area adjustment factor (F_A) set to 1.59 × 10^{-3}. Experimental measurements are added for comparison with a time shift to compensate nondetectable slow growth within the first hours of simulation.

sandstone and quartz sand containing 0.9 wt % kaolin were adjusted to 85 and 55 μm, respectively. The simulation time for experiment 1 was shifted to compensate for the early slow hydrate growth that can be undetected experimentally. Such a shift accounted for the first 10 h of simulation (Figure 10b). Initial hydrate growth was faster in the material with the smallest particle size (55 μm) and leveled out around 0.91 (fraction). Hydrate growth continued at a slower rate as the particle size increased. The final hydrate saturation leveled off in 85 and 110 μm at 0.76 and 0.63 (fraction), respectively. The final bulk water and hydrate saturation after hydrate formation were 0.01 and 0.76 (fraction) (Figures 10b and 12).

Experiment 2 was initialized with a heterogeneous distribution of fluids along the core. Enabling the capillary function prevented the simulation from preserving the heterogeneous distribution of fluids. Therefore, this feature was disabled and the results presented for the simulations of experiment 2 do not consider capillary pressure. To keep consistency with experiment 1, the particle size of Bentheim sandstone was set to 85 μm and the particle sizes of the sand mixtures containing 3.4, 6.1, and 12.4 wt % kaolin were set to 50, 45, and 40 μm, respectively. Hydrate growth responds to both the particle size and the mobility of gas throughout the system. Although hydrate growth starts earlier in the quartz sand containing 3.4 wt % kaolin (50 μm), hydrate growth in the Bentheim sandstone (85 μm) rapidly stagnates around

https://doi.org/10.1021/acs.energyfuels.1c00549
Energy Fuels 2021, 35, 9836−9846

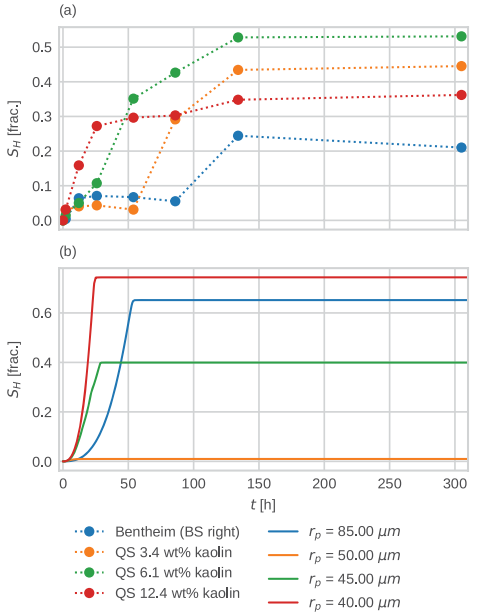

Figure 11. Experiment 2. (a) Time development of hydrate saturation in quartz sand (QS) containing 3.4, 6.1, and 12.4 wt % kaolin, and Bentheim sandstone (BS right). (b) Simulated hydrate saturation for the corresponding sections. Area adjustment factor (F_A) set to 1.59×10^{-3}.

0.01 (fraction). A similar process is observed in the quartz sand containing 6.1 wt % kaolin (45 μm). The modeled sequential hydrate growth was found to be very sensitive to variability in the initial distribution of fluids and the dynamics governing the boundary conditions. The final bulk water and hydrate saturation after hydrate formation were 0.43 and 0.44 (fraction), respectively (Figures 11b and 13).

Exchange of brine and gas between each grid section was tracked for both 2-D simulations. Most of the water that took part in hydrate formation at each core piece was observed to be sourced mainly from the initial water saturation of that grid region. Very small amounts of brine were exchanged between them. Active fluxes of gas between each grid region occurred and were only hindered by the regions with high saturation of brine in 2-D simulations for experiment 2 (Figure 13).

DISCUSSION

Effect of Clay on Hydrate Formation Rate. Results from both experiments reveal how the initial water distribution governs the final water and hydrate distribution. This is evident from Figures 4 and 5 and has also been verified earlier by Almenningen et al.[35]

The variation of initial water saturation along the length of the sediments in experiment 2 explains also part of the observed sequential growth rate of hydrate. However, it does not account for the slow and limited hydrate formation in the Bentheim sandstone at $L > 0.75$ (fraction); water saturation was in fact the lowest (0.54 volume fraction) and most ideal for hydrate formation.

The sequential growth of hydrate is also contrary to the applied temperature gradient; the temperature was decreasing from right to left (8.1 °C at $L = 1$ fraction, 5.3 °C at $L = 0$ fraction). The observed sequential growth rate of hydrate may therefore be explained by the content of kaolin in the quartz sand. Small kaolin particles fill the pore space between the quartz sand particles, and the observed growth rate of hydrate may be a pore size phenomenon.[40] The surface energy and texture of kaolin particles may also affect the nucleation of hydrate. This may be explained by a shift in the pore-scale

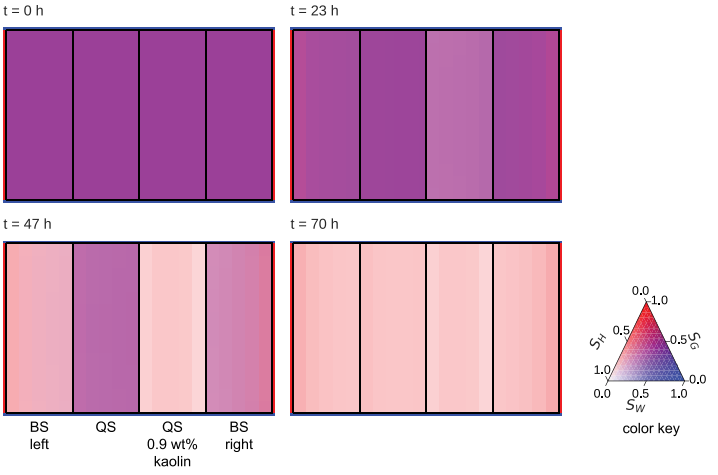

Figure 12. Experiment 1. Visualization of 2-D simulation results at different points in time. The color shade is proportional to the saturation of each phase. Hydrate (white), brine (blue), and gas (red). The last visualization is shown when hydrate growth has reached a steady state.

https://doi.org/10.1021/acs.energyfuels.1c00549
Energy Fuels 2021, 35, 9836−9846

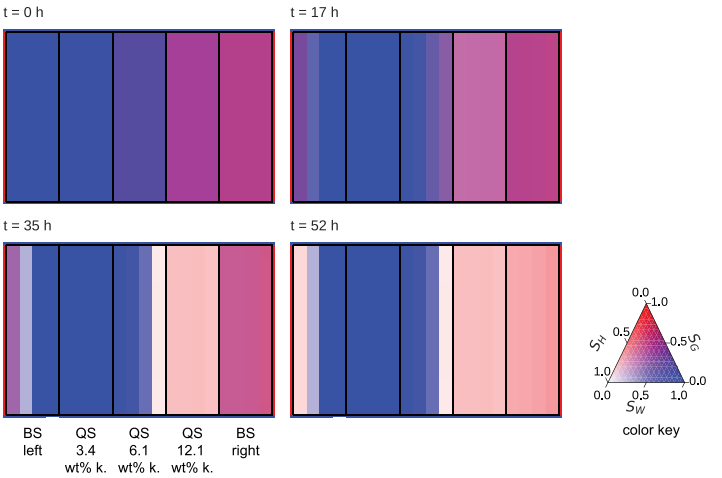

Figure 13. Experiment 2. Visualization of 2-D simulation results at different points in time. The color shade is proportional to the saturation of each phase. Hydrate (white), brine (blue), and gas (red). The last visualization is taken within the time all hydrate growth has reached a steady state.

hydrate growth pattern when the kaolin content exceeds a threshold.

The shift in average T_2 suggests a change in the pore-scale hydrate growth pattern when the kaolin content is changing. The loss of short T_2 components in quartz sand with high kaolin content implies hydrate formation close to the surface of clay and quartz particles.

Comparison between Numerical and Experimental Results. Simulation results show major deviations from the experimental results. The simulated systems are constrained by the assumptions in the model, and some mechanisms in the hydrate growth may not be accounted for.

It is, however, possible to make a qualitative comparison and attempt to understand where the limitations of the simulation model are. These limitations are analyzed from the methods used by T+H to model both hydrate growth and multiphase flow in the presence of hydrates, and how these affect each other. Both modeled hydrate growth and measured hydrate growth (Figures 9−11) are described in terms of the different stages of growth, based on the work by Yin et al.[19]

Induction Time (Stage I). Kowalsky and Moridis[32] have pointed out that the kinetic model does not account for nucleation phenomena. In the coarse grid used in this study, this results in the evolution of a homogeneous hydrate phase in each grid cell where formation is occurring. This effect makes the model deviate from the potential heterogeneous spatial distribution of hydrates.[40−42] However, the hydrate saturation reached toward the end of this stage is comparable to the early measurements made in both experiments (Figures 10 and 11).

Main Hydrate Growth (Stage II). Using particle size as a proxy for kaolin content provides a good approximation to model hydrate growth comparable to the experiments within the early part of this stage. Both experiments and simulations returned a sequential growth that was steeper in the core pieces with the highest content of kaolin (the smallest particle size) than in the pieces with little to no kaolin content.

Both experiments show changes in the hydrate growth rate at each core piece that may not be caused solely by the variations in the content of kaolin. The simulation results deviated largely from both experiments at this stage and did not manage to reproduce the observed changes in the hydrate growth rate. However, when different materials with different particle sizes are set adjacent to each other, the simulations show that hydrate growth is not constrained only by the kinetic model. When hydrate growth is modeled in homogeneous materials, the resulting hydrate growth is only a function of the particle size and the initial saturation of brine and gas. The particle size has a direct influence on how the growth reaches stages I and II of hydrate formation as seen in Figure 9. The initial fluid saturation determines at which point the growth will slow down and reach a steady state (stages III and IV). In the heterogeneous configuration of the 2-D grid (Figure 3), a new constraint is added to the modeled growth. Local formation of hydrates may have an impact on subsequent hydrate growth occurring in adjacent regions. These types of interferences are observed in 2-D simulations of both experiments. In the simulations of experiment 1, by the time growth in the Bentheim sandstone starts, hydrate formation in the quartz sand containing 0.9 wt % kaolin has already consumed part of the initial volume of brine. A similar situation is observed when hydrates are formed in the clean quartz sand. This effect results in each section of the grid reaching a progressively lower final saturation of hydrates (Figure 10b). In the simulations of experiment 2, the interaction between grid regions is more pronounced. The growth of hydrates is constrained not only by previous growth in other regions of the grid but also by the heterogeneous distribution of brine (Figure 11b). The high saturation of brine on the left side of the grid reduces the mobility of gas in this area. Although hydrate growth starts earlier in the sand with 3.4 wt % kaolin than in the Bentheim region, the growth slows down early and stagnates at a very low saturation (Figures 11 and 13). In the remaining materials, the growth rate at which

https://doi.org/10.1021/acs.energyfuels.1c00549
Energy Fuels 2021, 35, 9836−9846

each material reaches stage II varies according to their particle size. However, the final saturation at which growth slows down and reaches stage III is influenced mainly by the initial saturation of brine.

The different growth rates observed in both experiments may respond to interferences similar to those observed in the 2-D simulations. However, the lack of data characterizing the pore network properties of the materials and potential mechanisms not considered by T+H makes the modeling of such processes difficult.

The changes in flow patterns driven by local hydrate growth observed in the 2-D simulations are expected to behave differently if the effects of kaolin content and hydrate formation on pore network properties are considered. The different contents of kaolin in the sand mixtures are expected to have an impact on the intrinsic permeability and the relationships describing both the capillary pressure and relative permeability. The evolution of a solid hydrate phase is also expected to modify such properties. Although some of these mechanisms can be represented by T+H, they still need input data to narrow the range of uncertainty of the results.

Simulations of experiment 1 with and without capillary pressure function yielded near identical results and suggest that the displacements of methane and brine linked to the formation of hydrates are driven mainly by Darcy flow. However, in experiment 2, the capillary pressure function had immediate effects on the initialization of the system. When the capillary function model is enabled, the capillary pressure of each fluid phase is calculated. The fluid pressure of the nonwetting phase (methane) is assigned to 83 bar. The pressure in the wetting phase (brine) is close to 83 bar in the sections of the core where the brine saturation is close to 1.0 fraction, but it becomes less in the parts with lower brine saturation (Figure 14). This pressure gradient causes an almost

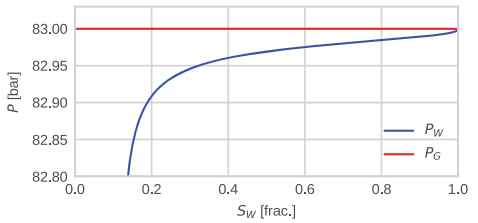

Figure 14. Fluid phase pressures of both water (P_W) and gas (P_G) when capillary pressure function is activated at varying water saturation (S_W). The system is confined 83 bar and uses model described in Table 1.

immediate redistribution of the fluid phases until there is no pressure imbalance. This mechanism hindered the use of the capillary pressure model and the analysis of the combined effects of kaolin and hydrate formation as well as the final saturation of hydrates.

The decrease in hydrate growth rate observed in the experiments can also be related to self-inhibitory hydrate formation mechanisms in porous media that cannot be represented by T+H. Hydrates have been observed to form randomly in pore spaces, causing local increases in saturation. These saturations can cause local hindrances for fluid flow,[43] which result in pores and throats becoming disconnected from each other and creating dead ends for flow.[44] Hydrate formation can also result in the evolution of both nonporous crystalline hydrates and porous hydrate shells with encapsulated fluids[45] that will no longer take part in the reaction within the time scale of the experiments.

Decrease in Growth and Steady State (Stages III and IV). Regarding the total amount of hydrate yielded, numerical simulations yielded contrasting results. Experiment 1 yielded almost as much hydrate as both 1-D and 2-D models did (Figure 7). At a core-piece level, both measurements and simulation show that the highest saturation of hydrate occurs in the quartz sand containing 0.9 wt % kaolin clay (Figure 7). The near homogeneous distribution of fluid phases prior to hydrate formation ensures an efficient contact between both fluid phases, resulting in a productive formation of hydrates in all core pieces.

One-dimensional simulations for experiment 2 showed a large deviation from both 2-D simulations and experimental measurements (Figure 8, right). The ideal system represented by the 1-D model guarantees that both gas and brine are always in contact, similar to experiment 1. With a heterogeneous distribution of brine, this is unlikely to happen. Two-dimensional simulations of experiment 2 yielded a bulk amount of hydrate comparable to that formed experimentally (Figure 8). The remaining brine saturation in the 2-D simulations (0.43 fraction) is also lower but comparable to the one yielded in the experiments (0.51 fraction).

In contrast, the heterogeneous water saturation in experiment 2 inhibits the system from forming hydrates as efficiently as 1-D simulations did. Both 2-D simulations and experimental results show that there is a large fraction of brine that does not react with gas (0.51 fraction) (Figure 8).

When each core piece is compared with its corresponding grid section in the 2-D model, the final distribution of hydrates shows large deviations (Figure 8). Most of the hydrate formation modeled in the 2-D simulations occurred in the right part of the system, in the regions representing the Bentheim sandstone (BS right) and the quartz sand containing 12.4 wt % kaolin (Figures 8 and 13). Limited to no growth is observed in the remaining grid regions. This is caused by the reduced mobility of gas. By the time hydrates start forming, the relative permeability is too low for methane to reach the inner parts of the system.

Thus, in terms of material balance, both 2-D models are able to form an amount of hydrate comparable to those acquired in the experiments. However, the limited characterization of the intrinsic properties of the system results in hydrates being distributed differently along the system. In addition, cross-flow of gas between layers causing changes of internal fluid saturations are observed. As mentioned above, hydrate growth may act as barriers for mass exchange and thus a significant amount of water may be disconnected from the gas phase and temporarily hinder hydrate formation. The detailed growth of hydrates that causes this combined effect will most likely be particular for a given experiment. However, for longer time scales and larger length scales, phenomena such as naturally occurring flow, diffusion, and Ostwald ripening are expected to drive the system toward an equilibrium situation within the local constraints of pressure and temperature gradients.

https://doi.org/10.1021/acs.energyfuels.1c00549
Energy Fuels 2021, 35, 9836−9846

CONCLUSIONS

- Methane gas hydrate phase transitions in unconsolidated quartz sand were imaged and the water distribution was mapped using MRI. The kaolin content of the sand ranged from 0 to 12 wt % in order to investigate the effect of clay on hydrate phase transitions.
- Experiments show that hydrate growth was significantly faster with increasing clay content. The final hydrate saturation was mainly governed by the initial water saturation.
- A shift in average T_2 during hydrate growth was observed for the highest clay content in sand. Hydrate was inferred to form close to the clay and sand surfaces when the sand contained 12 wt % clay, contrary to the pore-filling hydrate in sand containing less clay.
- One-dimensional models provided insight into the potential hydrate growth and final saturation in ideal conditions.
- By using particle size as a proxy for kaolin content, 2-D simulations reproduced a sequential hydrate growth similar to the one observed in the experiments.
- Deviations between simulations and experiments may be attributed to the effects of hydrates on intrinsic properties such as permeability and capillary pressure as well as the dynamic effects of local hydrate barriers and cross-flow between layers that is specific to each experiment.

AUTHOR INFORMATION

Corresponding Author

Alejandro Bello-Palacios − *Equinor ASA, 5020 Bergen, Norway; Department of Physics and Technology, University of Bergen, 5020 Bergen, Norway;* orcid.org/0000-0002-0294-9485; Phone: +47 941 56 014; Email: gpb@equinor.com

Authors

Stian Almenningen − *Department of Physics and Technology, University of Bergen, 5020 Bergen, Norway;* orcid.org/0000-0002-2839-8503

Per Fotland − *Equinor ASA, 5020 Bergen, Norway*

Geir Ersland − *Department of Physics and Technology, University of Bergen, 5020 Bergen, Norway*

Complete contact information is available at: https://pubs.acs.org/10.1021/acs.energyfuels.1c00549

Notes

The authors declare no competing financial interest.

ACKNOWLEDGMENTS

This work was supported by funding from the Norwegian Research Council. Equinor ASA is thanked for permission to publish this work.

REFERENCES

(1) Boswell, R.; Schoderbek, D.; Collett, T. S.; Ohtsuki, S.; White, M.; Anderson, B. J. The Iġnik Sikumi Field Experiment, Alaska North Slope: Design, Operations, and Implications for CO2−CH4 Exchange in Gas Hydrate Reservoirs. *Energy Fuels* **2017**, *31*, 140−153.

(2) Konno, Y.; Fujii, T.; Sato, A.; Akamine, K.; Naiki, M.; Masuda, Y.; Yamamoto, K.; Nagao, J. Key Findings of the World's First Offshore Methane Hydrate Production Test off the Coast of Japan: Toward Future Commercial Production. *Energy Fuels* **2017**, *31*, 2607−2616.

(3) Yamamoto, K.; Dallimore, S. Aurora-JOGMEC-NRCan Mallik 2006−2008 gas hydrate research project progress. *Fire in the Ice* **2008**, No. Summer, 1−8.

(4) Moridis, G. J.; Kowalsky, M. B.; Pruess, K. Depressurization-Induced Gas Production From Class-1 Hydrate Deposits. *SPE Reservoir Eval. Eng.* **2007**, *10*, 458−481.

(5) Boswell, R.; Collett, T. S. Current perspectives on gas hydrate resources. *Energy Environ. Sci.* **2011**, *4*, 1206−1215.

(6) Yoneda, J.; Masui, A.; Konno, Y.; Jin, Y.; Kida, M.; Katagiri, J.; Nagao, J.; Tenma, N. Pressure-core-based reservoir characterization for geomechanics: Insights from gas hydrate drilling during 2012−2013 at the eastern Nankai Trough. *Mar. Pet. Geol.* **2017**, *86*, 1−16.

(7) Kwon, T.-H.; Oh, T.-M.; Choo, Y. W.; Lee, C.; Lee, K.-R.; Cho, G.-C. Geomechanical and Thermal Responses of Hydrate-Bearing Sediments Subjected to Thermal Stimulation: Physical Modeling Using a Geotechnical Centrifuge. *Energy Fuels* **2013**, *27*, 4507−4522.

(8) Uchida, S.; Klar, A.; Yamamoto, K. Sand production model in gas hydrate-bearing sediments. *International Journal of Rock Mechanics and Mining Sciences* **2016**, *86*, 303−316.

(9) Wu, N.; Li, Y.; Chen, Q.; Liu, C.; Jin, Y.; Tan, M.; Dong, L.; Hu, G. Sand Production Management during Marine Natural Gas Hydrate Exploitation: Review and an Innovative Solution. *Energy Fuels* **2021**, *35*, 4617−4632.

(10) Han, G.; Kwon, T.; Lee, J. Y.; Kneafsey, T. J. Depressurization-Induced Fines Migration in Sediments Containing Methane Hydrate: X-Ray Computed Tomography Imaging Experiments. *J. Geophys. Res.: Solid Earth* **2018**, *123*, 2539−2558.

(11) Waite, W. F.; Jang, J.; Collett, T. S.; Kumar, P. Downhole physical property-based description of a gas hydrate petroleum system in NGHP-02 Area C: A channel, levee, fan complex in the Krishna-Godavari Basin offshore eastern India. *Mar. Pet. Geol.* **2019**, *108*, 272−295.

(12) Torres, M. E.; Tréhu, A. M.; Cespedes, N.; Kastner, M.; Wortmann, U. G.; Kim, J. H.; Long, P.; Malinverno, A.; Pohlman, J. W.; Riedel, M.; Collett, T. Methane hydrate formation in turbidite sediments of northern Cascadia, IODP Expedition 311. *Earth Planet. Sci. Lett.* **2008**, *271*, 170−180.

(13) Santamarina, J. C.; Dai, S.; Terzariol, M.; Jang, J.; Waite, W. F.; Winters, W. J.; Nagao, J.; Yoneda, J.; Konno, Y.; Fujii, T.; Suzuki, K. Hydro-bio-geomechanical properties of hydrate-bearing sediments from Nankai Trough. *Mar. Pet. Geol.* **2015**, *66*, 434−450.

(14) Uchida, T.; Takeya, S.; Chuvilin, E. M.; Ohmura, R.; Nagao, J.; Yakushev, V. S.; Istomin, V. A.; Minagawa, H.; Ebinuma, T.; Narita, H. Decomposition of methane hydrates in sand, sandstone, clays, and glass beads. *J. Geophys. Res.* **2004**, *109*, B05206.

(15) Kumar Saw, V.; Udayabhanu, G.; Mandal, A.; Laik, S. Methane Hydrate Formation and Dissociation in the Presence of Silica Sand and Bentonite Clay. *Oil Gas Sci. Technol.* **2015**, *70*, 1087−1099.

(16) White, M. D.; et al. An international code comparison study on coupled thermal, hydrologic and geomechanical processes of natural gas hydrate-bearing sediments. *Mar. Pet. Geol.* **2020**, *120*, 104566.

(17) Wilder, J. W.; Moridis, G. J.; Wilson, S. J.; Kurihara, M.; White, M. D.; Masuda, Y.; Anderson, B. J.; Collett, T. S.; Hunter, R. B.; Narita, H. An international effort to compare gas hydrate reservoir simulators. *Proceedings of 6th International Conference on Gas Hydrates (ICGH 2008), Vancouver, Canada*; National Energy Technology Laboratory: 2008.

(18) Liu, Y.; Gamwo, I. K. Comparison between equilibrium and kinetic models for methane hydrate dissociation. *Chem. Eng. Sci.* **2012**, *69*, 193−200.

(19) Yin, Z.; Khurana, M.; Tan, H. K.; Linga, P. A review of gas hydrate growth kinetic models. *Chem. Eng. J.* **2018**, *342*, 9−29.

(20) Uddin, M.; Coombe, D.; Law, D.; Gunter, B. Numerical Studies of Gas Hydrate Formation and Decomposition in a Geological Reservoir. *J. Energy Resour. Technol.* **2008**, *130*, 032501.

(21) Moridis, G.; Pruess, K. *User's Manual of the TOUGH+ v1. 5 Core Code: A General Purpose Simulator of Non-isothermal Flow and Transport through Porous and Fractured Media*; Report LBNL-6871E; Lawrence Berkeley National Laboratory: Berkeley, CA, 2014.

(22) Palodkar, A. V.; Jana, A. K. Gas hydrate dynamics in distributed porous particles with saltwater: Model formulation and experimental validation. *Chem. Eng. J.* **2020**, *392*, 123660.
(23) Sun, X.; Mohanty, K. K. Kinetic simulation of methane hydrate formation and dissociation in porous media. *Chem. Eng. Sci.* **2006**, *61*, 3476−3495.
(24) Moridis, G. *User's Manual for the HYDRATE v1. 5 Option of TOUGH+ v1. 5: A Code for the Simulation of System Behavior in Hydrate-Bearing Geologic Media*; Report LBNL-6869E; Lawrence Berkeley National Laboratory: Berkeley, CA, 2014.
(25) Gamwo, I. K.; Liu, Y. Mathematical Modeling and Numerical Simulation of Methane Production in a Hydrate Reservoir. *Ind. Eng. Chem. Res.* **2010**, *49*, 5231−5245.
(26) Moridis, G. J.; Collett, T. S.; Dallimore, S. R.; Satoh, T.; Hancock, S.; Weatherill, B. Numerical studies of gas production from several CH4 hydrate zones at the Mallik site, Mackenzie Delta, Canada. *J. Pet. Sci. Eng.* **2004**, *43*, 219−238.
(27) Li, B.; Li, X.-S.; Li, G.; Chen, Z.-Y. Evaluation of gas production from Qilian Mountain permafrost hydrate deposits in two-spot horizontal well system. *Cold Reg. Sci. Technol.* **2015**, *109*, 87−98.
(28) Sun, J.; Ning, F.; Zhang, L.; Liu, T.; Peng, L.; Liu, Z.; Li, C.; Jiang, G. Numerical simulation on gas production from hydrate reservoir at the 1st offshore test site in the eastern Nankai Trough. *J. Nat. Gas Sci. Eng.* **2016**, *30*, 64−76.
(29) Jin, G.; Lei, H.; Xu, T.; Xin, X.; Yuan, Y.; Xia, Y.; Juo, J. Simulated geomechanical responses to marine methane hydrate recovery using horizontal wells in the Shenhu area, South China Sea. *Mar. Pet. Geol.* **2018**, *92*, 424−436.
(30) Li, B.; Li, X.-S.; Li, G. Kinetic studies of methane hydrate formation in porous media based on experiments in a pilot-scale hydrate simulator and a new model. *Chem. Eng. Sci.* **2014**, *105*, 220−230.
(31) Yin, Z.; Moridis, G.; Tan, H. K.; Linga, P. Numerical analysis of experimental studies of methane hydrate formation in a sandy porous medium. *Appl. Energy* **2018**, *220*, 681−704.
(32) Kowalsky, M. B.; Moridis, G. J. Comparison of kinetic and equilibrium reaction models in simulating gas hydrate behavior in porous media. *Energy Convers. Manage.* **2007**, *48*, 1850−1863.
(33) Kim, H. C.; Bishnoi, P. R.; Heidemann, R. A.; Rizvi, S. S. H. Kinetics of methane hydrate decomposition. *Chem. Eng. Sci.* **1987**, *42*, 1645−1653.
(34) Almenningen, S.; Graue, A.; Ersland, G. Experimental Investigation of Critical Parameters Controlling CH4-CO2 Exchange in Sedimentary CH4 Hydrates. *Energy Fuels* **2021**, *35*, 2468−2477.
(35) Almenningen, S.; Fotland, P.; Ersland, G. Magnetic Resonance Imaging of Methane Hydrate Formation and Dissociation in Sandstone with Dual Water Saturation. *Energies* **2019**, *12*, 3231.
(36) Birkedal, K. A.; Freeman, C. M.; Moridis, G. J.; Graue, A. Numerical Predictions of Experimentally Observed Methane Hydrate Dissociation and Reformation in Sandstone. *Energy Fuels* **2014**, *28*, 5573−5586.
(37) Clarke, M.; Bishnoi, P. R. Determination of the activation energy and intrinsic rate constant of methane gas hydrate decomposition. *Can. J. Chem. Eng.* **2001**, *79*, 143−147.
(38) Stone, H. Probability model for estimating three-phase relative permeability. *JPT, J. Pet. Technol.* **1970**, *22*, 214−218.
(39) van Genuchten, M. T. A Closed-form Equation for Predicting the Hydraulic Conductivity of Unsaturated Soils. *Soil Science Society of America Journal* **1980**, *44*, 892−898.
(40) Bagherzadeh, S. A.; Moudrakovski, I. L.; Ripmeester, J. A.; Englezos, P. Magnetic Resonance Imaging of Gas Hydrate Formation in a Bed of Silica Sand Particles. *Energy Fuels* **2011**, *25*, 3083−3092.
(41) Seol, Y.; Kneafsey, T. J. X-ray computed-tomography observations of water flow through anisotropic methane hydrate-bearing sand. *J. Pet. Sci. Eng.* **2009**, *66*, 121−132.
(42) Priegnitz, M.; Thaler, J.; Spangenberg, E.; Schicks, J. M.; Schrötter, J.; Abendroth, S. Characterizing electrical properties and permeability changes of hydrate bearing sediments using ERT data. *Geophys. J. Int.* **2015**, *202*, 1599−1612.
(43) Yang, L.; Ai, L.; Xue, K.; Ling, Z.; Li, Y. Analyzing the effects of inhomogeneity on the permeability of porous media containing methane hydrates through pore network models combined with CT observation. *Energy* **2018**, *163*, 27−37.
(44) Sun, J.; Dong, H.; Arif, M.; Yu, L.; Zhang, Y.; Golsanami, N.; Yan, W. Influence of pore structural properties on gas hydrate saturation and permeability: A coupled pore-scale modelling and X-ray computed tomography method. *J. Nat. Gas Sci. Eng.* **2021**, *88*, 103805.
(45) Almenningen, S.; Iden, E.; Fernø, M. A.; Ersland, G. Salinity Effects on Pore-Scale Methane Gas Hydrate Dissociation. *Journal of Geophysical Research: Solid Earth* **2018**, *123*, 5599−5608.

https://doi.org/10.1021/acs.energyfuels.1c00549
Energy Fuels 2021, 35, 9836−9846

Paper III

A.3 Modelling the effects of sedimentation on natural occurrences of CH_4 hydrates in marine sediments

Alejandro Bello-Palacios, Per Fotland, and Geir Ersland

Energy & Fuels, published online in March 2022.

energy&fuels

pubs.acs.org/EF

Article

Modeling the Effects of Sedimentation on Natural Occurrences of CH_4 Hydrates in Marine Sediments

Alejandro Bello-Palacios,* Per Fotland, and Geir Ersland

Cite This: https://doi.org/10.1021/acs.energyfuels.1c03611

Read Online

ACCESS | Metrics & More | Article Recommendations

ABSTRACT: This study explores the relationships that sedimentation rate and transport properties have with the formation and evolution of hydrates in fine-grained marine sediments and their corresponding bottom simulating reflector (BSR) responses. Using a series of one-dimensional simulations of multiphase, multicomponent flow and transport of mass and heat through porous media, a slab of sediments through sedimentation is modeled. The boundary conditions are set to emulate the pressure and geothermal gradients and its resulting gas hydrate stability zone (GHSZ). Hydrates are formed by injecting methane gas through the bottom of the grid and letting it migrate and reach the boundary of stability. The resulting hydrate accumulation is subjected to different sedimentation rates and replicated with different intrinsic permeability. With sedimentation, the geothermal gradient is displaced upward and the boundary of stability shoals. Through methane recycling, the distribution of phases changes through cycles of slow melting and rapid reformation. This results in a dynamic flow barrier that relocates the base of the GHSZ over geological time, in response to the variations of both pressure and salinity. The characteristics of a BSR response will be tied to the stage of the melting cycle.

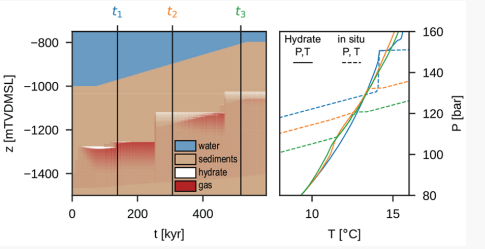

INTRODUCTION

Gas hydrates are crystalline ice-like solids formed by the mixing of water and gas under pressure. Water molecules form hydrogen-bonded structures with cavities that are stabilized by the filling of nonpolar or slightly polar guest gas molecules.[1]

In nature, methane is a predominant guest molecule[2] that forms hydrates at relatively low temperatures and high pressures.[1] Permafrost regions and deep marine sediments in the outer continental margins are known to host widespread accumulations of methane hydrates.[3] Estimates suggest that the latter hosts the majority of methane hydrates in nature.[4]

Several occurrences of deep marine hydrates have been identified and targeted for both scientific and commercial purposes. The International Ocean Discovery Program (IODP)/Ocean Drilling Program (ODP) scientific results from leg 164 at Blake Ridge,[5] leg 204 in the Hydrate Ridge in offshore Oregon,[6] and expedition 311 at the Northern Cascadia margin[7] have provided crucial data to study and monitor hydrate systems in this setting. The Nyegga pockmark field in offshore mid-Norway is another occurrence that has been studied in detail.[8] In addition, the governments of the U.S.A., Japan, South Korea, India, and China have initiated national-led programs to evaluate the economical prospectivity of hydrate occurrences in the Gulf of Mexico, Nankai Trough, Ulleung Basin, Krishna Godavari Basin, and South China Sea, respectively.[9]

The characteristics of these occurrences vary greatly in terms of their physical form and geological environment.[10] Some of the hydrate accumulations identified in both Blake Ridge[11] and the South China Sea[12] occur in fine-grained sediments with hydrates concentrated toward the base of the gas hydrate stability zone (GHSZ). Recycling of methane can explain the formation of such localized concentrations.[13,14] This mechanism works by active sedimentation driving hydrates out of the GHSZ. As the hydrates start melting, the expelled gas accumulates, driven by buoyancy, flows back into the GHSZ, and forms new hydrates. Methane migrating from far beneath the stability boundary can also enrich these hydrate accumulations.[15] The contrast in acoustic impedance caused by the interface between the expelled gas and hydrate can produce a bottom simulating reflector (BSR),[16] a seismic reflection that follows the shape of the seafloor and can coincide with the base of stability of hydrates.[17]

Numerical modeling has been crucial to study gas hydrate occurrences in geological systems.[10] It involves the use of fully

Received: October 22, 2021
Revised: February 26, 2022

coupled, multiphase, and multicomponent methane hydrate formation models. Multiple tools have been tested and compared[18,19] to validate and build confidence in the modeling of hydrate-related processes in porous media.

Some of these tools have been used to model deep marine hydrate systems. Using Blake Ridge as a case study, Burwicz and Rüpke[20] and You and Flemings[21] have thoroughly modeled the formation and evolution of a hydrate system with sediment burial and compaction. Focusing more on the mechanisms driving the concentration of hydrates, Nole et al.[22] developed a model to simulate methane recycling in marine hydrate systems. Similarly, Liu and Flemings[15] simulated hydrate formation from a methane source far beneath the GHSZ.

The TOUGH+HYDRATE (T+H) version 1.5[23,24] code and its open-source version HydrateResSim[25] are also publicly available codes that have taken part in code-comparison studies.[18,19] They have been used primarily to evaluate the methane production from natural hydrate systems.[26−29] In addition, T+H has been used to model systems over larger time scales representing geological processes.[30,31]

These numerical tools offer an opportunity to analyze the complexities of these natural systems. These tools are capable of simulating multiple processes occurring simultaneously at different spatial and time scales. To do this, they have to account for the dynamic effects of hydrate formation and dissociation on salinity, temperature, pressure, and transport properties.[15]

This study looks at how the physical form of a hydrate occurrence can be affected by changes in both geology and environment. Special focus is given to the role of sedimentation on the evolution of an already established methane hydrate occurrence. In each simulation, all variations in the temperature, pressure, phase saturation, and concentration of soluble components among other parameters are logged. This information is used to describe the occurring mechanisms that mark the evolution of a hydrate occurrence and to explain how the geological history of a basin can determine the expression of a BSR.

METHODS

All simulations were performed in T+H. Developed by Lawrence Berkeley National Laboratory (LBNL), it simulates the behavior of methane-hydrate-bearing sediments and handles both multiphase, multicomponent flow and transport of mass and heat through porous and fractured media.[23,24] An overview of the simulation runs included in the results is shown in Table 1.

In T+H, hydrate formation and dissociation are modeled using either an equilibrium or kinetic model. Kowalsky and Moridis[32] have compared both approaches and concluded that they are practically indistinguishable. Kinetic limitation becomes important in short-term processes or core-scale simulations. Thus, this study uses the equilibrium approach only.

In the equilibrium model, phase transitions are governed only by pressure and temperature. Water and methane are mass components, and hydrate is one of the potential phases that can be present in different combinations (Figure 1).

Modeling Approach and Initialization. The simulation grid consists of a one-dimensional (1D) representation of marine sediments. The total thickness modeled is 600 m with a vertical resolution of 1 m. Thermophysical properties and parameters used in the simulations are included in Table 2.

The grid is initialized fully saturated by brine (3.5 wt % NaCl), and boundary conditions at the top and bottom of the grid are set to emulate the natural pressure and temperature gradients of seafloor

Table 1. Overview of Simulation Runs

case number	modeled process	based on
1A	hydrate formation without scaling k and P_{ce} k = 10 mD	
1B	hydrate formation with scaling k and P_{ce} k = 10 mD	
1C	hydrate formation with scaling k and P_{ce} k = 10 μD	
2	hydrate evolution in an idle system no sedimentation rate; no gas source	1B
3A	hydrate evolution with sedimentation sedimentation rate = 220 mm/year; no gas source	1B
3B	hydrate evolution with sedimentation; k = 10 μD sedimentation rate = 220 mm/year; no gas source	1C
4	hydrate evolution with sedimentation sedimentation rate = 2 m/year; no gas source	1B

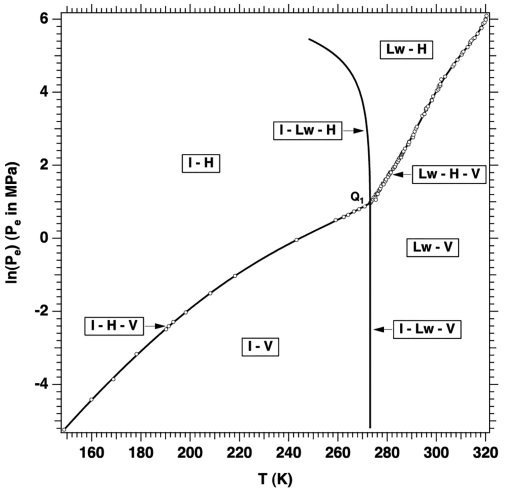

Figure 1. Pressure−temperature equilibrium relationship in the phase diagram of the water−methane−hydrate system. All possible combinations of the four phases are displayed: aqueous (Lw), ice (I), gas (V), and hydrate (H).[24]

sediments at 1000 m below mean sea level (Figure 2). At the top of the grid, a series of layers represent the water column and are set as an infinite boundary that keeps the pressure and temperature constant. At the bottom of the grid, a constant heat source emits the necessary heat to reach a thermal gradient close to 50 °C/km. Compaction of sediments is not considered; therefore, the initial intrinsic transport properties do not change along the thickness of the simulation grid.

We set an adjacent grid placed on each side of the main grid. The horizontal permeability between the main grid and these adjacent grids is zero through the largest part of the thickness (left panel of Figure 2). Fluid flow between these is possible only near the top or bottom of the grid. The purpose of this setup is to keep the pressure at the top and bottom of the grid always connected. In this manner, the restriction of flow caused by hydrates does cause pressure compartmentalization of the grid.

Hydrate Formation. Once the model is initialized and with a representative gradient of pressure and temperature, a flux of methane is initiated. The objective is to generate a hydrate accumulation as the buoyancy-driven flux of methane reaches the base of the GHSZ. The gas source delivers 12 kg of methane per millennium (kg of CH_4 m^{-2}

https://doi.org/10.1021/acs.energyfuels.1c03611
Energy Fuels XXXX, XXX, XXX−XXX

Table 2. Thermophysical Properties of Materials and Parameters Used in the Simulation Model

parameter	value
gas composition	100% CH_4
intrinsic permeability, $k_x = k_y = k_z$	1 mD (9.86×10^{-16} m^2)
intrinsic porosity, ϕ_0	0.30 fraction
density, ρ	2650 kg/m^3
brine salinity, X_{inh}	3.5 wt %
thermal conductivity, dry, λ_d	0.30 W m^{-1} K^{-1}
thermal conductivity, fully saturated, λ_w	1.40 W m^{-1} K^{-1}
specific heat, c_p	1400 J kg^{-1} K^{-1}
composite thermal conductivity model, λ	$\lambda = \lambda_d + (S_W^{1/2} + S_H^{1/2})(\lambda_w - \lambda_d)$
modified relative permeability model[33]	$k_{rA} = ((S_W - S_{irW})/(1 - S_{irW}))^{n_W}$ $k_{rG} = ((S_G - S_{irG})/(1 - S_{irG}))^{n_G}$ $k_{rH} = 0$ $n_W = 4.0$; $n_G = 2.0$ $S_{irW} = 0.11$; $S_{irG} = 0.02$
capillary pressure model[34]	$P_{cap} = -P_0\ [(S^*)^{-1/\gamma} - 1]^{1-\gamma}$ $S^* = ((S_W - S_{irW})/(S_{mxA} - S_{irW}))$ $\gamma = 0.7$; $S_{irW} = 0.1$ $P_0 = 22.2$ bar; $S_{mxA} = 1.0$
diffusion coefficients	1×10^{-10} m^2/s NaCl(aq) 1×10^{-10} m^2/s CH_4(aq) 1×10^{-5} m^2/s H_2O(g)
pressure at the top boundary (seabed)	104.5 bar at 1000 mTVDMSL
temperature at the top boundary (seabed)	0.1 °C (273.25 K)
basal heat flow rate	75 mW/m^2
methane source gas flow rate	12 kg of CH_4 m^{-2} kyr^{-1}
geothermal gradient	50 °C/km

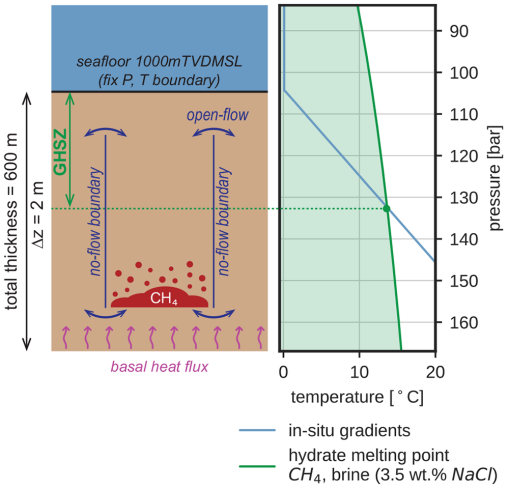

Figure 2. Schematic representation of the simulation model. The figure on the left shows the principal elements represented by the simulation model. The chart on the right shows the pressure and temperature at which the system is initialized (blue), superimposed by the curve representing the boundary of stability for CH_4 hydrate and 3.5 wt % brine NaCl. The green-shaded region highlights the P and T ranges, where hydrates are stable. The crossing between these two is defined as the base of the GHSZ.

kyr^{-1}). After 75 kyr, the simulations are arbitrarily stopped. At this point, the resulting distribution of phases and salinity might not equilibrate. Pressure buildups and peaks in the concentration of salinity will accompany the formation of hydrates. However, if the system is left to respond only to the boundary conditions and without a gas source, the time needed to bring it back to equilibrium will be longer than any of the processes modeled in this study.

T+H can modify transport properties (i.e., porosity, permeability, and capillary entry pressure) as a function of hydrate saturation (S_H). We model hydrate formation both with (case 1A) and without (case 1B) modification of transport properties. This alteration is expected to limit the fluid flow, increasing the concentration of hydrate toward the bottom of the GHSZ.

The modification of transport properties is defined by an evolutionary porosity model.[23] In this model, the hydrate is considered an extension of the matrix. The resulting effective porosity (ϕ) is equivalent to the intrinsic porosity (ϕ_0) reduced by the solid hydrate phase, expressed in eq 1.

$$\phi = \phi_0(1 - S_H) \tag{1}$$

This change in porosity is reflected in a scaling of both permeability (k) and capillary entry pressure (P_c).

Scaling of permeability is defined by a permeability reduction factor k_{rF}, expressed in eq 2 (top panel of Figure 3).

$$\left(\frac{k}{k_0}\right) = k_{rF} = \left(\frac{\phi - \phi_c}{\phi_0 - \phi_c}\right)^m \tag{2}$$

The critical porosity ϕ_c accounts for scenarios of hydrates clogging pore throats and disconnecting fluid-filled pores. It is linked to the saturation of hydrates at which the effective permeability is reduced to zero.

As the porosity and permeability change, the Leverett model (eq 3) is used to scale the capillary pressure (bottom panel of Figure 3). The input capillary pressure function was defined to match capillary pressure measurements from fine-grained marine sediments from the Gulf of Mexico[35] and Blake Ridge[36] regions. Both the hydrate-bearing and hydrate-free porosity and permeability from eqs 1 and 2 are used as inputs. Because hydrates are an extension of the matrix, the resulting scaled capillary pressure will reflect on the reduction of the effective radius of the pore throat.

$$P_c^* = P_c\sqrt{\frac{k_0}{k}\frac{\phi}{\phi_0}} \tag{3}$$

Sediment mechanics are not considered in these study. The formation of hydrates occurs uniformly and is constrained only by the pressure, temperature, salinity, and availability of methane and water.

Sedimentation Rate. Sedimentation is modeled by a series of continuous simulations. To emulate the process of sedimentation, the grid elements immediately above those representing the seafloor are progressively switched from an infinite boundary to a cell representing a new layer of sediment. The duration of each simulation is equivalent to the time it takes to deposit a 2 m thick layer at a given sedimentation rate. Assuming the temperature at the seafloor remains constant, the resulting temperature gradient is displaced upward. In response, the boundary of stability is progressively displaced in the same direction, forming a shallower and thinner GHSZ (Figure 4).

This setup is used to test how the previously formed hydrate occurrence responds to boundary conditions that change over time. Different sedimentation rates are tested, ranging from a low sedimentation rate (case 3, at 220 mm/year), comparable to that observed in the Blake Ridge,[37] to a system with higher sedimentation rates (case 4, at 2 m/year), comparable to those observed in places like the Nyegga area.[8] Particular attention is given to the process of methane recycling and how it affects the physical form of the final hydrate occurrence. For comparison, a simulation of an idle system where the boundary conditions remain unchanged is included in case 2.

https://doi.org/10.1021/acs.energyfuels.1c03611
Energy Fuels XXXX, XXX, XXX−XXX

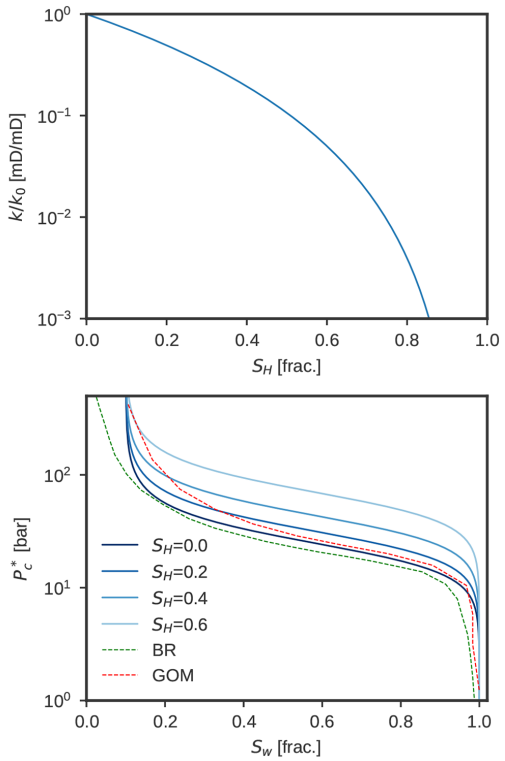

Figure 3. Scaling of both intrinsic permeability (top) and capillary pressure (bottom) in the presence of hydrates in T+H, with input parameters in Table 2. The initial capillary pressure curve (S_H = 0) was built using reference data from the Gulf of Mexico (GOM) and Blake Ridge (BR) sediments.[35,36]

Sediment compaction through burial is not considered in this study. As new layers are deposited, the transport properties remain unchanged.

RESULTS AND DISCUSSION

Initial Hydrate Formation. Two different hydrate accumulations were achieved during cases 1A and 1B. In both cases, the use of a capillary pressure curve (Figure 5) has modified the *in situ* pressure gradient with depth. With both gas and brine co-existing in the pores, the pressure in the gas phase has to overcome the capillary entry pressure of the given curve (near 10 bar). The resulting pressure gradients are no longer linear, and the excess pressure displaces the base of the GHSZ a few meters down (column 4 in Figure 5). In addition, the local increase of salinity that results from hydrate formation has also lifted the boundary of stability of hydrates.

In the cases where hydrate saturation did not affect the transport properties (top row of Figure 5), most methane was turned into hydrates. The resulting accumulation was a thick layer of hydrates (near 40 m) with residual gas only. Salinity increased locally to 6.4 wt % NaCl at the point of maximum hydrate saturation (68.7%).

Results varied greatly when hydrate saturation was used to scale both capillary pressure and permeability. As hydrates started forming, a smaller amount of gas was able to pass through the hydrate-saturated interval. The resulting accumulation concentrated in a thinner layer of hydrate. Because less hydrates have formed, the maximum salinity was 4.4 wt % NaCl. The remaining methane formed a gas accumulation trapped by hydrates. The capillary pressure resulting from this free gas accumulation displaced the base of the GHSZ further down.

The first scenario might produce a weak response not detectable as BSR. The second scenario would yield a stronger reflection. On the basis of these results, if the intrinsic capillary entry pressure of the host sediments is high, there would be a larger discrepancy in depth between the BSR and the thermodynamic phase boundary.

Evolution during Sedimentation. A useful feature of a numerical simulation like T+H is its capacity to keep track of all variables involved in hydrate transition phases and the transport of heat and mass. In complex systems, like those observed in this study, it becomes a powerful tool to understand the mechanisms behind the thermodynamic evolution of a hydrate occurrence over geological time. However, there are still limitations inherent to the simulator that constrain the capacity of this methodology. These limitations refer to the consideration of the mechanical properties of fine-grained sediments in two main processes: burial and compaction of sediments and the effects of hydrate formation in unconsolidated fine-grained sediments. For the first part, although it was possible to emulate the process of sedimentation by stacking up layers and updating the boundary condition, the resulting mechanical compaction of sediments was not represented. However, the base of the GHSZ, the interval where most melting and reformation occurs, represents a narrow interval in depth where the transport properties remain roughly constant over time. With regard to the second process, in fine-grained sediments, hydrates can form nodules and lenses that mechanically displace grains.[38] These processes can also have an impact on the effective transport properties of the system. Addressing these processes go beyond the scope of the simulator. Despite these considerations, the methods and results of this study are still meaningful and offer a building block in understanding the effects of hydrate formation on the transport properties of porous systems during sedimentation.

The simulations of the sedimentation rate showed the evolution of a hydrate accumulation over geological time. As expected, the temperature increase as a result of sedimentation caused hydrate melting. However, the rate of dissociation was asynchronous with the rate of sedimentation. The evolution of the hydrate−gas boundary follows a staircase pattern that does not follow the theoretical GHSZ that the *in situ* conditions of the pressure, temperature, and salinity would yield (Figure 6). Each step of this pattern represents a cycle where methane and hydrate reaccommodate following the local conditions.

Each cycle consisted of a period of fast growth of hydrates followed by slow melting. The length of the cycles was constrained by the rate at which the temperature increased (sedimentation) and the amount of hydrate that had formed at the beginning of each cycle. For the 220 mm/year sedimentation rate, at least two full cycles were observed (Figure 6). Melting started at the warmest and deepest intervals of the hydrate layer. Expelled methane reentered the gas column underneath, and the remaining hydrate became

https://doi.org/10.1021/acs.energyfuels.1c03611
Energy Fuels XXXX, XXX, XXX−XXX

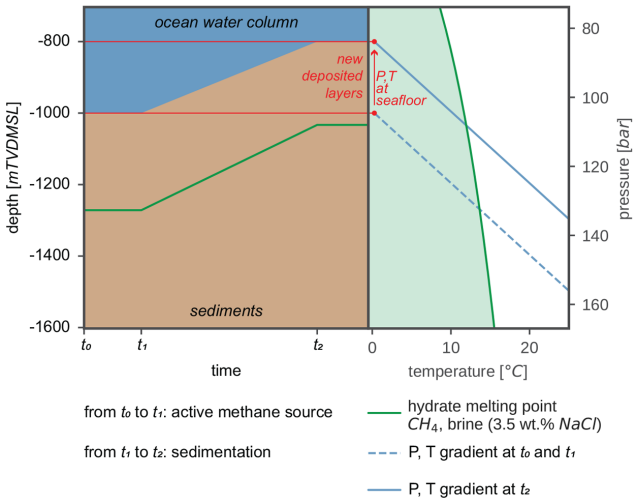

Figure 4. Schematic representation of how the sedimentation rate is modeled. On the left is a depth versus time chart showing how the sediment column changes over time. The methane gas source starts at t_0 and stops at t_1. At t_1, sedimentation starts and stops once it has deposited a thickness of 200 m. On the right is a P versus T chart displaying the boundary of stability (green) and the *in situ* P and T gradients at t_0, t_1, and t_2. The green-shaded region highlights the P and T ranges, where hydrates are stable. The depth at which the *in situ* gradients cross the stability boundary over time is displayed on the right and defines the base of the GHSZ.

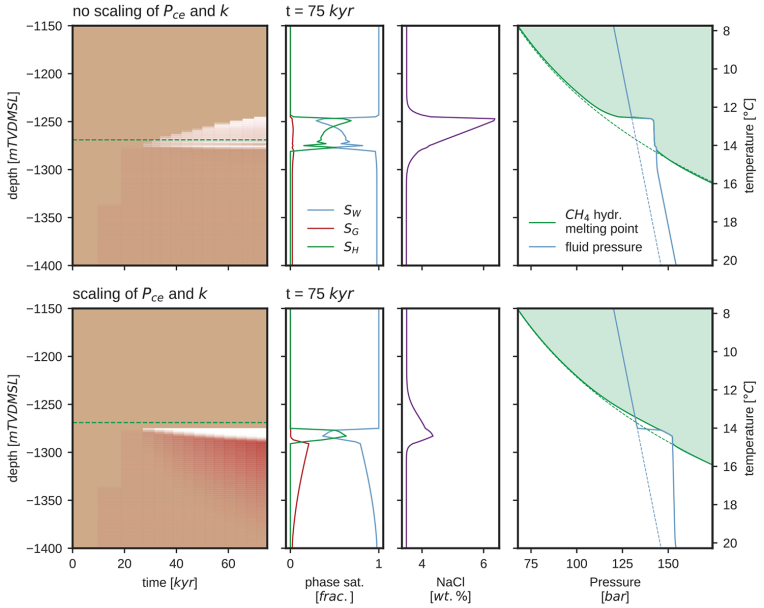

Figure 5. Cases 1A and 1B, with resulting hydrate accumulations from buoyancy-driven gas flow. The top row shows results for an accumulation where scaling of transport properties is not considered. The bottom row shows the results for an accumulation in the bottom where parameters from Table 2 were used to modify both k and P_c. From left to right, the first column shows the 1D evolution through time of hydrate (white) and gas (red) saturation. The green stippled horizontal line shows the base of the GHSZ at initial P and T conditions. The second and third columns show the distribution of phases and salinity concentrations at the end of hydrate formation (75 kyr). The last column shows the *in situ* (blue) P and T and the corresponding melting point (green) at both the beginning (stippled lines) and end (continuous lines) of the simulation. The green-shaded region highlights the P and T ranges, where hydrates are stable.

https://doi.org/10.1021/acs.energyfuels.1c03611
Energy Fuels XXXX, XXX, XXX−XXX

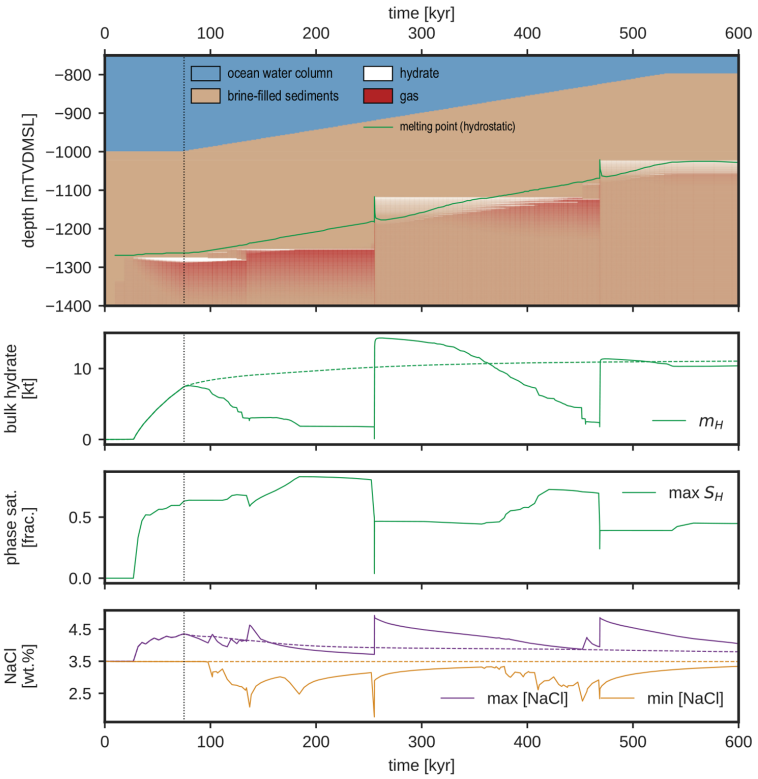

Figure 6. Case 3A, with evolution of hydrate occurrence during sedimentation (220 m/kyr). From top to bottom, the first chart shows the 1D evolution through time of hydrate (white) and gas (red) saturation. The green line shows the depth at which the temperature and pressure match the melting point at the given conditions. The second chart shows the bulk mass of hydrate through time during sedimentation (continuous) and with no sedimentation (stippled, case 2). The third chart shows the maximum hydrate saturation reached at each point in time. The fourth and last chart shows the maximum (purple) and minimum (orange) salinity during sedimentation (continuous) and with no sedimentation (stippled).

more concentrated. This is shown by how the maximum saturation of hydrates was reached toward the end of each cycle, because the bulk amount of hydrate (m_H) was at its minimum (Figure 6). After the gas column reached its maximum height, gas flowed through the hydrate layer and melted the remaining hydrate. It migrated upward, reached the shoaled base of the GHSZ, and formed new hydrates.

Figure 7 shows a detailed overview of one of these cycles. It tracks the interaction between the externally imposed temperature changes and the internal phase changes of hydrates and the resulting gas flow. The initial amount of hydrate was the result of an influx of gas migrating into the colder and shallower intervals (between points 1 and 2 in Figure 7). A peak in salinity was recorded at this instant. The melting of hydrates underneath dilutes the salinity locally, supporting the growth of more hydrates at this depth (between points 2 and 3 in Figure 7). The remaining hydrates were concentrated in a thin layer with high saturation. The peak in saturation allowed the layer to become an effective capillary seal able to support the underlying thick column of free gas. At this stage, melting was prolonged by the interplay between the variations of salinity and pressure (between points 3 and 4 in Figure 7). A very subtle increase in salinity suggests that hydrates were reformed as the capillary pressure kept increasing. Once the capillary entry pressure of the hydrate-bearing layer is overcome, the gas breaks through the seal and flows to a shallower interval, exceeding to form a new hydrate accumulation (between points 4 and 5 in Figure 7). The final melting was marked by a brief decrease in both the salinity and temperature.

When the permeability was decreased (1 μD), the simulation showed similar processes. However, the cycles were much shorter and more frequent during the same time span (Figure 8). The thickness of formed hydrate layers on each cycle was also thinner. Similarly, at a higher sedimentation rate (2 m/year), the simulation also showed a higher frequency of cycles (Figure 9) for the same thickness of sediments being deposited over time.

The process of sedimentation modeled here showed how the hydrates change as the system becomes progressively warmer. Although the hydrates are in net melting, the dynamic fluctuations of both S_H and NaCl(aq) concentration steer the rate at which fluid phases move through the system and phase changes occur, causing periods of melting and

https://doi.org/10.1021/acs.energyfuels.1c03611
Energy Fuels XXXX, XXX, XXX−XXX

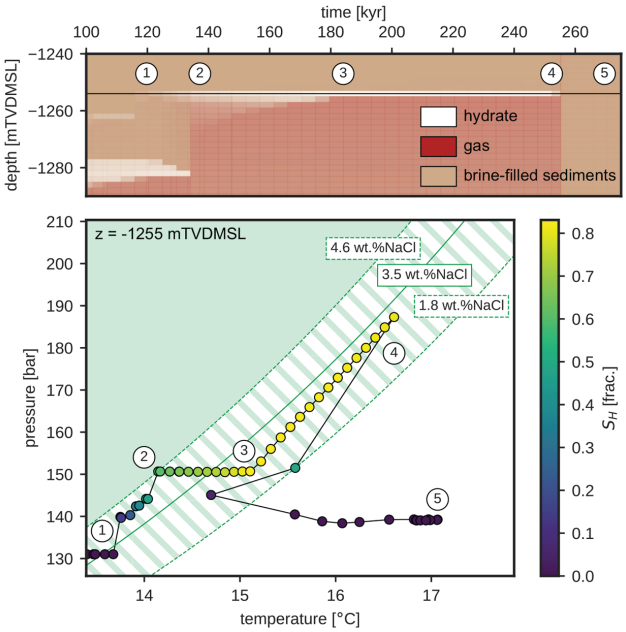

Figure 7. Case 3A, with the pressure and temperature evolution through time at 1255 mTVDMSL between 100 and 275 kyr. The top chart shows the 1D evolution through time of hydrate (white) and gas (red) saturation. The black horizontal line displays the depth at which pressure and temperature have been logged, and the circled numbers highlight the points where major changes occur in the pressure and temperature. The main chart at the bottom shows the logged pressure and temperature overlaid by the hydrate stability boundary at different salinity concentrations. The green-shaded region highlights the P and T ranges, where hydrates are stable. At point 1, hydrates start forming. Between points 2 and 3, hydrate saturation increases but salinity decreases as a result of the melting of underneath hydrates. At point 3, maximum hydrate saturation is reached, but all hydrates below this depth have melted in the system. Melting is actively occurring, but the incoming gas from underneath and the increased pressure preserve the hydrate accumulation. At point 4, the system quickly melts, salinity decreases, gas breaks through, and pressure decreases. At point 5, the system is filled by brine and residual gas.

reformation. Each cycle is initiated by gas flowing into the GHSZ and forming hydrates. The amount of methane capable of flowing is determined by the intrinsic transport properties of the sediments. In cases 3A and 4, the hydrate layers are thicker than in case 3B, where the intrinsic permeability is 100 times smaller.

The highest amount of hydrates (m_H) is reached at this point. This is reflected on the NaCl(aq) concentration reaching its peak. However, these hydrates are distributed over a thick layer, and S_H is not at its maximum. This means that the system is still permeable and can be drained by gas.

The temperature keeps increasing, and the hydrates at the deepest part of the layer are the first to melt. The higher melting point caused by the diluted brine and the availability of gas at a pressure high enough to invade the hydrate-bearing intervals result in further formation of hydrates. S_H reaches its maximum; permeability decreases; and the capillary entry pressure increases. At this point, the hydrate layer is an effective flow barrier. Both permeability and sedimentation rate can have an impact on the maximum S_H at this stage. With a lower permeability (case 3B; Figure 8), more methane remains as free gas trapped below hydrates. The larger gas column results in a higher capillary pressure, and the low permeability results in a slower rate at which more methane can turn into hydrate. The peak in S_H is also lower when the sedimentation rate is increased (case 4; Figure 9). When melting occurs at a faster rate, not enough time is given to develop a concentrated layer of hydrate with high S_H. The lower peak in S_H makes the capillary entry pressure of the hydrate-bearing layer lower and the length of the cycle shorter.

During the final stages of melting, the system goes through a period where each loss of hydrate can be compensated by gas invading the layer and forming new hydrates. No major increases are observed in S_H, but the slight increase in salinity decreases the melting point, making the hydrate progressively less stable. Because hydrates cannot support the underlying gas accumulation, the hydrate flow barrier fails and gas breaks through. When gas breakthrough occurs, the heat transported by the gas melts the remaining hydrate, reducing m_H to zero, just before a new hydrate layer is formed.

If the intrinsic permeability of the host sediments is not low (1 mD, cases 3A and 3B), gas may leak through the hydrate layer. As soon as it approaches the boundary of stability, it starts forming a new hydrate layer and, therefore, a new flow barrier. This mechanism was observed in both cases 3A and 3B, during periods where the thickness of the free gas zone was at its maximum.

Assuming that the effects of hydrate growth on sediment transport properties resemble those used in these models, the rate at which shoaling occurs is influenced by both intrinsic permeability and capillary entry pressure. Unlike the modeled sedimentation rate, shoaling occurs in pulses. The length of

https://doi.org/10.1021/acs.energyfuels.1c03611
Energy Fuels XXXX, XXX, XXX−XXX

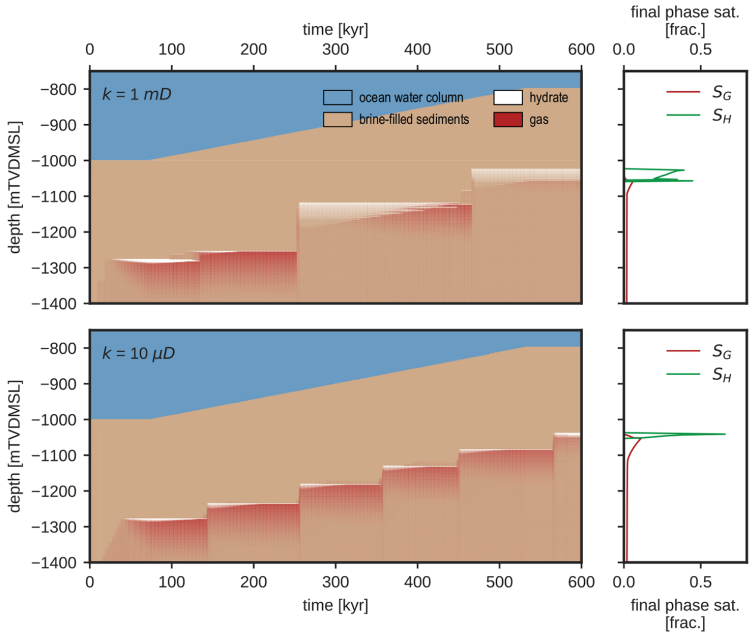

Figure 8. Comparison between cases 3A and 3B, with permeability sensitivity. On the left, hydrate evolution in the system with a permeability of 1 mD (top) and a system with a permeability of 10 μD (bottom). On the right column, final saturation of both gas (S_G) and hydrate (S_H).

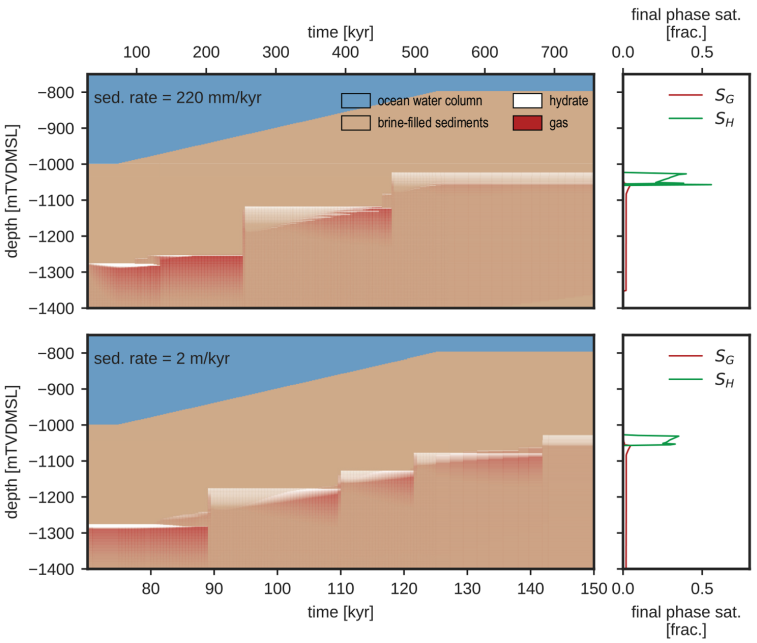

Figure 9. Comparison between cases 3A and 3C, with sedimentation rate sensitivity. On the left, hydrate evolution in a system with a sedimentation rate of 220 mm/year (top) and a sedimentation rate of 2 m/year (bottom). On the right column, final saturation of both gas (S_G) and hydrate (S_H).

https://doi.org/10.1021/acs.energyfuels.1c03611
Energy Fuels XXXX, XXX, XXX−XXX

each pulse is a function of the heating through burial (sedimentation rate), maximum S_H, and thickness of the free gas zone.

BSR responses are normally assumed to coincide with the boundary of stability and used to derive the geothermal gradient.[39] These methods normally assume linear gradients of both pressure and temperature. However, during sedimentation, within each pulse or cycle of melting, the local pore pressure underneath the hydrate layer is actively changing. This makes the pressure gradient no longer linear or hydrostatic, particularly toward the end of each cycle. In a basin that has been experiencing sedimentation over the previous thousands of years, the characteristics of the BSR response can be affected by where, within the melting cycle, the hydrate occurrence is taking place. The identification of multiple BSR responses can be associated with those transitional periods observed in cases 3A and 4, where gas has leaked through the hydrate layer and the hydrate occurrence is shoaling.

CONCLUSION

(1) During sedimentation, a hydrate occurrence experiences pulses of melting and reformation. The length and frequency of each pulse are influenced by the rate of sedimentation and the transport properties of the host sediments. (2) Although the mechanical properties of sediments are not considered in this study, it is possible to emulate the processes of sedimentation and burial within the context of natural gas hydrate occurrences. The results are a building block in understanding the effects of hydrate formation on the transport properties of porous systems during sedimentation. (3) By keeping track of the variations in the pressure, temperature, phase saturations, and concentration of soluble components, it is possible to understand the evolution of each cycle. (4) The characteristics of a BSR response in a system that has been under active sedimentation will vary depending upon the stage of melting that the system is currently experiencing. (5) In a system with a high intrinsic capillary entry pressure, toward the end of the cycle, hydrate-bearing sediments can become a capillary seal. This results in a boundary of stability placed deeper than what the hydrostatic gradient predicts. (6) Leakage of methane through permeable hydrate layers and reformation of hydrates at shallower depths over long periods can result in double BSRs.

AUTHOR INFORMATION

Corresponding Author

Alejandro Bello-Palacios − *Department of Physics and Technology, University of Bergen, 5020 Bergen, Norway; Equinor ASA, 5020 Bergen, Norway;* orcid.org/0000-0002-0294-9485; Phone: +47-941-56-014; Email: gpb@equinor.com

Authors

Per Fotland − *Equinor ASA, 5020 Bergen, Norway*

Geir Ersland − *Department of Physics and Technology, University of Bergen, 5020 Bergen, Norway*

Complete contact information is available at: https://pubs.acs.org/10.1021/acs.energyfuels.1c03611

Notes

The authors declare no competing financial interest.

ACKNOWLEDGMENTS

This work was supported by funding from the Norwegian Research Council. Equinor ASA is thanked for permission to publish this work.

NOMENCLATURE

Abbreviations

BR = Blake Ridge
BSR = bottom simulating reflector
GHSZ = gas hydrate stability zone
GOM = Gulf of Mexico
IODP = International Ocean Discovery Program
ODP = Ocean Drilling Program
T+H = TOUGH+HYDRATE

Symbols

λ = thermal conductivity
ϕ = effective porosity (hydrate-scaled)
ϕ_0 = intrinsic porosity
ϕ_c = critical hydrate-filled porosity at which permeability is reduced to zero
ρ = density
W, G, and H = subscripts representing aqueous, gas, and hydrate phases, respectively
c_p = specific heat
k = effective permeability (hydrate-scaled)
k_0 = intrinsic permeability
k_r = relative permeability
k_{rF} = permeability reduction factor
P_c = capillary pressure
P_c^* = hydrate-scaled capillary pressure
P_{ce} = capillary entry pressure
S = phase saturation
S_{irr} = irreducible phase saturation
X_{inh} = brine salinity
aq and g = aqueous and gaseous states of aggregation
CH_4 = methane
H_2O = water
NaCl = sodium chloride
kyr = thousands of years
m = total mass
mD and μD = permeability in millidarcy and microdarcy, respectively
mTVDMSL = meters below mean sea level
P = pressure
T = temperature

REFERENCES

(1) Sloan, E. D.; Koh, C. A. *Clathrate Hydrates of Natural Gases*, 3rd ed.; CRC Press: Boca Raton, FL, 2008; Vol. *119*, Chapter 1, pp 1−28.

(2) Boswell, R.; Collett, T. S. Current perspectives on gas hydrate resources. *Energy Environ. Sci.* **2011**, *4*, 1206−1215.

(3) Collett, T. S.; Johnson, A. H.; Knapp, C. C.; Boswell, R. *Natural Gas Hydrates−Energy Resource Potential and Associated Geologic Hazards*; American Association of Petroleum Geologists (AAPG): Tulsa, OK, 2009.

(4) Boswell, R.; Collett, T. The gas hydrates resource pyramid. *Fire in the Ice* **2006**, *06*, 5−7.

(5) Paull, C. K.; Matsumoto, R.; Wallace, P. J.; Dillon, W. P. *Proceedings of the Ocean Drilling Program, Scientific Results, 164*; College Station, TX, 2000; DOI: 10.2973/odp.proc.ir.164.1996.

(6) Tréhu, A. M.; Bohrmann, G.; Torres, M. E.; Colwell, F. S. Leg 204 Synthesis: Gas Hydrate Distribution and Dynamics in the Central Cascadia Accretionary Complex. *Proceedings of the Ocean Drilling*

https://doi.org/10.1021/acs.energyfuels.1c03611
Energy Fuels XXXX, XXX, XXX−XXX

Program, Scientific Results, 204; College Station, TX, 2006; DOI: 10.2973/odp.proc.sr.204.101.2006.
(7) Riedel, M.; Collett, T. S.; Malone, M. Expedition 311 synthesis: Scientific findings. *Proceedings of the IODP, 311*; Washington, D.C., 2010; DOI: 10.2204/iodp.proc.311.213.2010.
(8) Karstens, J.; Haflidason, H.; Becker, L. W. M.; Berndt, C.; Rüpke, L.; Planke, S.; Liebetrau, V.; Schmidt, M.; Mienert, J. Glacigenic sedimentation pulses triggered post-glacial gas hydrate dissociation. *Nat. Commun.* **2018**, *9*, 635.
(9) Collett, T.; Bahk, J.-J.; Baker, R.; Boswell, R.; Divins, D.; Frye, M.; Goldberg, D.; Husebø, J.; Koh, C.; Malone, M.; Morell, M.; Myers, G.; Shipp, C.; Torres, M. Methane Hydrates in Nature−Current Knowledge and Challenges. *J. Chem. Eng. Data* **2015**, *60*, 319−329.
(10) You, K.; Flemings, P. B.; Malinverno, A.; Collett, T. S.; Darnell, K. Mechanisms of Methane Hydrate Formation in Geological Systems. *Rev. Geophys.* **2019**, *57*, 1146−1196.
(11) Collet, T. S.; Ladd, J. Detection of gas hydrate with downhole logs and assessment of gas hydrate concentrations (saturations) and gas volumes on the Blake Ridge with electrical resistivity log data. *Proceedings of the Ocean Drilling Program, Scientific Results, 164*; College Station, TX, 2000; DOI: 10.2973/odp.proc.sr.164.219.2000.
(12) Wu, N.; Zhang, H.; Yang, S.; Zhang, G.; Liang, J.; Lu, J.; Su, X.; Schultheiss, P.; Holland, M.; Zhu, Y. Gas Hydrate System of Shenhu Area, Northern South China Sea: Geochemical Results. *J. Geol. Res.* **2011**, *2011*, 1−10.
(13) Paull, C. K.; Matsumoto, R. Leg 164 overview. *Proceedings of the Ocean Drilling Program, Scientific Results, 164*; College Station, TX, 2000; DOI: 10.2973/odp.proc.sr.164.204.2000.
(14) Paull, C. K.; Ussle, W.; Borowski, W. S. Sources of Biogenic Methane to Form Marine Gas Hydrates In Situ Production or Upward Migration? *Ann. N. Y. Acad. Sci.* **1994**, *715*, 392−409.
(15) Liu, X.; Flemings, P. B. Dynamic multiphase flow model of hydrate formation in marine sediments. *J. Geophys. Res.* **2007**, *112*, B03101.
(16) Paull, C. K.; Ussler, W. I.; Borowski, W. S. *Sources of Biogenic Methane to Form Marine Gas Hydrates: In Situ Production or Upward Migration?*; University of North Carolina at Chapel Hill: Chapel Hill, NC, 1993; Report DOE/ER/61010--T12.
(17) Hyndman, R. D.; Spence, G. D. A seismic study of methane hydrate marine bottom simulating reflectors. *J. Geophys. Res.: Solid Earth* **1992**, *97*, 6683−6698.
(18) Wilder, J. W.; Moridis, G. J.; Wilson, S. J.; Kurihara, M.; White, M. D.; Masuda, Y.; Anderson, B. J.; Collett, T. S.; Hunter, R. B.; Narita, H. An international effort to compare gas hydrate reservoir simulators. *Proceedings of 6th International Conference on Gas Hydrates (ICGH 2008)*; Vancouver, British Columbia, Canada, July 6−10, 2008.
(19) White, M. D.; Kneafsey, T. J.; Seol, Y.; Waite, W. F.; Uchida, S.; Lin, J. S.; Myshakin, E. M.; Gai, X.; Gupta, S.; Reagan, M. T.; Queiruga, A. F.; Kimoto, S.; Baker, R. C.; Boswell, R.; Ciferno, J.; Collett, T.; Choi, J.; Dai, S.; De La Fuente, M.; Fu, P.; Fujii, T.; Intihar, C. G.; Jang, J.; Ju, X.; Kang, J.; Kim, J. H.; Kim, J. T.; Kim, S. J.; Koh, C.; Konno, Y.; Kumagai, K.; Lee, J. Y.; Lee, W. S.; Lei, L.; Liu, F.; Luo, H.; Moridis, G. J.; Morris, J.; Nole, M.; Otsuki, S.; Sanchez, M.; Shang, S.; Shin, C.; Shin, H. S.; Soga, K.; Sun, X.; Suzuki, S.; Tenma, N.; Xu, T.; Yamamoto, K.; Yoneda, J.; Yonkofski, C. M.; Yoon, H. C.; You, K.; Yuan, Y.; Zerpa, L.; Zyrianova, M. An international code comparison study on coupled thermal, hydrologic and geomechanical processes of natural gas hydrate-bearing sediments. *Mar. Pet. Geol.* **2020**, *120*, 104566.
(20) Burwicz, E.; Rüpke, L. Thermal State of the Blake Ridge Gas Hydrate Stability Zone (GHSZ)−Insights on Gas Hydrate Dynamics from a New Multi-Phase Numerical Model. *Energies* **2019**, *12*, 3403.
(21) You, K.; Flemings, P. B. Methane Hydrate Formation and Evolution during Sedimentation. *J. Geophys. Res.: Solid Earth* **2021**, *126*, e2020JB021235.
(22) Nole, M.; Daigle, H.; Cook, A. E.; Malinverno, A.; Flemings, P. B. Burial-driven methane recycling in marine gas hydrate systems. *Earth Planet. Sci. Lett.* **2018**, *499*, 197−204.
(23) Moridis, G.; Pruess, K. *User's Manual of the TOUGH+ v1. 5 Core Code: A General Purpose Simulator of Non-Isothermal Flow and Transport through Porous and Fractured Media*; Lawrence Berkeley National Laboratory (LBNL): Berkeley, CA, 2014; Report LBNL-6871E.
(24) Moridis, G. *User's Manual for the HYDRATE v1. 5 Option of TOUGH+ v1. 5: A Code for the Simulation of System Behavior in Hydrate-Bearing Geologic Media*; Lawrence Berkeley National Laboratory (LBNL): Berkeley, CA, 2014; Report LBNL-6869E.
(25) Gamwo, I. K.; Liu, Y. Mathematical Modeling and Numerical Simulation of Methane Production in a Hydrate Reservoir. *Ind. Eng. Chem. Res.* **2010**, *49*, 5231−5245.
(26) Moridis, G. J.; Collett, T. S.; Dallimore, S. R.; Satoh, T.; Hancock, S.; Weatherill, B. Numerical studies of gas production from several CH_4 hydrate zones at the Mallik site, Mackenzie Delta, Canada. *J. Pet. Sci. Eng.* **2004**, *43*, 219−238.
(27) Li, B.; Li, X.-S.; Li, G.; Chen, Z.-Y. Evaluation of gas production from Qilian Mountain permafrost hydrate deposits in two-spot horizontal well system. *Cold Reg. Sci. Technol.* **2015**, *109*, 87−98.
(28) Sun, J.; Ning, F.; Zhang, L.; Liu, T.; Peng, L.; Liu, Z.; Li, C.; Jiang, G. Numerical simulation on gas production from hydrate reservoir at the 1st offshore test site in the eastern Nankai Trough. *J. Nat. Gas Sci. Eng.* **2016**, *30*, 64−76.
(29) Jin, G.; Lei, H.; Xu, T.; Xin, X.; Yuan, Y.; Xia, Y.; Juo, J. Simulated geomechanical responses to marine methane hydrate recovery using horizontal wells in the Shenhu area, South China Sea. *Mar. Pet. Geol.* **2018**, *92*, 424−436.
(30) Zhu, H.; Xu, T.; Zhu, Z.; Yuan, Y.; Tian, H. Numerical modeling of methane hydrate accumulation with mixed sources in marine sediments: Case study of Shenhu Area, South China Sea. *Mar. Geol.* **2020**, *423*, 106142.
(31) Marín-Moreno, H.; Minshull, T. A.; Westbrook, G. K.; Sinha, B. Estimates of future warming-induced methane emissions from hydrate offshore west Svalbard for a range of climate models. *Geochem., Geophys., Geosyst.* **2015**, *16*, 1307−1323.
(32) Kowalsky, M. B.; Moridis, G. J. Comparison of kinetic and equilibrium reaction models in simulating gas hydrate behavior in porous media. *Energy Convers. Manage.* **2007**, *48*, 1850−1863.
(33) Stone, H. Probability model for estimating three-phase relative permeability. *J. Pet. Technol.* **1970**, *22*, 214−218.
(34) van Genuchten, M. T. A Closed-form Equation for Predicting the Hydraulic Conductivity of Unsaturated Soils. *Soil Sci. Soc. Am. J.* **1980**, *44*, 892−898.
(35) Henry, P.; Thomas, M.; Clennell, M. B. Formation of natural gas hydrates in marine sediments: 2. Thermodynamic calculations of stability conditions in porous sediments. *J. Geophys. Res.: Solid Earth* **1999**, *104*, 23005−23022.
(36) Day-Stirrat, R. J.; Flemings, P. B.; You, Y.; Aplin, A. C.; van der Pluijm, B. A. The fabric of consolidation in Gulf of Mexico mudstones. *Mar. Geol.* **2012**, *295*−*298*, 77−85.
(37) Davie, M. K.; Buffett, B. A. A numerical model for the formation of gas hydrate below the seafloor. *J. Geophys. Res.: Solid Earth* **2001**, *106*, 497−514.
(38) Jang, J.; Santamarina, J. C. Hydrate bearing clayey sediments: Formation and gas production concepts. *Mar. Pet. Geol.* **2016**, *77*, 235−246.
(39) Zwart, G.; Moore, J. C.; Cochrane, G. R. Variations in temperature gradients identify active faults in the Oregon accretionary prism. *Earth Planet. Sci. Lett.* **1996**, *139*, 485−495.

https://doi.org/10.1021/acs.energyfuels.1c03611
Energy Fuels XXXX, XXX, XXX−XXX

Poster

A.4 Modelling Relative Permeability: Stretching the learnings from laboratory experiments

Alejandro Bello-Palacios, Stian Almenningen, Per Fotland, and Geir Ersland

2020 Gordon Research Conference and Seminar on Natural Gas Hydrate Systems. February, 2020. Galveston, TX United States.

Modelling Relative Permeability: Stretching the learnings from **laboratory experiments**

Alejandro Bello-Palacios[1], Stian Almenningen[2], Per Fotland[1], Geir Ersland[2]
[1]Equinor ASA, Bergen, Norway
[2]Department of Physics and Technology, University of Bergen, Norway

BACKGROUND

- In multiphase flow through hydrate-bearing rocks the effective phase permeability is affected by both:
  - porosity reduction driven by hydrate growth
  - each phase inhibiting the flow of the other.
- Core flooding experiments in methane hydrate-bearing Bentheim sandstone show that effective gas permeability decreased from mD-scale to µD-scale. Growth of pore-filling hydrate can make the gas phase disconnected and capillary immobile.
- Agreement between experimental data and numerical predictions is essential to better understand the complexity of the experiments and the limitations of the models.

DISCUSSION

- It is possible to reproduce laboratory experiments in T+H. However, further iterations should be performed honoring the uncertainty of the initial measurements and make a statistical analysis of the simulated results.
- Preliminary fitting of the permeability reduction factor relationship is affected by low measurements (µD scale). It yields a relationship where the sandstone is "clogged" when hydrate saturation is above ~50%.
- Simulation of hydrate formation reflected the experimental results in terms of final phase saturations. In addition, it was possible to keep track of changes in salinity concentration associated to hydrate formation.
- Simulations of core flooding experiments before hydrate formation were successful and replicated the results obtained in the laboratory.
- In hydrate bearing samples, simulations produced numerical instability reflecting the complexity of the system and how challenging is to carry out these experiments.
- In T+H the effective phase permeability in presence of hydrates is scaled by the permeability reduction factor.

$$k_{eff} = k_{abs} \cdot k_r \cdot PrF$$

By scaling the relative permeability relationships, it is assumed that the porous media keeps the same wettability, tortuosity and other effects that have an impact on the shape of the curve.

METHODS

Experiments are reproduced using the equilibrium model of TOUGH+HYDRATE (T+H) on a simple 2-dimensional grid representation of the core.

- Least squares regression on the experimental data to find the T+H input parameters to calculate relative permeability (krg) and permeability reduction factor (PrF).

$$\frac{k}{k_0} = PrF = \left(\frac{\phi - \phi_c}{\phi_0 - \phi_c}\right)^n \quad \textit{Xu et al (2004)}$$

$$k_{rg} = \left(\frac{S_g - S_{gir}}{1 - S_{wir}}\right)^n \quad \textit{Stone (1970)}$$

- Initialization of grid at 10 degC and modelling core flooding to estimate relative permeability before hydrate formation.
- Initialization of grid at 4 degC and modelling core flooding to estimate relative permeability after hydrate formation.

Hydrate growth simulation

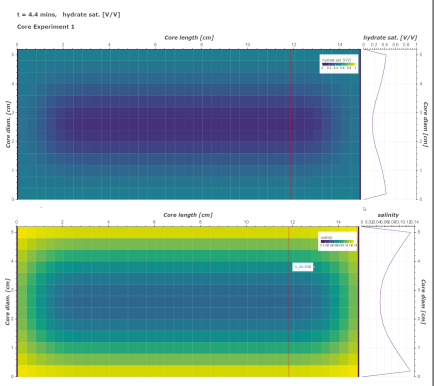

Experimental data

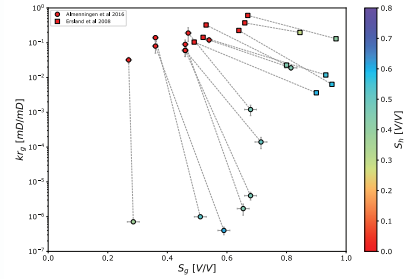

Hydrate growth over time

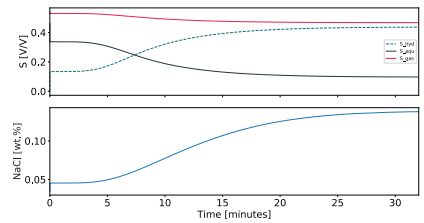

Preliminary fitting of models to data

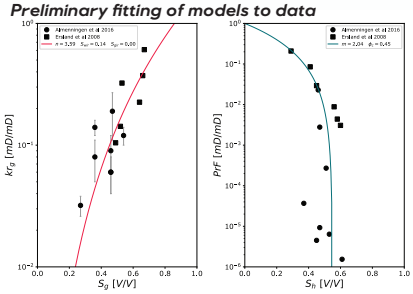

Model comparison to data

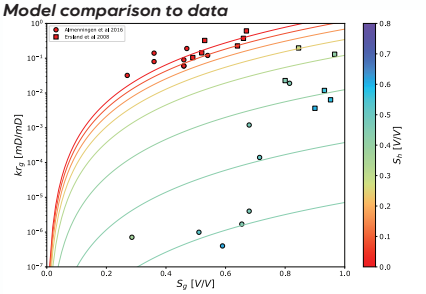

REFERENCES
Almenningen, Stian, Håkon Juliussen, and Geir Ersland. "Permeability measurements on hydrate-bearing sandstone cores with excess water." The 30th International Symposium of the Society of Core Analysts. 2016.
Ersland, Geir, et al. "Measurements of gas permeability and non-Darcy flow in gas-water-hydrate systems." 6th International Conference on Gas Hydrates, Vancouver, BC, Canada. 2008
Stone, H. L. "Probability model for estimating three-phase relative permeability." Journal of Petroleum Technology 22.02 (1970): 214-218.
Xu, Tianfu, et al. "Reactive transport modeling of injection well scaling and acidizing at Tiwi field, Philippines." Geothermics 33.4 (2004): 477-491.

UNIVERSITY OF BERGEN
Faculty of Mathematics and Natural Sciences
equinor

Appendix B

Pre- and post-processing scripts for TOUGH+HYDRATE

The scripts can be found in a GitHub repository: *TH-PrePost* [Bello-Palacios, 2021]. The scripts hold a simple structure of nested functions that can be used in or adapted to be used in any T+H simulation file. In addition to standard Python packages, the user is encouraged to have installed the `pandas` and `numpy` libraries. The installation of `Jupyter` is also encouraged.

Currently, they only support Cartesian grids. However, the code is open to being adapted for radial grids. Instead of extensive documentation, the repository includes a `Jupyter` notebook, a web-based interactive computational environment for running `Python` scripts. This notebook includes a tutorial to showcase the main functionalities of the routines.

Below, there is a simple recipe to read and process all input and output files.

```
import sys
sys.path.append('<path-to-TH_scripts-folder')

from TH_post import *
from TH_proc import *
from MeshMaker import *
from Aux_Functions import *

#Define simulation file location
file_in = r'<path-to-simulation-input-file>'

#Read input file
```

```
ip_data = read_TH_data(file_in)

#Read output files
op_data = get_output(file_in)

#Read Time_Series and Hydrate_Status files
subdoms, interfs, hyd_status, ss_groups = read_Time_Series(file_in)
```

The stored variables shall consist mainly of pandas dataframes that could be easily accessed for plotting or further calculations.

Graphic design: Communication Division, UiB / Print: Skipnes Kommunikasjon AS

uib.no

ISBN: 9788230842829 (print)
9788230841723 (PDF)